Diss. ETH. No. 14233

Inverse Finite Element Characterization of Soft Tissues with Aspiration Experiments

A thesis submitted to the
SWISS FEDERAL INSTITUTE OF TECHNOLOGY
for the degree of
Doctor of Technical Sciences

presented by

Martin Kauer

Dipl. Masch.-Ing. ETH
born on 26 May, 1970
citizen of Italy

Accepted on the recommendation of
Prof. Dr. J. Dual, examiner
Prof. Dr. M. B. Rubin, coexaminer

Zürich, 2001

Acknowledgements

This work was carried out during my employment as an assistant at the Institute of Mechanical Systems at the ETH Zurich. I am grateful to all those who have contributed to this thesis, in particular to:

Prof. Dr. J. Dual for his kind support and encouragement during this work and for having given me the chance to work on a multidisciplinary project.

Prof. Dr. M. B. Rubin from the Technion-Israel Institute of Technology in Haifa, Israel, for carefully reviewing this thesis.

Prof. Dr. M. B. Sayir, for fruitful comments and discussions on my first steps in non-linear continuum mechanics.

Roland Hutter for his interesting discussions, Alex Rhomberg for his powerful computer support and Vladimir Vuskovic who performed all the aspiration experiments presented in this thesis.

Andreas Lindemuth, Mark Sturgess and Sascha Gassmann for contributing to this work with their semester and diploma thesis.

All the members of the Institute of Mechanical Systems for the good times together.

Martin Kauer
Zürich, June 2001

Table of contents

Table of contents i
Abstract v
Zusammenfassung vii
List of symbols ix

Introduction 1
1.1 Minimal invasive surgery and virtual reality 1
1.2 Methods for the description of the mechanical behaviour of organic tissue 3
1.3 Mechanical testing of soft tissues 4
1.4 Overview on soft tissue aspiration in the biomechanical research 6
1.5 Scope and outline of the present work 8

Tissue aspiration 11
2.1 The tissue aspiration experiment 11

Continuum Mechanics for soft tissues 15
3.1 Mechanical properties of soft biological tissues 15

3.2 Stress-strain relationship of soft tissues 16
3.3 Viscoelasticity of soft tissues 17
3.4 The basics of non-linear continuum mechanics 18
3.5 Modelling viscoelastic behaviour 30

Finite element formulation 39

4.1 Modified strain energy function for u/p-formulation 39
4.2 Derivation of the finite element equations 41
4.3 Explicit integration of the finite element equations 43
4.4 Contact 48
4.5 Accelerating the simulation by artificially increasing the density of the simulated material 50
4.6 Friction 54
4.7 Explicit versus implicit formulation 57

Inverse Finite Element Algorithm 59

5.1 Restricted step methods and trust region approach 62
5.2 Estimation of material parameters 66
5.3 Sensitivity to geometrical model errors 79

Results 83

6.1 Validation of the inverse parameter estimation 83
6.2 Material parameter estimation for the Silgel sample 90
6.3 Measurements on soft biological tissues 98
6.4 Intra-operative in-vivo measurements 107

Conclusions and Outlook 123

7.1 Conclusions 123
7.2 Outlook 125

Appendix A **129**
Appendix B **131**
Appendix C **135**

References **137**

Curriculum vitae **143**

Seite Leer /
Blank leaf

Abstract

In this thesis a method for the determination of material model parameters for biological soft tissues is presented. The requirement of *in-vivo* applicability of the method led to the development of a tissue aspiration instrument. The aspiration instrument was developed by Vladimir Vuskovic at the Institute of Robotics, whereas this work is mainly concerned with the continuum mechanical modelling of the soft tissues, the robust determination of the corresponding material model parameters, and their validity under more general loading conditions.

In the first part of this thesis an explicit axisymmetric finite element formulation for the simulation of the aspiration experiment is derived and implemented. The nearly incompressible material behaviour of soft biological tissues results in very small time steps of the explicit integration and thus in computationally expensive simulations. The quasi-static character of the aspiration experiment is used advantageously to accelerate the simulations by artificially increasing the material density.

The finite element code was integrated into an optimization algorithm. The optimization algorithm allows to fit unknown material parameters entering the finite element simulation to experimental reference data.

Soft biological tissues are modelled as isotropic, viscoelastic, non-linear, and nearly incompressible. The continuum mechanical hyperelastic models employed are standard models in the field of biomechanics. Viscoelasticity is accounted for by a quasi-linear formulation. In view of the two-dimensional data available from the experiments, the huge computational effort, that would be connected with a three-dimensional simulation, and the large increase in the number of unknown material parameters the soft tissue models are restricted to isotropic behaviour.

The friction in the contact zone of the tissue with the aspiration tube proved to play an important role for the determination of the material parameters. Experiments with a simple "tribometer" for the assessment of the respective friction coefficient posed many difficulties. In numerical studies the influence of the friction coefficient on the parameter determination process was studied. As a result of these studies it is recommended to increase the friction in the aspiration experiment as much as possible to ensure sticking of the tissue to the surface of the aspiration tube.

Numerical studies of the convergence properties of the optimization

algorithm were performed in connection with the employed material laws. From experiments with a duration shorter than the largest material relaxation time non-unique parameter sets resulted in the inverse parameter estimation. An increase of robustness was obtained by requiring the duration of the reference experiments to be equal to or larger than the largest material model relaxation time. The material parameters estimated from experiments of short duration in most cases do not represent correct material parameters in the sense that the fully relaxed material answer is not estimated correctly. Experiments can nonetheless be predicted well with the estimated material parameters if the calculated stretches are within the range of stretches observed in the reference experiment and also the stretch rates are similar to the respective values in the reference experiment.

The aspiration method was validated experimentally with a synthetic material. The parameters obtained from the aspiration experiment were used to predict the force-elongation behaviour of the material in tensile tests. These predictions were compared to data from real tensile tests. Very good agreement between the predicted and the measured tensile test data was observed.

The aspiration technique was applied to *ex-vivo* pig kidney measurements and *in-vivo* and *ex-vivo* on human uteri. The effect of tissue conditioning was measured with the aspiration experiment on pig kidney and could also be reproduced with the obtained material parameters. A polynomial material law depending on the first invariant of the deformation tensor c was proposed to describe the kidney cortex. The *in-vivo* experiments on the human uteri were performed intra-operatively during *hysterectomies*. The human uterine tissue proved to be a strongly viscoelastic material. A pronounced decrease in the tissue stiffness between *in-vivo* and *ex-vivo* measurements was observed. The intersample variation of the stiffness seems to be slightly higher than the stiffness variation observed on the single uteri. The maximum differences in stiffness observed in all performed measurements on the uteri are approximately equal in the *in-vivo* and the *ex-vivo* measurements.

Zusammenfassung

In dieser Arbeit wird eine Methode zur Bestimmung von Materialparametern für weiche biologische Gewebe vorgestellt. Die geforderte Einsetzbarkeit der Methode unter *in-vivo* Bedingungen führte zur Entwicklung eines Gewebeaspirationsgerätes. Das Gewebeaspirationsgerät wurde von Vladimir Vuskovic am Institut für Robotik der ETH Zürich entwickelt. Die hier vorgestellte Arbeit beschäftigt sich vor allem mit der mechanischen Modellierung weicher Gewebe und der robusten Bestimmung der in diesen Modellen enthaltenen Parameter.

Im ersten Teil dieser Arbeit wird eine explizite finite Element Formulierung für die Simulation des Aspirationsversuches hergeleitet und implementiert. Die als nahezu inkompressibel modellierten Gewebe bedingen sehr kleine Zeitschritte und damit rechenintensive Simulationen bei der expliziten Zeitintegration der finite Element Gleichungen. Der quasistatische Charakter des Aspirationsexperimentes kann jedoch vorteilhaft für eine Beschleunigung der Simulation des Experimentes genützt werden.

Das finite Elemente Programm wurde in einen Optimierungsalgorithmus integriert. Auf diese Art und Weise können die Parameter im Materialmodell der Simulation optimal an die experimentell gewonnenen Daten angepasst werden.

Weiche biologische Gewebe werden in dieser Arbeit als isotrop, viskoelastisch, nichtlinear und nahezu inkompressibel behandelt. Die verwendeten hyperelastischen Stoffgesetze können als Standardmodelle im Gebiet der Biomechanik bezeichnet werden. Die viskoelastischen Eigenschaften der Gewebe werden mittels eines quasilinearen Ansatzes berücksichtigt. Auf eine Modellierung der anisotropen Gewebeeigenschaften wurde aufgrund der dabei stark anwachsenden Zahl unbekannter Modellparameter, der nur in zwei Raumdimensionen vorhandenen experimentellen Daten aus dem Aspirationsversuch und der grossen benötigten Rechenleistung bei einer dreidimensionalen Modellierung verzichtet.

Es zeigte sich, dass die Reibung in der Kontaktzone von Aspirationsrohr und Gewebe eine grosse Rolle bei der Bestimmung der Materialparameter spielt. Experimente zur Bestimmung der Reibung mit einem selbstgebauten einfachen "Tribometer" erwiesen sich als sehr schwierig. In numerischen Simulationen wurde der Einfluss des Reibungskoeffizienten auf die inverse Materialparameterbestimmung untersucht. Als ein Resultat dieser

Untersuchungen wird empfohlen, den Reibungskoeffizienten in den Aspirationsexperimenten so gross wie möglich zu halten, um ein Haften des Gewebes am Aspirationsrohr sicherzustellen.

Konvergenzstudien des Optimierungsalgorithmus wurden in Zusammenhang mit verschiedenen Stoffgesetzen durchgeführt. Bei der inversen Auswertung von Experimenten mit einer Dauer, welche kleiner ist als die grösste im verwendeten Materialmodell vorkommende Relaxationszeit, resultieren keine eindeutigen Schätzungen für die Materialparameter. Eindeutige Parametersätze können durch Verlängern der Dauer des Aspirationsexperimentes gewonnen werden. Parameter, die aus Experimenten mit kurzer Dauer gewonnen werden, entsprechen in den meisten Fällen nicht den korrekten Materialparametern. Die voll relaxierte Materialantwort wird meist nicht korrekt widergegeben. Die gewonnenen Materialwerte können jedoch für korrekte Vorhersagen des Materialverhaltens verwendet werden, falls die Dehnungsgeschwindigkeiten und die Grösse der Dehnungen in den Vorhersagen mit jenen im ursprünglichen Referenzexperiment vergleichbar sind.

Die Aspirationsmethode wurde mittels Experimenten an einem weichen synthetischen Material validiert. Die aus den Aspirationsversuchen gewonnenen Parameter dienten zur Simulation von Zugversuchen. Bei der experimentellen Überprüfung dieser Vorhersagen konnte eine sehr gute Übereinstimmung zwischen Simulation und Experiment festgestellt werden.

Die Aspirationsmethode wurde *ex-vivo* an Schweinsnieren und *in-vivo* sowie auch *ex-vivo* an menschlichen Uteri angewendet. Der Effekt der Gewebekonditionierung wurde an Schweinsnieren gemessen und konnte mit dem vorgeschlagenen Gewebemodell in der ersten Invarianten des Deformationstensors C nachgebildet werden. Die *in-vivo* Messungen an den menschlichen Uteri wurden intraoperativ während offenen *Hysterectomien* durchgeführt. Eine deutliche Abnahme der Gewebesteifigkeit der Uteri zwischen *in-vivo* und *ex-vivo* Bedingungen wurde festgestellt. Die Steifigkeitsunterschiede des Uterusgewebes scheinen zwischen verschiedenen Uteri grösser zu sein als die lokalen Unterschiede an ein und demselben Uterus. Die Streuung aller gemessenen Uterussteifigkeiten ist bei den *in-vivo* und *ex-vivo* Messungen ungefähr gleich gross.

List of symbols

$\boldsymbol{A}$	Jacobian matrix
$\boldsymbol{C}$	right Cauchy-Green deformation tensor
$\boldsymbol{C}$	numerical damping matrix
$\boldsymbol{C}^*$	isochoric right Cauchy-Green deformation tensor
c_p	propagation speed of p-waves
c_i, c^u, c^p	weighting factors of reduced exponential relaxation function
C_{ijkl}	components of elasticity tensor
$\boldsymbol{D}$	symmetric part of velocity gradient
$\boldsymbol{E}$	Green-Lagrange deformation tensor
E^*, E', E''	complex, storage and loss modulus respectively
E^e	Young's modulus
E_∞, E_0	constants of Kelvin-Voigt model
$\boldsymbol{f}$	force vector
$\boldsymbol{F}$	deformation gradient
F_R	friction force
$G(t), \boldsymbol{G}(t)$	reduced relaxation function and reduced relaxation matrix function
h	parameter for trust region approach
h_I	I-th shape function
i	$\sqrt{-1}$
I_1, I_2, I_3	first, second and third invariant of $\boldsymbol{C}$
J_1, J_2, J_3	first, second and third reduced invariant of $\boldsymbol{C}$

K	deformed configuration of a continuum
$\boldsymbol{K}$	element stiffness matrix
K^0	reference configuration of a continuum
${}^{uu}\boldsymbol{K}, {}^{up}\boldsymbol{K}, {}^{pp}\boldsymbol{K}$	element stiffness matrices
L	element length
$\boldsymbol{L}$	velocity gradient
$\boldsymbol{M}$	mass matrix
N	normal contact force
$\boldsymbol{N}$	nominal stress tensor
N_d	span of frequency spectrum (in decades)
$o(\ )$	objective function
$\tilde{o}(\ )$	trust region approach of $o(\ )$
$p, \bar{p}, \tilde{p}$	hydrostatic pressure
$\boldsymbol{p}$	parameter vector
$\boldsymbol{r}$	residual vector
$\boldsymbol{R}$	orthogonal matrix
$\boldsymbol{S}, \boldsymbol{S}^e, \boldsymbol{S}'$	second Piola-Kirchhoff stress tensor
$\boldsymbol{S}_i^v$	history matrix function corresponding to relaxation time τ_i
$\boldsymbol{u}$	displacement vector
$\boldsymbol{U}$	right stretch tensor (symmetric)
u_{tol}	tolerance in friction model
$\boldsymbol{v}$	velocity (eulerian)
$\boldsymbol{V}$	left stretch tensor (symmetric)
$\boldsymbol{W}$	skewsymmetric part of velocity gradient
$\tilde{W}, \hat{W}, W_H, \overline{W}$	strain energy functions
$\boldsymbol{X}$	position vector in reference configuration
$\boldsymbol{x}$	position vector in deformed configuration
x, y, z	coordinates
α	material parameter in the Mooney-Rivlin and Veronda-Westmann formulation
γ	material parameter in the Veronda-Westmann formulation

δ_{ij}	Kronecker symbol
Δt	time step
ϵ	linear strain tensor
κ	bulk modulus
λ	stretch
$\bar{\lambda}$	Lamé constant
μ	material parameter in the Mooney-Rivlin, neo-Hookean and Veronda-Westmann formulation
$\bar{\mu}$	Lamé constant
μ_R, μ_0, μ_1	friction coefficients
ν	Poisson's ratio
ξ	numerical damping parameter
$\rho, \rho_{elem}, \rho_{real}$	material density
σ	Cauchy stress tensor
σ_{dev}	deviatoric part of Cauchy stress tensor
$\tau, \tau_i, \tau_i^u, \tau_i^p$	relaxation times
ω	angular frequency

$,i$	derivative with respect to i

Chapter 1

Introduction

1.1 Minimal invasive surgery and virtual reality

In the past few years a large increase of *minimal invasive* operation techniques has been observed in surgery. Minimal invasive surgery, also well known as *laparoscopy* or *keyhole surgery*, puts the surgeon in a completely new and unusual situation. In order to reduce the damage caused to the tissue by opening access holes leading to the internal organs only small perforation holes are cut and special surgical instruments are introduced through trocars. All manipulations are performed via instruments from outside of the abdomen. This situation requires very special training from the surgeon, since he loses direct contact to the operation site. No direct haptic contact nor any direct visual inspection of the organs or tissues is possible. The reaction forces of the deformed tissue are mediated through the surgical instruments to the surgeon and visual information is obtained by observing the abdomen with an endoscope. The images from the endoscope are, in most of the cases still in two-dimensional representation, displayed on a video monitor. Operating under these restricted conditions requires intensive training of the surgeon. Although in some special cases tests of new surgical devices or surgical techniques are performed on dead animals, ethical reasons and the limited availability of animal cadavers don't allow for extensive training and research. Here, virtual reality is probably one of the most promising fields to accommodate this need of training possibilities: flight simulators have already shown to provide very valuable training for pilots and surgery simulators will prove to be equally

well suited for surgical training. The capabilities of a surgical simulator seem to be limited only by the available computational power and the rendition requirements of details on the anatomical model. Compared to artificial organ models or training on dead animal organs the unlimited repeatability of training units is certainly a great advantage offered by surgery simulators. Also, special models for patient specific surgery planning and training are a long term target of virtual surgery simulations.

The situation of a surgical operation under laparoscopic conditions is very well suited to be simulated in a virtual environment. Already in the real laparoscopy the visual data is displayed on monitors and the surgical instruments are fixed through trocars. This situation can very easily be reproduced with a simulator.

At the ETH Zurich and the University Hospital Zurich the Mechatronics group has decided to pursue the goal of building such a virtual reality surgery training simulator. The schematic diagram in Fig. 1.1 shows the most important parts of this simulator. A project of this complexity needs

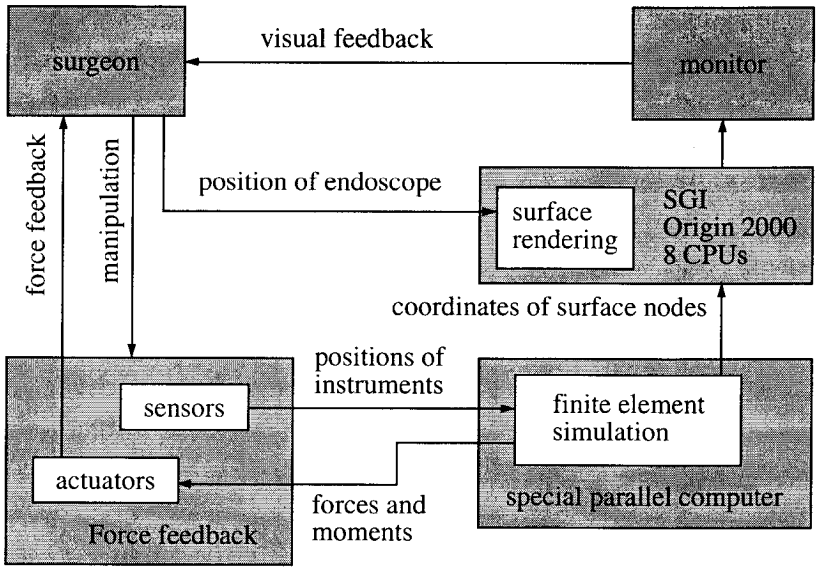

Fig. 1.1 Virtual reality laparoscopy simulator

research to be done in various fields and was thus divided into 5 subjects:

- Generation of a detailed geometrical model of the female abdomen for use in the simulation environment (because of the participation of the Department of Gynaecology of the University Hospital Zurich in the project we focus on the female abdomen).

- Modelling of the mechanical properties of soft tissues and estimation of the unknown model parameters.
- Development of methods for the *on-line* calculation of tissue deformation during purely diagnostic interventions (it is not yet a target of the present project to model cutting and sewing of tissues).
- Development of a parallel computer for the *real-time* computation of the finite element model.
- Development of algorithms for photorealistic rendering of organ surfaces.

From the above list we see that the description of the mechanics of soft tissues has been divided into two different parts: one part is concerned with the development of computationally fast finite element algorithms whereas the second part concentrates on the development of well suited material descriptions and especially on the *in-vivo* estimation of the unknown material parameters.

Surgical interventions like cutting or sewing are not targets of the present project since they require on-line re-meshing of the finite element model. On-line re-meshing has not been implemented in the current code and is not feasible with the mostly semi-automatic algorithms available at present.

1.2 Methods for the description of the mechanical behaviour of organic tissue

There are mainly two different approaches to soft tissue modelling: the first approach tries to realistically model the physical behaviour of soft tissues, whereas the second category of tissue models (like purely graphical methods or mass-spring systems) does not account for the complicated tissue mechanics, but in most cases has the great advantage of being simple and real-time computable.

In contrast to the widely used mass-spring systems or systems basing on purely graphical methods (surface interpolation) the finite element method is the consistent approach accounting for the continuous nature of soft tissues. Within the limits of the employed constitutive model the finite element method allows physically correct simulations of the tissue mechanics. Since soft tissues often undergo large deformations and in many cases show a strongly non-linear material behaviour non-linear finite element methods are indispensable for a correct simulation of their

behaviour. The finite element method was chosen as tool for the simulation of the tissue mechanics in the present virtual reality project.

In contrast to the finite element method, free form deformation models from computer graphics (Basdogan, 1998) or mass-spring models (Kühnapfel, 1995) can be assigned to the second category of models mentioned above. Although mass-spring models achieve a certain degree of physical realism the parameters of these models have to be set in a purely heuristic way and cannot be based on a general framework as in a continuum-mechanical approach. The parameters for mass-spring models cannot be gained from classical mechanical testing setups since there does not exist a physically consistent method to transform any experimentally gained data into parameters for the mass-spring model.

1.3 Mechanical testing of soft tissues

In the past, a big effort was made to characterize the mechanical properties of soft biological tissues. The two probably most important names to mention here are Yamada and Fung. Both researchers contributed much to the understanding and modelling of the mechanics of soft biological tissues. Yamada collected a variety of experimental data obtained by other researchers and also performed a large number of experiments on all kinds of human and animal tissues. This results are summarized in the book *Strength of Biological Materials* (Yamada, 1970). The work of Fung comprises a large number of books and other publications, but probably best known amongst people working in the field of biomechanics is his book *Biomechanics: Mechanical Properties of Living Tissues* (Fung, 1993 and also earlier editions). Fung did not only perform a large number of experiments but also contributed much to the mechanical modelling of soft biological tissues.

Classical research on the mechanical properties of soft biological tissues in most cases faces the problem that the amount of change in the elastic properties during preparation or excision of the studied tissue cannot be quantified. Almost all classical testing setups require excision of geometrically well defined samples. Indentation experiments might be seen as an exception to this problem. However, in *in-vivo* applications indentation experiments lack the ability to set well defined boundary conditions for the performed measurement. Only one-dimensional force-displacement histories are gained from indentation tests. If no additional tracking methods to measure the surface deformation around the indenter are used this one-

dimensional measurements may be susceptible to measurement errors. The rigid body motions of the whole organ caused by the contact force of the indenter are not accounted for. Only complicated tracking algorithms are able to avoid this error in the measured force vs. indentation-depth data.

Many different methods are used in biomechanics to quantitatively determine the mechanical properties of biomaterials. In the following we shortly present some standard setups used in biomechanical tissue testing. Apart from tissue indentation none of the presented classical testing methods is usable under *in-vivo* conditions. Widely used in soft tissue testing are experiments like compression or tension tests (Farshad, 1999). These tests require the excision of tissue samples and consequently result to be very sensitive to the geometry of the samples. Cutting samples from soft tissues and obtaining an accurate geometry is a challenging task. After excision, the samples are often stored in saline solutions. The effects of conservation procedures on the mechanical properties of the samples are not well known or have not yet been quantified. Inflation tests and also indentation experiments (Davies, 1998) are often used with thin tissue membranes; biaxial testing is quite common in experiments with skin or other thin layered tissues (Fung, 1993). All these experimental techniques require a lot of experience to overcome the difficulties of tissue handling and sample preparation.

At the moment major research efforts are made to use *non-invasive* methods, as e.g. ultrasound, for the evaluation of soft tissue parameters. Elastography basing on MRI or ultrasound displacement measurements are state of the art methods (Muthupillai, 1995). These acoustic methods allow the non-invasive characterization of tissues which are not accessible with classical testing methods. Due to the very small deformations caused by the acoustic waves propagating through the target tissue only elastic tangent moduli can be determined. Additionally, without prestraining of the target tissues only the tangential elastic modulus in the undeformed configuration can be measured with this approach. The Young's modulus might suffice to characterize the linear elastic behaviour for small tissue deformations. But, since most soft tissues show a strongly non-linear behaviour, the Young's modulus determines only the initial slope of the stress-strain curve and does not capture the material behaviour at large strains. Additionally, the frequency range (between 100 [Hz] and 1000 [Hz]) of the acoustic strain waves used in elastography experiments is not relevant for the material properties in virtual reality surgery simulation, where we want to simulate processes lasting approximately between 0.1 [s] and 100 [s].

Since virtual surgery simulations require the mechanical properties of tissues at large deformations our measurements cannot be limited to the linear elastic range.

1.4 Overview on soft tissue aspiration in the biomechanical research

Since this project is concerned with the characterization of soft tissues using soft tissue aspiration an overview of the research in this field is given in the following.

In contrast to the above discussed classical experimental setups, tissue aspiration is a technique which sets well defined boundary conditions through the contact of the aspiration tube with the soft tissue, yields two-dimensional load-deformation data and also allows an *in-vivo* application of the method.

Up to now tissue aspiration has mainly been used for the estimation of the mechanical properties of single cells in micro pipette aspiration experiments. A good overview of much of the work done on blood cells is given by Hochmuth (Hochmuth, 1993). Though the experimental setups used in micro pipette experiments are very similar to our tissue aspiration setup, the theoretical models used to analyse the results and determine the material parameters are different from those used in this work. Because of their special structure, cells are modelled as fluid filled membranes or shells, whereas tissue aspiration as it is performed in this study may rather be regarded as the application of surface forces to an infinite half space. Theret (Theret, 1988) and Sato (Sato, 1990) studied micro pipette cell aspiration with a half-space model. In the latter work the correspondence principle was applied to the model presented by Theret to account for the viscoelastic properties of the aspirated tissue. Both Theret and Sato used linear elastic models in their studies. Both models are based on the assumption of small deformations and require aspiration pipette radii to be small as compared to the radii of the aspirated cells. In view of the large tissue deformations observed in our aspiration experiments a linear elastic model would certainly be inadequate.

Spector (Spector, 1996) presented the pipette aspiration technique for the determination of the mechanical properties of cochlear outer hair cells. The theoretical model used is a linear shell model which neglects both adhesion of the aspirated cell to the pipette and contact friction.

Apart from the determination of cellular material properties, tissue aspi-

ration was presented by Aoki (Aoki, 1997), Okamoto (Okamoto, 1995), Guccione (Guccione, 1994) and Ohashi (Ohashi, 1995) for the determination of the mechanical properties of soft tissues. Aoki (Aoki, 1997) used a linear finite element model to evaluate aspiration experiments. For the linear range of deformations studied only a negligible difference between a model with no contact friction and a model with total adherence of the tissue to the aspiration pipette was observed. Viscoelasticity was not included in the model and experimental data was not obtained from soft tissues but from artificial materials only. Okamoto (Okamoto, 1995; see also Okamoto, 2000) used a square suction cup to perform suction experiments on ventricular myocardium. The deformation of the myocardium was measured using MR tagging. A qualitative comparison of experimental data and finite element simulations was done, but no material parameter estimation was performed by correlating experiment and simulation results. Guccione (Guccione, 1994) used a non-linear three-dimensional finite element model to analyse the transmural distribution of strain in the canine left ventricle that would be produced by local epicardial suction. A transversely isotropic exponential hyperelastic material law with varying transmural fibre axis was used to model passive myocardium. A complex mode of deformation was observed which suggested that material properties could be quantified under loading conditions similar to that which occur during left ventricular ejection. Material parameters were not determined in this study. In a following study (Okamoto, 2000) epicardial suction was applied to determine the passive material parameters for the left ventricle of the canine hart. Two finite element models were used in the evaluation: a homogeneous wall model and a model with separate epicardium. The employed material model was of an exponential type with transverse isotropy incorporated. Fibre directions for the heart model were taken from a separate study. The material parameters obtained from the parameter estimation by minimizing the measured and simulated displacements of a number of marked points in the ventricular wall were later used to predict ventricular wall deformations for suction pressures different from the ones used in the material parameter estimation. The calibration data for these predictions was taken from a separate study and the validity of this comparison is therefore questionable. The predicted displacements matched the reference data better when the epicardium was included as a separate layer in the model and a non-homogeneous ventricular wall was assumed. Ohashi (Ohashi, 1995) used pipette aspiration to measure the elastic moduli of bovine and porcine aortic walls. Linear elastic moduli for

the circumferential, the radial and the axial direction were determined from experiments by comparing the slope of the empirical pressure-deformation curve with simulated data from finite element models. No details about the model used to describe the contact between the tissue and the pipette are given.

1.5 Scope and outline of the present work

The scope of this thesis is the determination of adequate soft tissue models and of their parameters in order to allow realistic force-feedback in virtual reality surgery simulation. This main target may be split up in the following parts or questions:

- Development of an experimental technique allowing the *in-vivo* determination of the mechanical properties of living soft biological human tissues (in collaboration with the Institute of Robotics from the ETH Zurich).
- Implementation of an inverse finite element algorithm for the evaluation of the experimental data.
- Determination of adequate material laws for the description of the mechanical behaviour of soft biological tissues. In this thesis the material law is restricted to isotropic material behaviour. The viscoelastic material properties have to be modelled for a frequency range relevant for virtual reality surgery simulation (from approximately 10^{-2}[Hz] to 10[Hz]).
- Determination of the fully non-linear material response for a stretch range tolerable in *in-vivo* experiments and not only of the Young's modulus.
- How have the experiments to be carried out in order to allow a robust estimation of the material parameters of the chosen material laws and what influence have the mechanical boundary conditions (like e.g. friction) on the experiment?
- Validation of the inverse finite element method. Testing of the capability to predict the material behaviour for states of deformation different from the one used in the initial experiment with the material parameters obtained with the inverse finite element method .
- Determination of the *in-vivo* and *ex-vivo* mechanical properties of the human uterus.

In Chapter 2 the tissue aspiration instrument used for both the *in-vivo* and

the *ex-vivo* experiments on the soft biological tissues is presented. Although tissue aspiration has already been presented in the literature as a method for the estimation of material properties (Aoki, 1997) it has to our knowledge not yet been applied *in-vivo* on inner human organ tissues.

In Chapter 3 an introduction to the mechanical properties of soft tissues is given and the soft tissue models used in this work are presented. A non-linear isotropic hyperelastic model for soft tissue, including nearly incompressible behaviour and quasi-linear viscoelasticity, is employed. Though most biological materials are anisotropic, anisotropy was not included in our models. At present, it does not seem feasible to determine all the material parameters necessary to describe anisotropy under *in-vivo* conditions, especially without any *a priori* knowledge of the principle material directions. Including anisotropy in our models would require tracking of the whole aspirated tissue surface in our tissue aspiration experiments and not only of its profile. Additionally, all finite element computations would have to be carried out fully three-dimensional. A fully three-dimensional simulation of the problem would dramatically increase the computational effort in the inverse parameter estimation problem which is already considerable with the employed axisymmetric formulation. Soft biological tissue is assumed to be isotropic and homogeneous, at least in the small portion of tissue affected by the aspiration experiment. An initial stress-free tissue configuration is assumed. Though soft biological tissues are probably never in a stress-free state, the stresses induced by the aspiration experiment are assumed to be much larger than any stresses present in the unloaded tissue. In contrast to the publications presented in the overview in section 1.4 both the non-linear and the viscoelastic material properties of soft biological tissues are determined.

The deformation of the aspirated tissue is simulated with an explicit finite element code. Due to the nearly incompressible material behaviour of soft tissues very small time steps result with the chosen explicit integration of the finite element equations. An implicit integration scheme would be clearly preferable. However, the very large deformations observed in the tissue aspiration experiment require the computationally more expensive but also more robust explicit integration algorithm. A suitable element formulation is derived in Chapter 4 and also implemented. Contact between the pipette and the tissue is modelled as an undeformable-deformable contact. Friction is included in the model, although experimental determination of the parameters for the friction has shown to pose large difficulties. For dry tissue surfaces the tissue is assumed to stick to the

aspiration tube. This assumption was confirmed in experiments for dry pig kidney and dry pig liver tissue.

In Chapter 5 the parameter estimation algorithm used to fit the experimental data is presented. Together with the finite element algorithm this optimization routine makes up what is called an *inverse finite element algorithm*. In the parameter estimation routine, simulated profile data for an assumed material law simulated with the pressure data taken from the experiment is compared to the measured tissue deformation data. Squared differences between the two data sets are used to measure the quality of the match between the two data sets and find an optimal set of material parameters. A *Levenberg-Marquardt* algorithm was used to perform the material parameter optimization. The determinability of the different parameters in the employed material laws is studied at the end of Chapter 5. Guidelines for the aspiration experiments, resulting in a robust parameter estimation, are derived from these results.

At the beginning of Chapter 6 the tissue aspiration method is validated in the sense that the material parameters gained from the inverse finite element evaluation of an aspiration experiment are used to predict tension tests. These predictions are compared to experimental data from tension tests performed on the same material. A very soft gel-like synthetic material is used for these experiments.

The aspiration method is also applied to *ex-vivo pig* kidney aspiration experiments. The effect of tissue conditioning is measured. The parameters gained from the aspiration experiments proved to reflect the effect of tissue conditioning.

At the end of Chapter 6 *in-vivo* experiments performed on human uteri are presented. Since the aspiration experiments were performed on uteri which were extracted a comparison of the obtained *in-vivo* data with *ex-vivo* data was possible. To our knowledge, this comparison of *in-vivo* with *ex-vivo* material properties is for the first time possible for human soft tissues.

Chapter 2

Tissue aspiration

2.1 The tissue aspiration experiment

The experimental data needed to determine the parameters in the constitutive equations is obtained with tissue aspiration experiments. The soft tissue model parameters are then determined with an inverse finite element fitting routine. The *in-vivo* applicability of the aspiration experiment

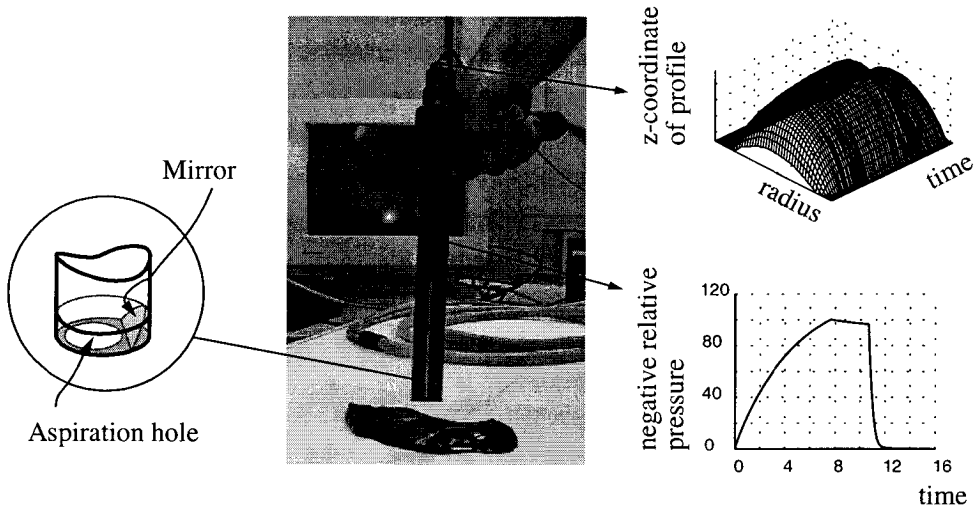

Fig. 2.1 Tissue aspiration instrument

requires the tissue aspiration instrument to be suited for sterilization. Easy handling of the instrument is another prerequisite for the use during surgi-

cal interventions in operating theatres. Many security aspects, like e.g. tissue damaging, had to be considered in the setup of the aspiration instrument. Therefore, the first *in-vivo* experiments on human tissue were performed on uteri which were then extracted. Nearly all of these uteri showed pathological indications. After the extraction of the uteri the aspiration experiments were repeated. This way both *in-vivo* and *ex-vivo* data is available for the human uteri.

The aspiration instrument used is shown in Fig. 2.1. It was developed by Vladimir Vuskovic at the Institute of Robotics at the ETH Zurich. In the tissue aspiration experiment the aspiration instrument is put against the target tissue and a weak vacuum is generated inside the tube by connecting it to a low-pressure reservoir. This setup guarantees that the aspiration pressure does not fall below the value preset in the reservoir. The maximum aspiration pressure applied in the tissue aspiration experiments is approximately 120 [mbar]. During the aspiration experiments no peculiar observations, like e.g. water droplets on the surface of the aspirated tissue, were made. The diameter of the aspiration hole in the base of the aspiration tube is 10 [mm]. At the maximum aspiration pressure a relative displacement of the tip of the tissue surface of 1 [mm] to 3 [mm] is observed. The relative tip displacement resulting in the experiments is strongly related to the stiffness of the aspirated tissue. The maximum stretches (ratio of deformed to undeformed material length) observed in the aspirated tissue are approximately $\lambda \approx 1.5$. A small mirror, placed next to the aspiration hole at the bottom of the tube, reflects the side view of the aspirated tissue towards the video camera placed on top of the instrument. An optic fibre, which is connected to a light source, illuminates the tissue surface. The video camera grabs images of the aspirated tissue with a frequency of approximately 25 [Hz]. The aspiration pressure is measured simultaneously with a pressure sensor. The grabbed images are processed *on-line* in order to save computer memory. Contour extraction from the grabbed images is done in a dual process. Each image is processed with a thresholding algorithm and an edge extraction algorithm. The very easy to interpret but not very accurate result of the thresholding algorithm is combined with the multiple, very accurate, candidate points for the profile from the edge extraction. Through a minimization process very accurate profile results are obtained from a superposition of the two data sets. The schematic diagram in Fig. 2.2 depicts this image evaluation method.

Only the profile of the aspirated tissue, represented by the outermost contour of the surface in the side-view, is used to characterize the tissue

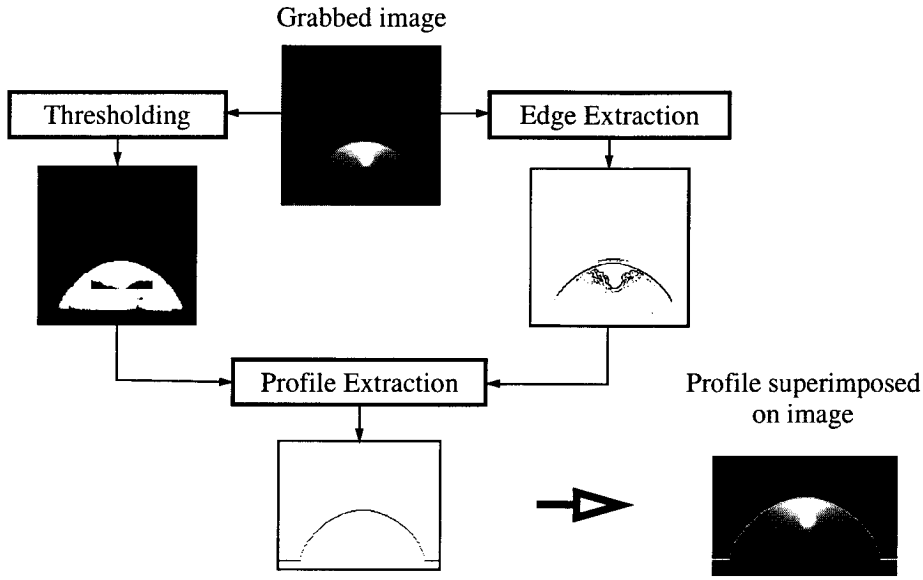

Fig. 2.2 Profile extraction

deformation. This simplification bases on the assumption of axisymmetric conditions in the aspiration experiment. Due to their special fibrous or layered structure soft biological tissues are in general anisotropic. The data published by Farshad (Farshad, 1999) for the pig kidney e.g. shows a pronounced anisotropy of the pig kidney cortex depending on the orientation of the tissue sample in the kidney. For samples lying in the tangential direction a nominal stress value of 0.2 [MPa] is obtained at a compression ratio of 1.35 and for samples in the radial direction at a compression ratio of 1.55 (in uniaxial compression tests). This data results from averaged measurements which were used to model the pig kidney cortex in finite element simulations. Due to the anisotropy of the soft tissues the condition of axisymmetry will probably never be met exactly in our aspiration experiments.

Two data sets result from the experiments: the aspiration pressure history and the profile history. This data is later used to determine the parameters in the chosen constitutive equation for the tissue. The tissue aspiration experiment has the advantage of setting well defined boundary conditions. Since the deformation measurement in the aspiration experiment is a relative measurement performed with respect to the base of the aspiration tube only negligible influence of the experimenter's trembling is expected. Rigid body motions of the organ do not influence on the measurement (which is in contrast to the indentation technique, where rigid body

motions strongly influence on the measured force-indentation curve)

A strong influence on the aspiration experiment results from the contact conditions between the aspirated tissue and the instrument, i.e. that friction plays an important role. The initial state of stress in the tissue represents one of the biggest unknowns. Tissue under gravitational load is never in a state free of stress (Fung, 1993, pp. 349-352; Fung, 1984). Research regarding the zero stress state of soft tissues concentrates on the cardiovascular system. Due to the special situation encountered in vascular systems (cylindrical geometry and prestressed tissues) the results of this research cannot be transferred to tissues of other organs. However, no quantitative data for initial stresses present in vascular tissues free of any external load was found in the literature. The stresses induced by the aspiration experiment are assumed to be much larger than any stresses present in the undeformed tissue. The influence of these initial stresses on the identification is expected to be negligible. In the following our work is therefore based on the assumption of a stress-free initial configuration.

Chapter 3

Continuum Mechanics for soft tissues

3.1 Mechanical properties of soft biological tissues

The diversity of mechanical properties encountered in soft biological tissues is huge. Soft organic tissues are characterized by very complex mechanical behaviour. They show non-linear, anisotropic, viscoelastic and in some cases also viscoplastic behaviour. Tissues often have a layered, a fibrous or an even more complicated structure. The mechanical properties of soft tissues are in general inhomogeneous. The perfusion of the organs and of their constituting tissues is also known to play an important role regarding their mechanical properties.

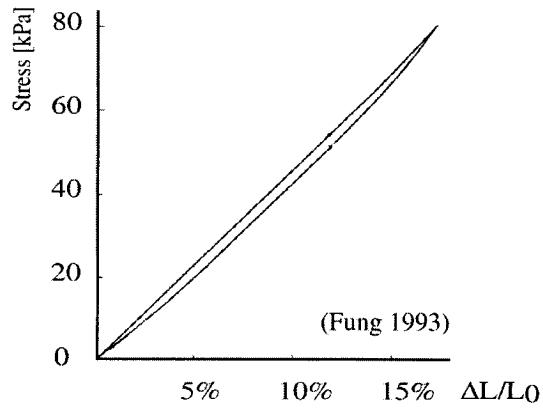

Fig. 3.1 Stress-strain curve for elastin

A very important component of many tissues is elastin. Elastin provides

elasticity to arteries, veins and lung parenchyma and keeps skin smooth. It is known that in humans the gene responsible for synthesizing elastin is turned off at puberty. Elastin is probably the component with the most linear elastic properties of all soft tissue components (Fig. 3.1). Elastin shows such linearly elastic properties up to stretches of $\lambda = (\Delta L + L_0) / L_0 \approx 1.6$, where ΔL is the material elongation and L_0 is its initial length. Additionally, elastin shows only very little hysteresis in loading and unloading. This hysteresis nevertheless proves the presence of an energy dissipation mechanism in the material.

Another very important component of soft and also hard biological tissues is collagen. It is one of the most important substances of our body and it is encountered in a variety of structural forms. Collagen is the main load carrying element in blood vessels, skin, tendons, cornea, bone, etc. The mechanical properties result from the structure of the collagen molecules. These molecules wind themselves together into fibrils; these fibrils are organized into fibres and the fibres into various tissues. The extensibility of collagen is much smaller than the one of elastin ($\lambda \approx 1.1$).

3.2 Stress-strain relationship of soft tissues

There are mainly two sources of elasticity in soft biological tissues. The first source of elasticity is due to changes of internal energy whereas the second one is due to changes of entropy (Fung, 1993; pp. 242). Change of

(Fung 1993)

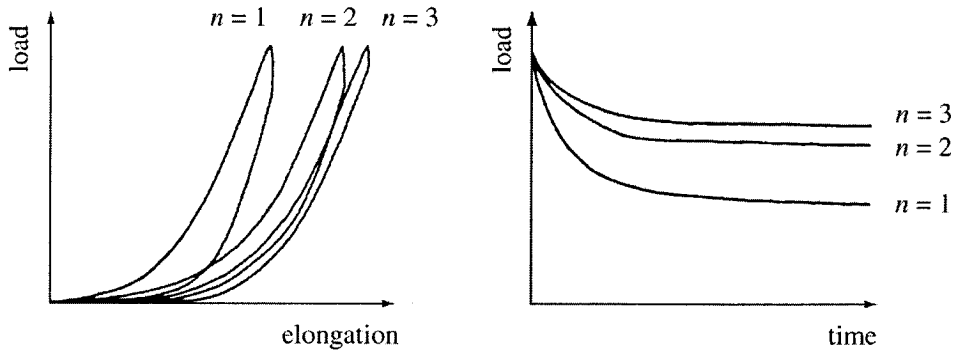

Fig. 3.2 Preconditioning of tissue, n denotes the number of loading cycles. In the diagram on the left-hand side the strain rate is kept constant, whereas in the figure on the right-hand side the material is kept at a constant pre-stretch and the material relaxation is recorded

entropy occurs in tissues whenever changes of orientation or waviness of fibres during loading or unloading occur.

A typical load-elongation and a load-time (relaxation) diagram for soft tissue is shown in Fig. 3.2. With repeated loading cycles the load-deformation curves shift to the right in a load-elongation diagram (n is the number of the current load cycle) and the hysteretic effects diminish (left-hand side of Fig. 3.2). In a load-time diagram the load-time curves shift upwards with increasing repetition number n (right-hand side of Fig. 3.2). By repeated cycling, eventually a steady state is reached at which no further change will occur unless the cycling routine is changed. In this state the tissue is said to be preconditioned. Any change of the lower or upper limits of the cycling process requires new preconditioning of the tissue. Preconditioning occurs due to internal changes in the structure of the tissue. Hysteresis, non-linearity, relaxation and preconditioning are common properties of all soft tissues, although the observed degree varies.

3.3 Viscoelasticity of soft tissues

The hysteresis in the left-hand side of Fig. 3.2 is caused by the viscoelastic properties of the soft biological tissue. In a viscoelastic material the history of strain affects the stresses observed in the material. Loading and unloading of a viscoelastic material occur on different stress-strain paths. If only small strains are considered the hysteresis of most biological tis-

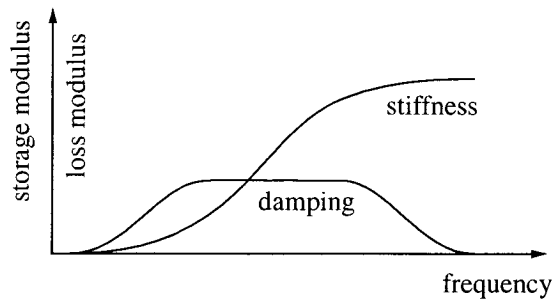

Fig. 3.3 Qualitative behaviour of damping and stiffness of soft tissues

sues shows only little dependence on the strain rate over several decades of strain rate variation. It is however not clear whether this fact holds also for large tissue deformations. Liu (Liu, 1998) measured the rheological properties of bovine liver tissue. The measured shear loss modulus G'' (see section 3.5) constantly increased from 400 [N/m^2] to 1000 [N/m^2] for an exci-

tation frequency varying between 0.005 [Hz] and 10 [Hz]. His results additionally indicate that bovine liver tissue has a linear viscoelastic stretch limit of $\lambda \approx 1.002$, which is much smaller than the stretches considered in this work. Insensitivity of the material to stretch rate over several decades cannot be modelled with simple viscoelastic models such as a single spring-dashpot element. A viscoelasticity model with a single spring-dashpot element shows a maximum hysteresis loop at a certain strain rate whereas all other strain rates show a smaller hysteresis loop (see Neubert, 1963). A constitutive model consisting of a discrete number of spring-dashpot elements consequently results in a hysteretic material behaviour with maximum dissipation at discrete strain rates. If the relaxation times of the different elements are chosen adequately a series of spring-dashpot elements can be used to approximate a continuous relaxation spectrum. Living tissues often show a viscoelastic behaviour as shown qualitatively in Fig. 3.3. In Fig. 3.3 the viscoelastic material properties are characterized by storage and loss modulus, which are concepts only valid in linear elasticity.

3.4 The basics of non-linear continuum mechanics

Amongst the many approaches known for soft tissue modelling continuum mechanics is probably the only physically correct method. A continuum mechanical formulation together with a corresponding finite element calculation of soft tissue deformations might not be the most efficient formulation, at least from a computational point of view, but it is certainly the approach with a thorough theoretical background. In continuum mechanics two classes of approaches to model soft tissues may be distinguished:

- The first class of formulations, representing a bottom up approach, tries to include structural aspects of the micro-mechanical level (Horowitz, 1988; Kimmel, 1987). Any mechanical properties caused by the tissues' micro-mechanical structure, like e.g. anisotropy, are accounted for very naturally in this approach. Material models within this class in many cases contain a large number of material parameters. These parameters are often related to structural aspects at the microscopical level of the tissue and are therefore difficult to determine without any *a priori* knowledge of the material structure.
- The second class of tissue models bases its material laws on homogenized formulations paying less attention to the micromechanical tissue structure. In most of these cases strain energy functions are used to

describe the mechanical tissue properties. Anisotropy e.g., can be included by employing strain energy functions depending on more quantities than only the three invariants of the strain tensor needed to model isotropy (Ogden, 1997, pp. 211-212).

Although this latter approach at a first glance may seem simpler than the bottom up models it often becomes as complex as the micromechanical approaches, if it is adapted to account for equivalently detailed mechanical tissue properties.

3.4.1 Deformation and strain

In continuum mechanics a reference configuration and a deformed configuration of the considered continuum are distinguished. The reference

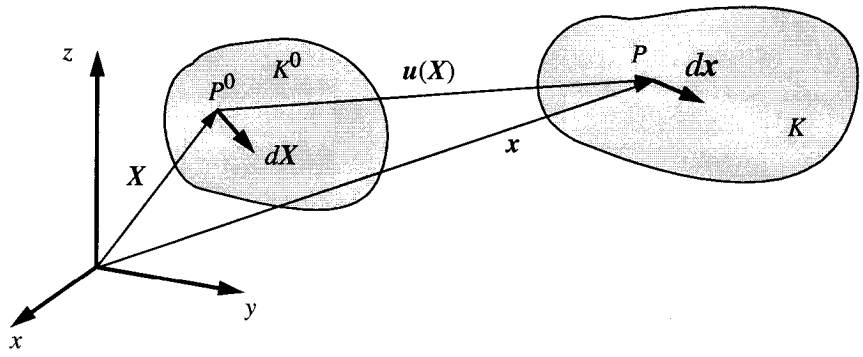

Fig. 3.4 Reference configuration K^0 and deformed configuration K

configuration is denoted by K^0 and the current deformed configuration by K (see Ogden, 1997; Bathe, 1996). The current configuration and the reference configuration are connected through a displacement vector $u(X)$, where X is the position vector in the undeformed configuration K^0 (see Fig. 3.4). In the following, the usual convention of non-linear continuum mechanics with uppercase letters for quantities belonging to the reference configuration K^0 and lowercase letters for quantities of the current configuration K is used. The summation convention is applied. An infinitesimal vector dX at the point P^0 in the reference configuration is mapped to the infinitesimal vector dx at the point P in the deformed configuration. This mapping leads to the definition of the deformation gradient F, which in component representation is

$$F_{ij} = \frac{\partial x_i}{\partial X_j}, \tag{3.1}$$

or

$$dx_i = F_{ij} dX_j \,. \tag{3.2}$$

The deformation gradient F relates the infinitesimal vector dX to the infinitesimal vector dx. A measure of strain, being invariant under rigid body rotations, can be defined by

$$\boldsymbol{E} = \frac{1}{2}(\boldsymbol{F}^T\boldsymbol{F} - \boldsymbol{I}) = \frac{1}{2}(\boldsymbol{C} - \boldsymbol{I}) \,, \tag{3.3}$$

where E denotes the *Green-Lagrange* strain tensor and C is called the *right Cauchy-Green* deformation tensor. The Green-Lagrange strain tensor can also be expressed with the displacement vector $u(X)$

$$E_{ij} = \frac{1}{2}(u_{i,j} + u_{j,i} + u_{k,i}u_{k,j}) \,, \tag{3.4}$$

where the comma denotes derivation with respect to the coordinate that follows.

For small deformations and rotations the Green-Lagrange strain tensor E is equal to the strain tensor ϵ used in linear continuum mechanics

$$\epsilon = \frac{1}{2}(u_{i,j} + u_{j,i}) \approx E_{ij} \,. \tag{3.5}$$

The displacement gradient $u_{i,j}$ is related to the deformation gradient F by

$$u_{i,j} = \frac{\partial u_i}{\partial X_j} = \frac{\partial (x_i - X_i)}{\partial X_j} = F_{ij} - \delta_{ij} \,. \tag{3.6}$$

The deformation gradient F can be decomposed (polar decomposition) in a symmetric matrix U or V and an orthogonal matrix R

$$\boldsymbol{F} = \boldsymbol{R}\boldsymbol{U} = \boldsymbol{V}\boldsymbol{R} \,, \tag{3.7}$$

where R represents a pure rigid body rotation and both U and V represent a pure strain. U is called the *right stretch tensor* and V the *left stretch ten-*

sor. The eigenvalues $\lambda_i(U)$ are called the *principal stretches.* The *stretch* of a general line element can be defined as follows. Let M and m be unit vectors along dX and dx. Then, from eq. (3.2)

$$m|dx| = FM|dX| \text{ and hence } |dx|^2 = M \cdot (F^T FM)|dX|^2 . \quad (3.8)$$

or

$$\frac{|dx|}{|dX|} = |FM| = \{M \cdot (F^T FM)\}^{1/2} = \lambda(M), \quad (3.9)$$

which defines $\lambda(M)$, the stretch in the direction of M at X, as the ratio of current to reference lengths of a line element which was in the direction M in the reference configuration. The quantity $\hat{\lambda} = \lambda(M) - 1$ is called the *extension ratio* in the direction of M. With eq. (3.7) in eq. (3.3) follows that the Green-Lagrange strain tensor E does not depend on rigid body rotations, since

$$E = \frac{1}{2}(F^T F - I) = \frac{1}{2}((RU)^T RU - I) = \frac{1}{2}(U^2 - I) . \quad (3.10)$$

Rigid body translations, represented by a constant displacement field, do not have any influence on E since the deformation gradient F in eq. (3.1) is then equal to unity.

The infinitesimal volume element dV in the reference configuration K^0 and in the deformed configuration K, denoted by dv, are related through

$$dv = det(F)dV = (det(C))^{1/2} dV. \quad (3.11)$$

3.4.2 Stress

The *second Piola-Kirchhoff* stress tensor S is work conjugate to the Green-Lagrange strain tensor E and is defined through

$$S = det(F)F^{-1}\sigma F^{-T}, \quad (3.12)$$

where σ is the well known *Cauchy* stress tensor. Work conjugate means that the following relation holds

$$S \bullet \dot{E} = det(F)(\sigma \bullet D), \quad (3.13)$$

where D is the symmetric part of the velocity gradient L

$$\boldsymbol{L} = \partial \boldsymbol{v} / \partial \boldsymbol{x} = \boldsymbol{D} + \boldsymbol{W},$$

$$\boldsymbol{D} = \frac{1}{2}(\boldsymbol{L} + \boldsymbol{L}^T) = \boldsymbol{D}^T, \qquad \boldsymbol{W} = \frac{1}{2}(\boldsymbol{L} - \boldsymbol{L}^T) = -\boldsymbol{W}^T. \quad (3.14)$$

In eq. (3.13) the inner product $\boldsymbol{A} \cdot \boldsymbol{B} = tr(\boldsymbol{A}\boldsymbol{B}^T)$ is used. From eq. (3.12) follows that the second Piola-Kirchhoff stress tensor $\boldsymbol{S}$ is symmetric since due to the principle of momentum also the Cauchy stress tensor σ is symmetric.

In the following sections the concept of *hyperelasticity* is used. An elastic material for which a strain-energy function exists is called a *Green elastic* or *hyperelastic* material. The mechanical properties of a hyperelastic material can be characterized by a strain energy function $\tilde{w}$. The stress-strain relationship is then obtained from

$$\boldsymbol{S} = \frac{\partial \tilde{W}}{\partial \boldsymbol{E}} = 2\frac{\partial \tilde{W}}{\partial \boldsymbol{C}}. \quad (3.15)$$

The energy stored in a deformed hyperelastic material is independent of the deformation path and is determined only by the value of the strain energy function $\tilde{w}$. It can be shown that for hyperelastic isotropic materials $\tilde{w}$ is a function of the three invariants of the deformation tensor $\boldsymbol{E}$ or $\boldsymbol{C}$ only

$$\tilde{W} = \tilde{W}(I_1, I_2, I_3), \quad (3.16)$$

where

$$I_1 = C_{ii},$$

$$I_2 = \frac{1}{2}(I_1^2 - C_{ij}C_{ij}),$$

$$I_3 = det(\boldsymbol{C}). \quad (3.17)$$

From eq. (3.11) follows that for incompressible materials ($det(\boldsymbol{C}) = 1$) the strain energy function is a function of the first and second invariant of the deformation tensor $\boldsymbol{C}$ only.

3.4.3 Strain energy functions

Most rubbery materials are modelled as incompressible materials. Due to their high water content also tissues are in general assumed to be incompressible. The *Mooney-Rivlin* form of the strain energy function is often employed for rubber materials

$$\tilde{W} = \mu(I_1 - 3) + \alpha(I_2 - 3), \tag{3.18}$$

whereas the also widely used *neo-Hookean* form results from eq. (3.18) by neglecting the dependency of the strain energy function on the second invariant

$$\tilde{W} = \mu(I_1 - 3). \tag{3.19}$$

A material characterized by the Mooney-Rivlin or the neo-Hookean strain energy function shows a more or less linear or even flattening force-elongation behaviour in uniaxial tension. This mechanical behaviour is seldom encountered in soft biological tissues. A formulation better suited for soft tissue modelling is given by the following strain-energy function

$$\tilde{W} = \frac{\mu}{\gamma}(e^{\gamma(I_1 - 3)} - 1) + \alpha(I_2 - 3). \tag{3.20}$$

With the parameter γ [-] the exponential formulation from eq. (3.20) is able to capture different degrees of material non-linearity. In contrast to the parameter γ both the parameters μ [N/m^2] and α [N/m^2] have an influence on the material stiffness in the undeformed configuration (compare also eq. (3.40)), i.e. both contribute to the *Young's modulus*. The material formulation in eq. (3.20) is especially suited to model pronounced non-linear material behaviour. For pronounced non-linear materials the parameter γ will assume rather large values, i.e. $\gamma > 1$. For large deformations ($\lambda > 1.2$) and a pronounced material non-linearity the contribution to the stresses of the first term on the right-hand side of eq. (3.20) will usually dominate over the contribution of the second term. When a parameter fit with emphasis on the material behaviour at large deformations is performed, the dependence on the second invariant in eq. (3.20) might thus be omitted. For moderate stretches (up to $\lambda \approx 1.2$) the term depending on the second invariant can be useful to match the material model to the initial tangential elastic behaviour of the studied material. However, for small

and to some extent also for moderate stretches most biological materials behave nearly linear elastic and then a material formulation different from the one in eq. (3.20) is certainly better suited to model the mechanical behaviour. From a numerical point of view it is preferable to omit the dependence of the strain energy function from eq. (3.20) on the second invariant. The calculation of the stresses is computationally more expensive if the dependence on the second invariant is included. In the finite element code it is computationally cheaper to formulate the elastic stresses in the element on the basis of the nominal stress tensor $N_{ij} = F_{ik}S_{kj}$. For a hyperelastic material with a strain energy function according to eq. (3.22) the nominal stress can then be written as

$$N_{ij} = aF_{ij} + bF_{ij}^{-1} + cF_{ik}F_{rk}F_{rj}, \tag{3.21}$$

where a, b and c depend on the derivatives of the strain energy functions $\hat{W}$ and W_H with respect to the reduced invariants. The factor c is equal to zero if the strain energy $\hat{W}$ does not depend on the second reduced invariant J_2. In this case the evaluation of eq. (3.21) is computationally cheaper than in the general case in which $\hat{W}$ depends also on the second reduced invariant J_2. For a definition of $\hat{W}$, W_H and J_1, J_2, J_3, please see section 3.4.4.

The strain energy function from eq. (3.20) was proposed in this or similar forms by Blatz (Blatz, 1969), Veronda and Westmann (Veronda, 1970), Demiray (Demiray, 1972) and others. In the following this material formulation is referred to as *Veronda-Westmann* material. If the dependence on the second invariant in eq. (3.20) is omitted we refer to it as *reduced Veronda-Westmann* material.

3.4.4 Nearly incompressible materials

In a totally incompressible isotropic material no one-to-one correspondence between stress and strain exists (you may e.g. superpose an arbitrary hydrostatic pressure on an incompressible isotropic material without changing the deformation). In the case of nearly or totally incompressible materials the purely displacement based finite element method therefore lacks of accuracy. This effect is known as *locking* of the finite elements. Using a very fine mesh in some cases helps to overcome these inaccuracies. Since the computational cost of the solution in non-linear problems is already considerable finer meshes do not represent a desirable alternative.

In contrast, mixed formulations which use both displacement and pressure degrees of freedom, have shown to be very efficient and accurate in the solution of problems involving nearly or totally incompressible materials. Since in a mixed formulation the pressure is to be treated as a separate degree of freedom the employed material laws have to be modified. To separate the hydrostatic pressure from the stress tensor, the following strain energy function is proposed by Sussman and Bathe (Sussman, 1987)

$$\bar{W} = \hat{W}(J_1, J_2) + W_H(J_3), \tag{3.22}$$

where J_1, J_2, J_3 denote the reduced invariants of the deformation tensor C and $W_H(J_3)$ represents a hydrostatic work term. $\hat{W}(J_1, J_2)$ is used instead of $\tilde{W}(I_1, I_2)$ because the invariants of the deformation tensor C are replaced by their respective reduced invariants in eqs. (3.18) to (3.20) (Flory, 1961; Simo, 1985).

The reduced first and second invariant J_1 and J_2 are defined as first and second invariant of the deformation tensor C^*, where

$$C^* = I_3^{-1/3} C. \tag{3.23}$$

C^* is a unimodular tensor with $det(C^*) = 1$ and represents a decomposition of the deformation tensor C in a purely isochoric distortional part C^* and a dilatational part $I_3^{1/3} I$

$$C = (I_3^{1/3} I) C^*, \tag{3.24}$$

since with eq. (3.11)

$$dv = [det(C^*)]^{1/2} dV = [I_3^{-1} det(C)]^{1/2} dV = dV. \tag{3.25}$$

This means, that the deformation described by C^* is isochoric. The third reduced invariant J_3 is defined by

$$J_3 = det(F) = [det(C)]^{1/2} = \sqrt{I_3}. \tag{3.26}$$

The hydrostatic pressure in a material is given by

$$p = -\frac{1}{3}\sigma_{ii} = -\frac{1}{3J_3} S_{ij} C_{ij}. \tag{3.27}$$

With eq. (3.15) the second Piola-Kirchhoff stresses in the material with a strain energy function corresponding to eq. (3.22) are

$$S_{ij} = \frac{\partial \hat{W}}{\partial J_1} 2I_3^{-1/3}\left(\delta_{ij} - \frac{1}{3} I_1 C_{ij}^{-1}\right)$$

$$+\frac{\partial \hat{W}}{\partial J_2} 2I_3^{-2/3}\left(I_1\delta_{ij} - C_{ij} - \frac{2}{3} I_2 C_{ij}^{-1}\right) + \frac{\partial W_H}{\partial J_3} J_3 C_{ij}^{-1} . \tag{3.28}$$

Applying eq. (3.27) to eq. (3.28) and using the definitions from eq. (3.17) yields

$$p = -\frac{\partial W_H}{\partial J_3} . \tag{3.29}$$

Eq. (3.29) shows that only the term W_H contributes to the hydrostatic pressure in the material. The Cauchy stresses resulting from $\hat{W}$ are deviatoric stresses. For the derivation of the above results it is necessary to know the derivatives of the invariants with respect to the strain tensor $\boldsymbol{E}$. These derivatives can be found in Appendix A.

Introducing the hydrostatic work term proposed by Sussman and Bathe (Sussman, 1987), which is presented in Chapter 4, leads to the following general form for a nearly incompressible isotropic material

$$\overline{W} = \hat{W}(J_1, J_2) + \frac{1}{2}\kappa(J_3 - 1)^2 , \tag{3.30}$$

where κ [N/m^2] is the bulk modulus of the material. The bulk modulus κ in eq. (3.30) determines the compressibility of the material. κ is assumed to be independent of the material deformation and is set constant. Since the bulk modulus κ is assumed to be constant and the material stiffness resulting from $\hat{W}(J_1, J_2)$ increases with increasing deformation a deformation dependent volume preservation is observed for the nearly incompressible material. An applied deformation will in general cause the material to become orthotropic; the material is isotropic only in the undeformed reference configuration.

Apart from the size of the finite elements, the bulk modulus κ dominates the time step for the integration algorithm in the explicit finite element formulation when nearly incompressible material behaviour is considered.

The time step is given approximately by eqs. (4.18) to (4.20) and is additionally influenced by the shear modulus of the material. A large bulk modulus κ results in small time steps and thus in computationally expensive simulations, whereas small values of the bulk modulus κ result in strongly deformation dependent volume preservation for a material corresponding to eq. (3.30). The value of the bulk modulus κ thus plays an important role in the simulation of nearly incompressible materials with explicit finite element methods.

To study the effects caused by the assumption of a constant bulk modulus we first study the nearly incompressible neo-Hookean material with the following strain energy function

$$\overline{W} = \mu(J_1 - 3) + \frac{1}{2}\kappa(J_3 - 1)^2 .$$

In the undeformed material configuration the Young's modulus E^e for the neo-Hookean material can be derived from

$$dS_{ij} = \frac{\partial S_{ij}}{\partial E_{kl}} dE_{kl} = C_{ijkl} dE_{kl}, \tag{3.31}$$

where (see also eq. (C.3))

$$C_{ijkl} = \frac{4}{9}\mu J_1 C_{ij}^{-1} C_{kl}^{-1} + \frac{4}{3}\mu J_1 C_{ik}^{-1} C_{jl}^{-1}$$

$$-\frac{4}{3}\mu I_3^{-1/3}(\delta_{ij} C_{kl}^{-1} + \delta_{kl} C_{ij}^{-1}) + \kappa J_3(2J_3 - 1) C_{ij}^{-1} C_{kl}^{-1}$$

$$-2\kappa J_3(J_3 - 1) C_{ik}^{-1} C_{jl}^{-1} . \tag{3.32}$$

The undeformed material configuration, in which the material is isotropic, is now considered. The conditions for the undeformed material $C_{ij} = C_{ij}^{-1} = \delta_{ij}$ and $J_1 = 3$, $J_3 = 1$ are introduced into eq. (3.32). Comparison of the result with the following form of the linear isotropic material law

$$C_{ijkl} = \bar{\lambda}\delta_{ij}\delta_{kl} + 2\bar{\mu}\delta_{ik}\delta_{jl} \tag{3.33}$$

yields the Young's Modulus E^e

$$E^e = \frac{18\kappa\mu}{3\kappa + 2\mu}, \tag{3.34}$$

and the Poisson's ratio ν of the undeformed neo-Hookean material

$$\nu = \frac{3\kappa - 4\mu}{6\kappa + 4\mu}. \tag{3.35}$$

Eq. (3.33) represents the constitutive equation for an isotropic material expressed in the *Lamé constants* $\bar{\lambda}$ and $\bar{\mu}$. The following relations have been used in the above derivation

$$\bar{\lambda} = \frac{\nu E^e}{(1+\nu)(1-2\nu)}, \qquad \bar{\mu} = \frac{E^e}{2(1+\nu)}. \tag{3.36}$$

Taking the limit $\kappa \to \infty$ in eqs. (3.34) and (3.35) the well known result for the totally incompressible neo-Hookean material is obtained

$$E^e = 6\mu, \qquad \nu = 1/2. \tag{3.37}$$

If the nearly incompressible neo-Hookean material is deformed the corresponding elastic moduli describing the material are deformation dependent.

A simple deformation is now applied to the neo-Hookean material which allows to study the behaviour of the material depending on the deformation. Let the applied deformation be characterized by the following deformation gradient

$$F = \begin{bmatrix} \lambda & 0 & 0 \\ 0 & \tilde{x} & 0 \\ 0 & 0 & \tilde{x} \end{bmatrix} = \begin{bmatrix} \lambda_1 & 0 & 0 \\ 0 & \lambda_2 & 0 \\ 0 & 0 & \lambda_3 \end{bmatrix}. \tag{3.38}$$

The deformation consists of an extension or compression λ of the material in the direction of the first coordinate axis and a lateral contraction or expansion $\tilde{x}$. In our case the lateral stretch $\tilde{x}$ is obtained by requiring the lateral material surfaces to be free of tension. In Fig. 3.5 the ratio of the

deformed volume to the undeformed reference volume $dv/dV = J_3$ can be seen to strongly depend on the ratio of κ/μ. The bulk modulus κ has to be chosen large enough as compared to the material parameter μ to obtain a mostly deformation independent volume preservation in the deformed material.

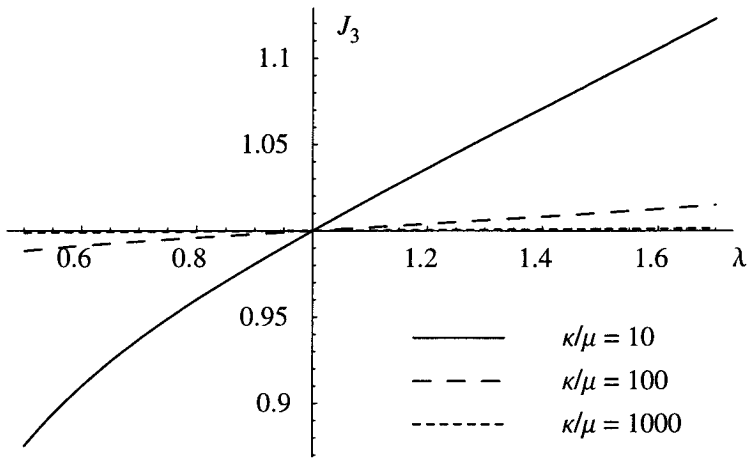

Fig. 3.5 Volume preservation of compressible neo-Hookean material depending on deformation

The same procedure as for the neo-Hookean material is now applied to the reduced Veronda-Westmann material from eq. (3.20) (the material constant α is set to zero). The Young's modulus and the Poisson's ratio in the undeformed material configuration can be obtained from (see also eq. (C.5))

$$
\begin{aligned}
C_{ijkl} = {} & 4\mu e^{\gamma(J_1-3)}(\gamma I_3^{-2/3}\delta_{kl}\delta_{ij} \\
& -\frac{1}{3}I_3^{-1/3}(1+\gamma J_1)(\delta_{ij}C_{kl}^{-1}+\delta_{kl}C_{ij}^{-1}) \\
& +\frac{1}{9}J_1(1+\gamma J_1)C_{ij}^{-1}C_{kl}^{-1}+\frac{1}{3}J_1C_{ik}^{-1}C_{lj}^{-1}) \\
& +\kappa J_3(2J_3-1)C_{ij}^{-1}C_{kl}^{-1}-2\kappa J_3(J_3-1)C_{ik}^{-1}C_{lj}^{-1}\,,
\end{aligned}
\tag{3.39}
$$

which with eq. (3.33) yields

$$E^e = \frac{18\kappa\mu}{3\kappa + 2\mu}, \qquad \nu = \frac{3\kappa - 4\mu}{6\kappa + 4\mu}. \tag{3.40}$$

By comparing eq. (3.40) with eqs. (3.34) and (3.35) the reduced Veronda-Westmann material and the neo-Hookean material are both seen to have the same Young's moduli in the undeformed material configuration. In the reduced Veronda-Westmann material formulation the initial material stiffness is only influenced by the parameters μ and κ. The influence of the parameter γ augments with increasing material deformation. In Fig. 3.6

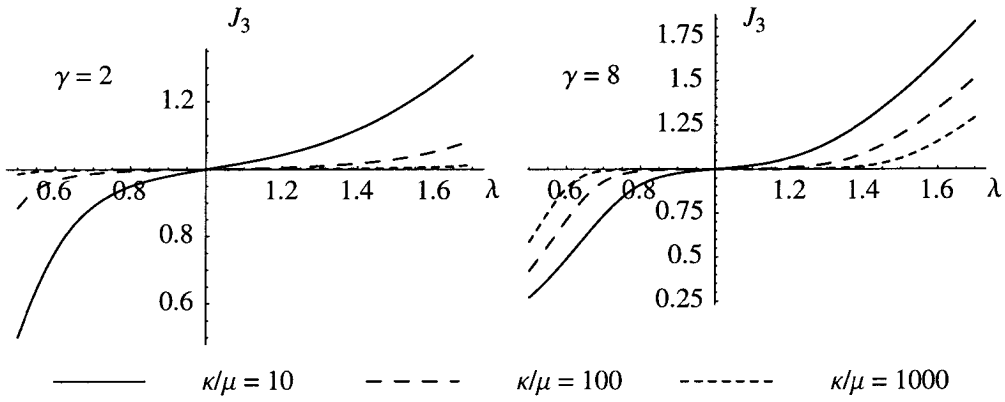

Fig. 3.6 Volume preservation of compressible reduced Veronda-Westmann material depending on deformation

the volume preservation for the two values $\gamma = 2$ and $\gamma = 8$ of the reduced Veronda-Westmann material undergoing a deformation characterized by eq. (3.38) is shown for different values of the ratio κ / μ. It is seen that with increasing values of the non-linearity γ an increasing bulk modulus κ is required in order to assure near incompressibility of the modelled material.

3.5 Modelling viscoelastic behaviour

Viscoelasticity is a very important aspect in modelling the mechanical properties of soft tissues. Various approaches to model viscoelastic tissue behaviour can be found in the literature:

- *Biphasic* formulations model tissue as composed of an incompressible fluid and an incompressible hyperelastic matrix. The viscoelastic material properties arise from the relative motion of the fluid through the matrix. Biphasic material formulations are frequently employed to

model cartilaginous tissues (Mow, 1980). In most of these models only small deformations are considered.

- Another class of models uses internal variables to model viscoelastic material properties. Evolution equations define the dependency of the internal variables on the deformation history of the material. The evolution equations for the internal variables are usually given as differential equations and have to be integrated over time (Rubin, 1998; Johnson, 1995).
- An approach widely used in biomechanics is the *quasi-linear viscoelasticity* formulation. The stresses in the material, which themselves may result from a non-linear stress-strain relation, are linearly superposed with respect to time (Fung, 1993; Woo, 1993; Puso, 1998).

With regard to the inverse parameter estimation a small number of unknown model parameters is preferable. Regarding the number of unknown parameters, none of the above approaches contains much less model parameters than the others. A decision for one of the above approaches is thus not influenced by this aspect. The quasi-linear viscoelasticity formulation is used since it represents a straightforward expansion of the elasticity models already used previously in this work. Additionally, the model of quasi-linear viscoelasticity allows a simple implementation into our explicit finite element code used in the virtual reality laparoscopy simulator.

To derive the basic concepts of quasi-linear viscoelasticity we start with the case of linear viscoelasticity

$$\sigma(t) = \boldsymbol{G}(t)\epsilon(0) + \int_0^t \boldsymbol{G}(t-s)\dot{\epsilon}(s)ds\,, \tag{3.41}$$

where the relaxation modulus matrix $G(t)$ may be replaced by a relaxation tensor to account for material anisotropy. The first term in eq. (3.41) is equal to zero if continuous straining of the material starting from an undeformed configuration is assumed. In the following it is assumed that this condition holds and the first term in eq. (3.41) is not further accounted for. The relaxation modulus for a uniaxial *Kelvin-Voigt* model (spring-dashpot element) is

$$G(t) = E_\infty + (E_0 - E_\infty)e^{-t/\tau}\,. \tag{3.42}$$

E_∞ and E_0 characterize the fully relaxed and the instantaneous response, respectively and τ is the relaxation time of the Kelvin-Voigt model. With eq. (3.42) in eq. (3.41) follows

$$\sigma(t) = \int_0^t G(t-s)\dot{\epsilon}(s)ds =$$

$$= E_\infty \epsilon(t) + \frac{E_0 - E_\infty}{E_\infty} \int_0^t E_\infty e^{-(t-s)/\tau} \dot{\epsilon}(s)ds =$$

$$= \sigma_\infty(t) + \frac{E_0 - E_\infty}{E_\infty} \int_0^t e^{-(t-s)/\tau} \dot{\sigma}_\infty(s)ds\,, \tag{3.43}$$

where

$$\sigma_\infty(t) = E_\infty \epsilon(t)\,.$$

Only the uniaxial case is considered in the above equations. Analogous to eq. (3.43) and in view of the implementation of the above formulation into a finite element code one can write

$$S(x, t+\Delta t) = S^e(C(x, t+\Delta t)) + \int_0^{t+\Delta t} G(t+\Delta t - s)\frac{\partial}{\partial s} S'(C(x, s))ds\,, \tag{3.44}$$

where $S(...)$ are the second Piola-Kirchhoff stresses, $G(t+\Delta t-s)$ is a reduced relaxation function and Δt is the time step of the finite element formulation. The above quasi-linear viscoelastic formulation was presented in a similar way by Fung (Fung, 1993). In contrast to Fung the reduced relaxation function is not required to fulfill the following condition

$$G(0) = 1\,. \tag{3.45}$$

The quasi-linear viscoelastic formulation was derived by analogy to eq. (3.43) whereas Fung used a more general derivation of the formulation (for details see Fung, 1993, pp. 278). The stresses $S^e(...)$ result from eq. (3.30) with eq. (3.15)

$$S^e(C(x, t+\Delta t)) = 2\frac{\partial \bar{W}}{\partial C(x, t+\Delta t)}, \tag{3.46}$$

whereas the stresses $S'(\ldots)$ result from

$$S'(C(x, s)) = 2\frac{\partial \hat{W}}{\partial C(x, s)}. \tag{3.47}$$

From eq. (3.44) it is seen that only the part $S'(C(x, s))$ of the stresses contributes to the history dependence of the stress-strain path. The pressure $p = -\kappa(J_3 - 1)$ in the material is treated as purely elastic. The stresses $S'(C(x, s))$ are related to a deviatoric Cauchy stress tensor $(\sigma_{dev})_{ii} = 0$.

As already described in section 3.3, soft tissues are often assumed to have strain rate insensitive damping characteristics over a wide range of strain rates. If viscoelasticity is modelled with internal spring-dashpot elements, each spring-dashpot element may be characterized by its time constant and its spring stiffness. The *loss modulus* for a spring-dashpot element, a measure for the energy dissipated in the material, is rate dependent with a pronounced maximum at an angular frequency depending on the relaxation time τ (see Fig. 3.7). In order to use the terminology of linear viscoelasticity eq. (3.41) is used

$$\sigma(t) = G(t)\epsilon(0) + \int_0^t G(t-s)\dot{\epsilon}(s)ds.$$

Introducing a harmonic excitation

$$\epsilon(t) = \epsilon_0 e^{i\omega t} \tag{3.48}$$

and assuming that all transient parts of the answer have decayed $(t \to \infty)$ yields

$$\sigma(t) = E^*(\omega)\epsilon(t) = (E'(\omega) + E''(\omega))\epsilon(t). \tag{3.49}$$

$E'(\omega)$ is the real part of the *complex modulus* $E^*(\omega)$ and represents the elastic part of the answer (*storage modulus*), whereas $E''(\omega)$ is the imaginary part of the complex modulus and is called the loss modulus. The loss modulus characterizes the energy dissipated in the material by internal damping. Fig. 3.7 shows that the loss modulus assumes its maximum value at

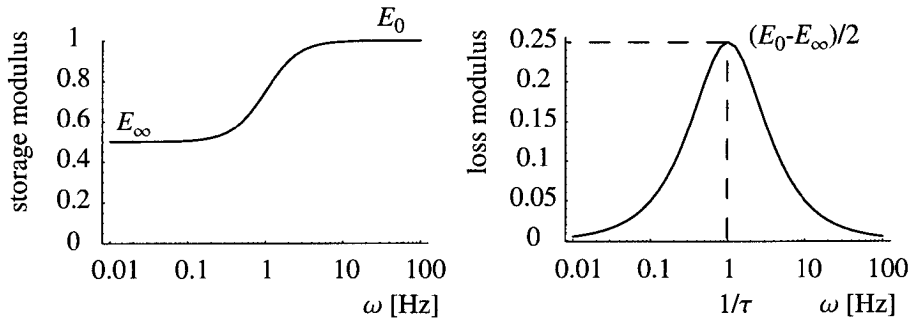

Fig. 3.7 Storage modulus and loss modulus for Kelvin-Voigt model

the frequency $\omega = 1/\tau$. Fig. 3.7 also shows that a single spring-dashpot element is not suited to model a rate independent loss modulus over a wide frequency range.

Combining a number of spring-dashpot elements with suitable relaxation times allows to model an arbitrary material damping behaviour. In Fig. 3.8 the storage modulus and the loss modulus for a series of 6 spring-dashpot

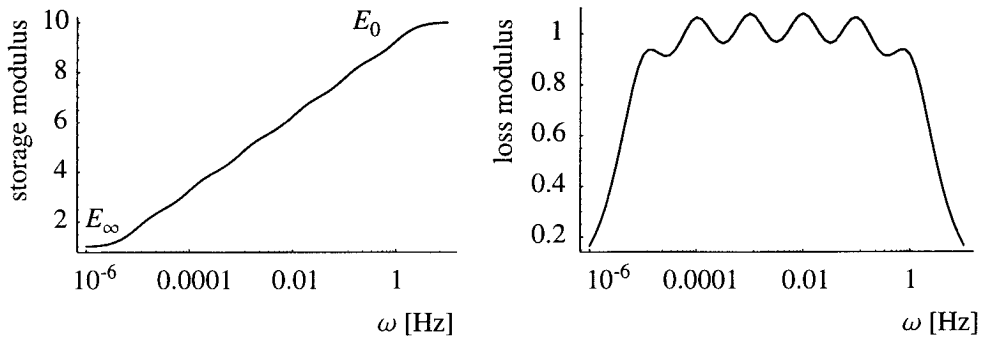

Fig. 3.8 Storage modulus and loss modulus for series of 6 spring-dashpot elements

elements in parallel with time constants τ spanning a range of 6 decades from 10^0 to 10^5 is shown. A constant loss modulus over a wider frequency range, as it is often assumed in the literature for soft tissues, can be approximated quite well with this discrete model (see Puso, 1998).

It is also possible to model a constant loss modulus over a wide frequency range with a continuous relaxation spectrum instead of the discrete spectrum presented above. However, the discrete exponential approximation of the reduced relaxation function $G(t)$ allows a computationally

much more efficient calculation of the convolution integral in eq. (3.44) than the continuous relaxation spectrum. The following reduced relaxation function $G(t)$ can be used to model a constant loss modulus over N_d decades of the frequency range

$$G(t) = E_\infty + \frac{E_0 - E_\infty}{N_d + 1} \sum_{i=0}^{N_d} e^{-t/\tau_i}$$

$$= E_\infty + \frac{E_0 - E_\infty}{N_d + 1} \sum_{i=0}^{N_d} e^{-t/10^{i+i_0}} . \tag{3.50}$$

The parameter i_0 describes the lowest discernible relaxation time $\tau_0 = 10^{i_0}$ and the parameter N_d is the span of the transition region in decades. With eq. (3.41) the storage modulus and the loss modulus for the relaxation modulus from eq. (3.50) are

$$E'(\omega) = E_\infty + \frac{E_0 - E_\infty}{N_d + 1} \sum_{i=0}^{N_d} \frac{(\omega\tau_i)^2}{1 + (\omega\tau_i)^2}$$

$$E''(\omega) = \frac{E_0 - E_\infty}{N_d + 1} \sum_{i=0}^{N_d} \frac{\omega\tau_i}{1 + (\omega\tau_i)^2} . \tag{3.51}$$

Comparison of eq. (3.50) with eq. (3.43) shows that E_∞ is the factor characterizing the fully relaxed answer $\sigma_\infty(t)$. Coming back to the quasi-linear formulation of eq. (3.44) one can write analogously

$$S(x, t+\Delta t) = S^e(C(x, t+\Delta t)) + \int_0^{t+\Delta t} \sum_{i=0}^{N_d} \left(c_i e^{-(t+\Delta t-s)/\tau_i} \frac{\partial}{\partial s} S'(C(x, s)) \right) ds . \tag{3.52}$$

By setting all weighting constants c_i equal to each other $c_i = c$, this approach leads to a good approximation of a constant loss modulus over the span of N_d decades (see Fig. 3.8). Here, the fully relaxed answer characterized by E_∞ in eq. (3.43) is replaced by the elastic answer $S^e(C(x, t+\Delta t))$ obtained from the strain energy function eq. (3.46).

For the integration of eq. (3.52) all the values of the second Piola-Kirchhoff stress tensor need to be saved over the whole time period $0 \ldots t+\Delta t$.

Additionally, in finite element calculations the values of the second Piola-Kirchhoff stress tensor need to be saved in all numerical sampling points of the volume integration. Already for models with only a small number of elements the needed computer memory is huge. An approximation of the convolution integral in eq. (3.52) very much reduces the amount of storage needed (see Puso, 1998). For simplicity $S'(C(x,s))$ is replaced by $S'(s)$

$$\int_0^{t+\Delta t}\left(\sum_{i=0}^{N_d} c_i e^{-(t+\Delta t-s)/\tau_i}\right)\frac{\partial}{\partial s}S'(s)ds$$

$$= \int_0^{t}\left(\sum_{i=0}^{N_d} c_i e^{-(t+\Delta t-s)/\tau_i}\right)\frac{\partial}{\partial s}S'(s)ds + \int_t^{t+\Delta t}\left(\sum_{i=0}^{N_d} c_i e^{-(t+\Delta t-s)/\tau_i}\right)\frac{\partial}{\partial s}S'(s)ds =$$

$$\approx \sum_{i=0}^{N_d} e^{-\Delta t/\tau_i} S_i^v(t) + \frac{S'(t+\Delta t)-S'(t)}{\Delta t}\int_t^{t+\Delta t}\left(\sum_{i=0}^{N_d} c_i e^{-(t+\Delta t-s)/\tau_i}\right)ds =$$

$$= \sum_{i=0}^{N_d}\left(e^{-\Delta t/\tau_i} S_i^v(t) + \frac{c_i}{\Delta t/\tau_i}(1-e^{-\Delta t/\tau_i})(S'(t+\Delta t)-S'(t))\right); \qquad (3.53)$$

where the history variable

$$S_i^v(t) = c_i\int_0^t e^{-(t-s)/\tau_i}\frac{\partial}{\partial s}S'(s)ds \qquad (3.54)$$

has been introduced. Partial integration and the approximation of the derivative $\partial(S'(s))/\partial s$ with a central difference rule led to the result of eq. (3.53). As can be seen from eq. (3.53) only the values of the history variable $S_i^v(t)$ and the values of $S'(t)$ from the last time step have to be saved in order to proceed to the next time step (here $S_i^v(t)$ is called a variable although it is not a variable but a tensor). The history variables $S_i^v(t)$ are initialized by setting $S_i^v(0) = 0$.

In explicit integration schemes the time step Δt is usually so small, that the error introduced by the above approximation is negligible. In implicit integration schemes rather small load steps and tight convergence criteria have to be used to ensure a good approximation of the convolution integral.

If the relaxation times τ_i assume large values as compared to the time step Δt, numerical problems can arise from the approximation presented in

eq. (3.53). For $\Delta t / \tau_i$, the factors

$$\frac{c_i}{\Delta t / \tau_i}(1 - e^{-\Delta t / \tau_i})$$

analytically tend to c_i, but due to round-off errors in the numerical evaluation the factors will tend to zero. This error can be avoided by using the series expansion

$$c_i(1 - 1/2(\Delta t / \tau_i) + 1/6(\Delta t / \tau_i)^2 - (1/24)(\Delta t / \tau_i)^3 + O((\Delta t / \tau_i)^4))$$

as an approximation of the above expression for small values of $\Delta t / \tau_i$.

Values for the smallest and the largest relaxation times determining the parameters i_0 and N_d can be taken from the literature (Decraemer, 1980, Woo, 1981) or have to be determined by experiments (see Chapter 6). A limit on the smallest relaxation time that can be determined with an aspiration experiment results from the sampling rate of the video system used to track the tissue deformation. The optical system in the aspiration tube has a maximum sampling frequency of 25 [Hz]. Due to the high communication bandwidth needed to deliver the image data from the video camera to the computer the image sampling frequency cannot be guaranteed to be constantly 25 [Hz]. Variations between 12 [Hz] and 25 [Hz] of the image sampling frequency are observed. Thus processes with a typical frequency of 6 [Hz] can at maximum be sampled. Processes with relaxation times much smaller than $T_{min} = 1/(6\ [s^{-1}]) \approx 0.17$ [s] can hardly be tracked with this system. Therefore the smallest relaxation time in the spectrum approximation relevant for the material properties in the aspiration experiments is set to $\tau \approx 0.1$ [s].

Seite Leer /
Blank leaf

Chapter 4

Finite element formulation

Apart from some very simple situations the partial differential equations resulting from a continuum-mechanical boundary value problem can only be solved with numerical methods. The complex geometry of the studied organs and the employed constitutive equations additionally complicate the solution of the problem. Finite element methods have become the standard method in solving continuum mechanical problems with complex geometry and complex material laws, especially when non-linear situations are encountered. Employing finite element methods to solve the governing continuum-mechanical equations means to solve these equations in a weak sense. The governing equations are not fulfilled exactly in every point of the considered continuum but only the integral form of the governing equations is required to be fulfilled over each finite element.

4.1 Modified strain energy function for u/p-formulation

As already mentioned earlier displacement based finite element formulations tend to lock if nearly or totally incompressible materials are considered, i.e. a loss of accuracy is observed in the computed response as material incompressibility is enforced. There are various methods to avoid element locking. To treat the hydrostatic pressure in the material as a separate degree of freedom proved to be very efficient to avoid element locking. This approach leads to a so called mixed displacement-pressure formulation or u/p-formulation (Sussmann, 1987; Simo, 1985). To allow the hydrostatic pressure to be treated as a separate degree of freedom

material models with a strain energy function corresponding to eq. (3.22) have to be used. As already shown, the hydrostatic pressure in the material then only depends on the hydrostatic work term W_H and thus can be treated as a separate degree of freedom. Sussman and Bathe (Sussman, 1987) proposed the following strain energy function W_H for the hydrostatic work term which together with eq. (3.22) yields

$$\overline{W} = \hat{W}(J_1, J_2) + W_H(J_3) = \hat{W}(J_1, J_2) + \frac{1}{2}\kappa(J_3 - 1)^2 . \tag{4.1}$$

For the derivation of the element equations the following strain energy function was suggested again by Sussman and Bathe (Sussman, 1987)

$$W = \overline{W} - \frac{1}{2\kappa}(\bar{p} - \tilde{p})^2 = \overline{W} + Q , \tag{4.2}$$

where κ is the bulk modulus of the material. $\tilde{p}$ is the separately interpolated pressure which represents an additional degree of freedom in the finite element formulation. $\bar{p}$ is the pressure which results from the material description in eq. (4.1) by using eq. (3.29)

$$\bar{p} = -\kappa(J_3 - 1) . \tag{4.3}$$

Since the bulk modulus κ in eq. (4.1) is set constant but the distortional material behaviour resulting from $\hat{W}(J_1, J_2)$ usually varies with varying strain, variable elastic moduli result from this specific material description. Some implications resulting from this approach were already discussed in section 3.4.4. In eq. (4.2) the pressure information $\bar{p}$ resulting from the material description (which is not available in the limiting case of total incompressibility with $J_3 \equiv 1$) is related to the separately treated pressure $\tilde{p}$. If in eq. (4.2) both pressure values $\bar{p}$ and $\tilde{p}$ are equal eq. (4.2) does not represent any correction to the original strain energy function of eq. (4.1). This means that in this case the pressure information $\bar{p}$ is reliable. In all other cases eq. (4.2) represents a correction of the wrongly estimated pressure $\bar{p}$ towards the separately interpolated pressure $\tilde{p}$. For details regarding the derivation of the potential used in eq. (4.2) we refer to the work of Sussman and Bathe (Sussman, 1987). The corrected second Piola-Kirchhoff stresses $\widehat{S}_{ij}$ in the element then follow from eq. (4.2)

$$\widehat{S}_{ij} = \frac{\partial W}{\partial E_{ij}} = \frac{\partial \hat{W}(J_1, J_2)}{\partial E_{ij}} - \tilde{p} J_3 C_{ij}^{-1} . \tag{4.4}$$

These corrected stresses are used to calculate the nodal forces in the elements.

4.2 Derivation of the finite element equations

For the derivation of the finite element equations the principle of virtual work is used

$$\delta\Big(\int_V W dV\Big) = r ,$$

where r is the virtual work of all external forces and W is the strain energy function presented above. The volume integration is performed over the volume V of the undeformed reference configuration. This approach is known as *total Lagrangian formulation*. Since in addition to the element displacements (related to the strain in the material by eq. (3.4)) also the separately interpolated pressure $\tilde{p}$ represents a degree of freedom, the virtual work is

$$\int_V \Big(\frac{\partial W}{\partial E_{ij}} \delta E_{ij} + \frac{\partial W}{\partial \tilde{p}} \delta\tilde{p}\Big) dV = r . \tag{4.5}$$

In the following derivation we have to take into account that the pressure and displacement variation are independent of each other. The finite element discretization for the displacements u_i and the separately interpolated pressure $\tilde{p}$ is introduced

$$u_i = h_I u_i^I , \quad \delta u_i = h_I \delta u_i^I , \quad du_i = h_I du_i^I , \tag{4.6}$$

$$\tilde{p} = h_K \tilde{p}^K , \quad \delta\tilde{p} = h_K \delta\tilde{p}^K , \quad d\tilde{p} = h_K d\tilde{p}^K . \tag{4.7}$$

The upper index I of u_i^I (δu_i^I, du_i^I) denotes the nodal value of the displacement u_i at the I-th node in the element, whereas the upper index K of $\tilde{p}^K$ ($\delta\tilde{p}^K$, $d\tilde{p}^K$) denotes the pressure value taken at the pressure node with index K. Pressure nodes and displacement nodes are usually not at the same

location within the element and consequently also different shape functions h_I and h_K for the displacement and pressure interpolation, respectively, are used. The variation δE_{ij} with respect to the Green-Lagrange strain tensor in eq. (4.5) is substituted by the corresponding variations δu_l with respect to the displacements. The discretized and linearized principle of virtual work can be written with the following two equations

$$\int_V \left(\frac{\partial S_{ij}}{\partial E_{rs}} + \frac{\partial^2 Q}{\partial E_{rs} \partial E_{ij}} \right) \frac{\partial E_{rs}}{\partial u_k} \frac{\partial E_{ij}}{\partial u_l} du_k \delta u_l + \left(S_{ij} + \frac{\partial Q}{\partial E_{ij}} \right) \frac{\partial^2 E_{ij}}{\partial u_k \partial u_l} du_k \delta u_l + \frac{\partial^2 Q}{\partial E_{ij} \partial \tilde{p}} \frac{\partial E_{ij}}{\partial u_l} \frac{\partial \tilde{p}}{\partial \tilde{p}^M} d\tilde{p}^M \delta u_l \Big) dV$$

$$= \int_V {}^B f_l \delta u_l dV + \int_S {}^S f_l \delta u_l dS - \int_V \left(S_{ij} + \frac{\partial Q}{\partial E_{ij}} \right) \frac{\partial E_{ij}}{\partial u_l} \delta u_l dV , \tag{4.8}$$

$$\int_V \left(\frac{\partial^2 Q}{\partial E_{rs} \partial \tilde{p}} \frac{\partial E_{rs}}{\partial u_k} \frac{\partial \tilde{p}}{\partial \tilde{p}^N} du_k \delta \tilde{p}^N + \frac{\partial^2 Q}{\partial \tilde{p}^2} \frac{\partial \tilde{p}}{\partial \tilde{p}^N} \frac{\partial \tilde{p}}{\partial \tilde{p}^M} d\tilde{p}^M \delta \tilde{p}^N \right) dV = - \int_V \left(\frac{\partial Q}{\partial \tilde{p}} \frac{\partial \tilde{p}}{\partial \tilde{p}^N} \delta \tilde{p}^N \right) dV . \tag{4.9}$$

In eq. (4.9) the external virtual work r is set equal to the sum of the virtual work of the external surface forces ${}^S f$ and the external body forces ${}^B f$

$$r = \int_V {}^B f_l \delta u_l dV + \int_S {}^S f_l \delta u_l dS . \tag{4.10}$$

In eq. (4.10), according to d'Alemberts principle, inertia forces for dynamic analysis may be included. The external forces are assumed to be independent of the deformation (although, surface loads are deformation dependent). Including deformation dependent external loads leads to skewsymmetric matrices in the linearized element equations. The last expression on the right-hand side of eq. (4.8) represents the internal nodal element forces. This term is obtained by linearizing the principal of virtual work and represents the point at which the linearization is performed. As can be seen from eq. (4.8) the term of the internal nodal element forces does not depend on the increment du_k in the nodal displacements and is therefore taken on the right-hand side.

The volume integration in eqs. (4.8) and (4.9) is performed numerically by *Gauss quadrature*. In the case of our 4-node element the integrand is evaluated at four defined positions within the element. The weighted sum of the four values then represents the value of the volume integral.

Due to the symmetry of the elasticity tensor $C_{ijrs} = \partial S_{ij} / \partial E_{rs}$ and the Green-Lagrange strain tensor $\boldsymbol{E}$ eq. (4.9) can be written in matrix form

$$\begin{bmatrix} {}^{uu}\boldsymbol{K} & {}^{up}\boldsymbol{K} \\ {}^{up}\boldsymbol{K}^T & {}^{pp}\boldsymbol{K} \end{bmatrix} \begin{bmatrix} d\boldsymbol{u} \\ d\tilde{\boldsymbol{p}} \end{bmatrix} = \begin{bmatrix} {}^{ext}\boldsymbol{f} \\ \boldsymbol{0} \end{bmatrix} - \begin{bmatrix} {}^{u}\boldsymbol{f} \\ {}^{p}\boldsymbol{f} \end{bmatrix}, \tag{4.11}$$

with $d\boldsymbol{u}$ and $d\tilde{\boldsymbol{p}}$ representing the increments in the nodal displacements and in the separately interpolated pressure. The vectors $d\boldsymbol{u}$ and $d\tilde{\boldsymbol{p}}$

$$d\boldsymbol{u} = \left[du_1^1 \; du_i^1 \; \ldots \; du_N^1 \; \ldots \; du_N^L \right],$$

$$d\tilde{\boldsymbol{p}} = \left[d\tilde{p}^1 \; d\tilde{p}^2 \; \ldots \; d\tilde{p}^K \right] \tag{4.12}$$

represent the nodal displacement and pressure increments of the element. L denotes the number of nodes per element, N the number of degrees of freedom per node and K the number of pressure nodes in the element. To avoid element locking it is necessary that the number of displacement degrees of freedom $L \cdot N$ per element is greater or equal than the number of pressure degrees of freedom K per element (Zienkiewicz, 1994, pp. 337)

$$L \cdot N \geq K. \tag{4.13}$$

The element matrices corresponding to eq. (4.11) can be found in Appendix B.

4.3 Explicit integration of the finite element equations

The integration methods for finite element equations may be separated in implicit methods and explicit integration methods. In implicit methods the solution at time $t + \Delta t$ is based on the equilibrium conditions at time $t + \Delta t$ whereas explicit integration schemes base the solution at time $t + \Delta t$ on the equilibrium conditions at time t. A simple forward calculation is usually possible with explicit integration methods. Implicit integration schemes are unconditionally stable whereas explicit integration schemes are subject to mostly strict stability conditions. However, accuracy requirements also limit the time step in implicit integration schemes. In our case we integrate the system of non-linear finite element equations with an explicit integration algorithm. The reasons that led to this choice are explained at the end

of Chapter 4.

The non-linear system of equations is the following

$$\boldsymbol{M}\ddot{\boldsymbol{u}}^{(t)} + \boldsymbol{C}\dot{\boldsymbol{u}}^{(t)} = {}^{ext}\boldsymbol{f}^{(t)} - {}^{int}\boldsymbol{f}^{(t)} . \tag{4.14}$$

$\ddot{\boldsymbol{u}}^{(t)}$ and $\dot{\boldsymbol{u}}^{(t)}$ are the acceleration and the velocity at time t, $\boldsymbol{M}$ is the mass matrix of the system, $\boldsymbol{C}$ the damping matrix, ${}^{ext}\boldsymbol{f}^{(t)}$ are the externally applied forces or the equivalent nodal forces in the case of distributed surface loads, and ${}^{int}\boldsymbol{f}^{(t)}$ are the internal nodal element forces at time t. The internal nodal element forces result from eq. (4.11) by statically condensing out the incremental pressure vector $d\tilde{\boldsymbol{p}}$. The pressure variables $\tilde{\boldsymbol{p}}$ have to be updated with the corresponding increments $d\tilde{\boldsymbol{p}}$ before the algorithm can proceed to the next time step.

The central difference approximation for the acceleration $\ddot{\boldsymbol{u}}^{(t)}$ and the velocity $\dot{\boldsymbol{u}}^{(t)}$ at time t are

$$\dot{\boldsymbol{u}} = \frac{\boldsymbol{u}^{(t+\Delta t)} - \boldsymbol{u}^{(t-\Delta t)}}{2\Delta t} ,$$

$$\ddot{\boldsymbol{u}} = \frac{\boldsymbol{u}^{(t+\Delta t)} - 2\boldsymbol{u}^{(t)} + \boldsymbol{u}^{(t-\Delta t)}}{\Delta t^2} . \tag{4.15}$$

Using eq. (4.15) in eq. (4.14) and solving for $\boldsymbol{u}^{(t+\Delta t)}$ yields

$$\boldsymbol{u}^{(t+\Delta t)} = \frac{\boldsymbol{M}^{-1}}{\left(\frac{1}{\Delta t^2} + \frac{\xi}{\Delta t^2}\right)} \left({}^{ext}\boldsymbol{f}^{(t)} - {}^{int}\boldsymbol{f}^{(t)} + \boldsymbol{u}^{(t)}\boldsymbol{M}\frac{2}{\Delta t^2} - \boldsymbol{u}^{(t-\Delta t)}\boldsymbol{M}\left(\frac{1}{\Delta t^2} - \frac{\xi}{\Delta t^2}\right)\right) , \tag{4.16}$$

where the damping matrix is assumed to be proportional to the mass matrix

$$\Delta t\boldsymbol{C} = 2\xi\boldsymbol{M} . \tag{4.17}$$

In the total Lagrangian formulation the mass matrix $\boldsymbol{M}$ is constant. In a lumping process the mass matrix $\boldsymbol{M}$ is diagonalized and its inverse is computed in advance. Since no stiffness matrix has to be assembled in eq. (4.16) the central difference method represents a very efficient method of integration. To proceed to the next time step only the internal nodal element forces ${}^{int}\boldsymbol{f}^{(t)}$ have to be computed. The conditional stability of the algorithm represents one of the major drawbacks of the explicit finite dif-

ference method. The time step Δt is subject to the *Courant-Friedrich-Lewy condition* for stability

$$\Delta t \leq \Delta t_{crit}. \tag{4.18}$$

A simple approximation of the critical time step Δt_{crit} is given by

$$\Delta t_{crit} \approx \frac{L_{min}}{c_p}, \tag{4.19}$$

where L_{min} is the minimal characteristic length of all finite elements in the mesh and c_p is the propagation speed of *p-waves* in the nearly incompressible material

$$c_p = \sqrt{\frac{E^e}{\rho}} \sqrt{\frac{1-\nu}{(1+\nu)(1-2\nu)}} \approx \sqrt{\frac{\kappa}{\rho}}, \tag{4.20}$$

where the above approximation is valid for $\nu \to 0.5$. From eq. (4.20) and eq. (4.19) follows that for totally incompressible materials ($\kappa \to \infty$) the time step Δt is equal to zero. In this special case an integration of the finite element equations with the central difference method is no longer possible.

In the implicit integration of the finite element equations, with a Newton-Raphson scheme e.g., an equilibrium iteration is performed at every load step to find the newly converged solution. This has the effect that any peak values of the separately interpolated pressure $\tilde{p}$ occurring at the beginning of a new load step are smoothed out with the iteration. In the explicit integration scheme no iteration is performed and thus the separately interpolated pressure $\tilde{p}$ is generally subject to strong oscillations. Since the synthetic material used in Chapter 6 and especially most biological tissues are very soft and nearly incompressible the internal nodal element forces are dominated by the contribution resulting from the pressure $\tilde{p}$. A strongly oscillating pressure $\tilde{p}$ thus produces strongly oscillating internal nodal element forces. Even if the simulation remains stable the oscillating contact forces, which are calculated from the internal nodal element forces, do not allow a reasonable simulation of contact conditions, especially in the presence of friction (see also section 4.6). In the following we are going to show how these oscillations can be smoothed by introducing artificial material damping in the corresponding frequency ranges.

For clarity we recall eq. (3.52) from section 3.5

$$S(x, t+\Delta t) = S^e(C(x, t+\Delta t)) + \int_0^{t+\Delta t} \left(\sum_{i=0}^{N_d} c_i e^{-(t+\Delta t-s)/\tau_i} \right) \frac{\partial}{\partial s} S'(C(x, s)) ds \quad .$$

The above equation shows that the element stresses depend on a purely elastic part including the separately interpolated pressure $\tilde{p}$, which is represented by the first term of the right-hand side, and a history incorporating part depending on the stresses $S'(C(x, s))$ only, represented by the second term of the right-hand side of the above equation. This is the formulation how it is usually found in the literature and which is well suited for implicit finite element algorithms. In the case of the explicit integration the above formulation has to be modified in order to better damp the oscillations of the separately interpolated pressure $\tilde{p}$ and of the element displacements occurring at high frequencies by introducing artificial material damping in the corresponding frequency ranges. The following formulation proved to be very efficient in damping these strong oscillations

$$\begin{aligned} S(x, t+\Delta t) = {} & S^e(C(x, t+\Delta t)) + \int_0^{t+\Delta t} \left(\sum_{i=0}^{N_d} c_i e^{-(t+\Delta t-s)/\tau_i} \right) \frac{\partial}{\partial s} S'(C(x, s)) ds \\ & - \int_0^{t+\Delta t} \left(c^p \sum_{i=0}^{1} e^{-(t+\Delta t-s)/\tau_i^p} \right) \frac{\partial}{\partial s} (\tilde{p}(x, s) J_3(s) C^{-1}(x, s)) ds \\ & + \int_0^{t+\Delta t} \left(c^u \sum_{i=0}^{3} e^{-(t+\Delta t-s)/\tau_i^u} \right) \frac{\partial}{\partial s} S'(C(x, s)) ds \quad , \end{aligned} \tag{4.21}$$

where c^p is the constant weighting factor and τ_i^p are the relaxation times of the reduced exponential relaxation functions used to damp the pressure oscillations and c^u and τ_i^u are the counterparts of the reduced exponential relaxation functions used to damp the displacement oscillations. The third and fourth term of the right hand side in eq. (4.21) were introduced to damp the separately interpolated pressure $\tilde{p}$ and oscillations in the element displacements occurring at high frequencies. Since the third and fourth term of the right hand side in eq. (4.21) have no other reason than to damp element oscillations they were separated from the first two terms which represent material properties relevant for the simulation of the aspiration experiment. The third term in eq. (4.21) can be easily explained by recalling eq. (4.4); the pressure $\tilde{p}$ is included in the history dependence of the stresses and not treated as purely elastic. The fourth term in eq. (4.21) is

analogous to the second term except that it influences a frequency range relevant only for the element oscillations and not for the material behaviour in the simulation of the aspiration experiment.

The new constants introduced in eq. (4.21) were set to the following values which proved to be optimal regarding the suppression of the nodal element force oscillations: $c^p = 0.3$ [-], $\tau_0^p = 0.2\Delta t$ [s], $\tau_1^p = 2.0\Delta t$ [s], $c^u = 3.0$ [-], $\tau_0^u = 10^{-5}[s]$, $\tau_1^u = 10^{-4}[s]$, $\tau_2^u = 10^{-3}[s]$ and $\tau_3^u = 10^{-2}[s]$, where Δt is the time step of the explicit integration scheme. As can be seen from the above constants the relaxation times τ_i^p used to damp the pressure oscillations vary with the time step Δt. This is a heuristic approach which is due to the observation that the pressure oscillations occur with a period proportional to the time step Δt. Here, the question arises how large the value of the largest of the above time constants can be set without altering the material model properties with respect to its application in the simulation of the aspiration experiment. As shown later in Section 5.2 the largest of the above relaxation times $\tau_3^u = 10^{-2}[s]$ used for the displacement oscillation damping does not substantially influence the simulation of the aspiration experiment since the smallest material relaxation time having a discernible influence on an experiment with dynamics similar to the one of a typical aspiration experiment lies in the vicinity of $\tau \approx 0.1[s]$.

The above damping formulation with a whole spectrum of material relaxation times introduced for numerical stability allows to set the value of the numerical damping constant ξ in eq. (4.16) equal to zero, $\xi \equiv 0$. In Fig. 4.1 a comparison of a simulation performed with numerical damping and with material damping only ($\xi \equiv 0$) is shown. The index on the abscissa is proportional to the time in the simulation. Both simulations were performed once with the separately interpolated pressure $\tilde{p}$ not damped ($c^p = 0$) and once with damped pressure $\tilde{p}$. Fig. 4.1 shows the normal contact force of a single node being in contact with the base of the aspiration tube. The normal contact force is plotted over the index which is proportional to the time. As the contact forces have shown to be very sensitive to element oscillations they are a good measure for the quality of the simulation. As Fig. 4.1 shows a relevant improvement of the quality of the simulation is only possible by damping the pressure $\tilde{p}$ (the simulations in Fig. 4.1 were all performed with the following friction parameters $\mu_R = 0.2$ and $u_{tol} = 10^{-6}[m]$, compare Section 4.6). Without pressure damping strong oscillations are observed in the nodal element forces with both formulations. Especially in contact simulations including friction strong contact force oscillations are undesirable. The difference between the two damp-

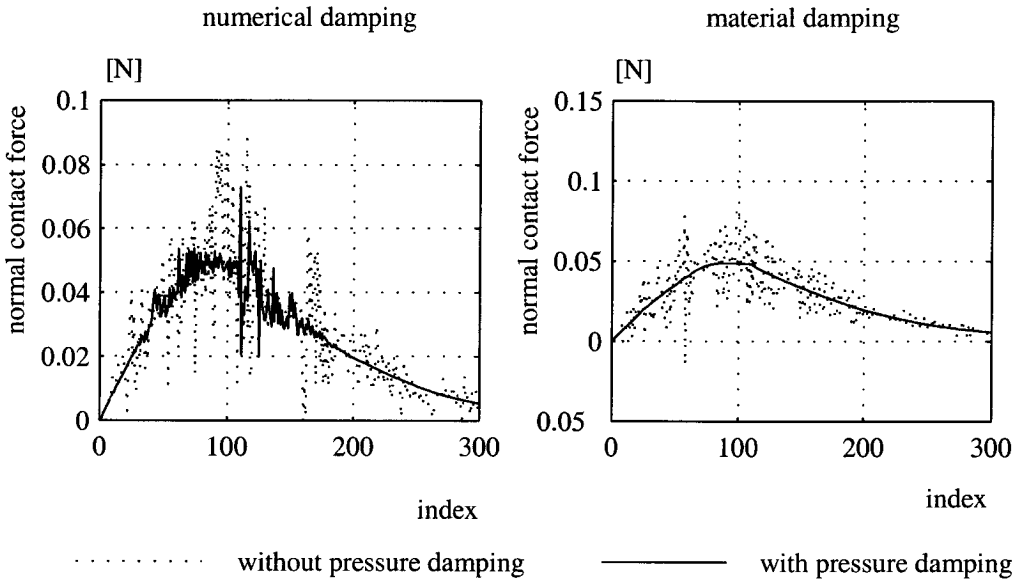

Fig. 4.1 Comparison of numerical and material damping

ing formulations in the simulated displacements of the whole aspirated surface is negligible.

The great advantage of the damping formulation with a discrete spectrum of relaxation times in contrast to a mass proportional damping is that a wide spectrum of frequencies can be damped. The most important advantage of the "material damping method" is that we are able to know which frequencies are influenced and thus the influence of the damping which is introduced only for numerical stability can be separated from the real material damping.

4.4 Contact

In our model only rigid-deformable contact is treated. Since the aspiration tube is much stiffer than the aspirated tissue treating the tube as a rigid body is a good approximation of the encountered situation. Treating rigid-deformable contact poses much less difficulties than treating deformable-deformable contact, at least with the explicit time integration algorithm.

A first step in modelling contact is a systematic definition of the contact geometry. Since only two-dimensional contact is modelled, lines and circular arcs with a maximum aperture angle of 45° are used to define the rigid contact geometry. Both used curve elements have a starting point and

an end point which then also define an outward normal (see Fig. 4.2). A potential contact zone is defined in order to speed up the contact searching algorithm. At the beginning of each simulation all potential contact nodes of the finite element model are established. In the model used for the simulation of the aspiration experiment all nodes lying on the topmost surface in the vicinity of the geometry defining the base of the aspiration tube are potential contact nodes. During the simulation only the potential contact nodes are checked against all curve elements, which define the contact geometry. The outward normal for a potential contact node, defining

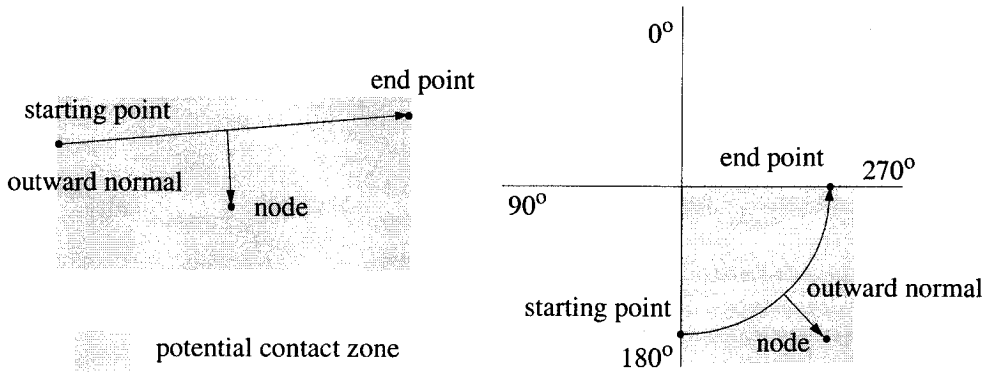

Fig. 4.2 Definition of contact geometry

whether a node lies inside or outside the contact geometry, is only calculated if the node is inside the potential contact zone of the respective curve element. This saves computational effort in the explicit formulation since the time step is very small and the contact conditions need to be checked at every time step.

Treatment of rigid-deformable contact with the explicit integration scheme is very simple. Before the nodal positions are updated in each time step the contact conditions are checked with the calculated displacement increments for all potential contact nodes. These displacement increments are calculated without any restrictions resulting from the contact geometry. If a node is about to penetrate the contact geometry the nodal displacement is corrected so that the node lies on the rigid bounding surface again. The correction of the displacement increment of the penetrating nodes is done perpendicular to the curve defining the rigid surface. This method is very simple and efficient and can be compared to a *penalty method.*

In the penalty method the contact conditions are enforced by applying forces proportional to the penetration depth of the respective node. The

proportionality factor is called penalty factor and the applied forces are the penalty forces. Large penalty factors, which enforce the contact conditions to be met more precisely, usually tend to destabilize the finite element simulation.

4.5 Accelerating the simulation by artificially increasing the density of the simulated material

In contact simulations it is of great importance to refine the finite element mesh in the contact zone with other contact bodies, especially in the tissue aspiration experiment where contact of the aspirated tissue with the small radius of the rigid base of the aspiration tube occurs. The strongly varying stresses around the contact zone can only be resolved with a fine mesh. Additionally, in the contact algorithm only the element nodes and not the element sides are tested for contact. If typical proportions of the contact geometry are similar to the smallest element lengths in the contact zone the contact geometry can penetrate the mesh without coming into contact with one of the nodes. The smallest radius of the rigid contact geometry is $r = 0.25$ [mm] (see Fig. 4.3). Since the time step in an explicit

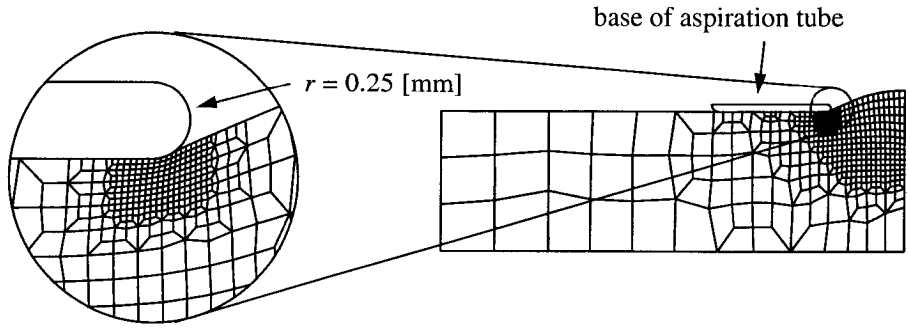

Fig. 4.3 Detail of finite element mesh

integration scheme is, apart from the bulk modulus of the material, determined by the smallest element in the mesh, the computational effort increases rapidly with decreasing element size. In the mesh shown in Fig. 4.3 the size of the smallest element is about $L_{min} = 4 \cdot 10^{-5}$ [m]. A bulk modulus of 10^7[N/m^2] and a density of $\rho = 10^3$ [kg/m^3] yield with eqs. (4.19) and (4.20) a critical time step of $\Delta t_{crit} \approx 4 \cdot 10^{-7}$[s]. This time step is much too small to allow a simulation of the aspiration experiment with reasonable computational effort. Especially when the simulations are employed in an inverse finite element algorithm with a frequent recomputation of the

model the computational effort has to be reduced drastically.

Since the aspiration experiment is a slow process it can be treated as *quasi-static*. In a quasi-static process the potential energy stored in the deformation of the material is much larger than the kinetic energy resulting from the material velocity. In this case the density of the simulated material might be artificially increased without relevantly changing the kinetic energy of the system. On the other hand Fig. 4.3 shows that additionally a varying mass distribution within the mesh can be used. The smallest elements in the mesh are subject to small accelerations both in the direction tangential and normal to the base of the aspiration tube. By artificially increasing the mass density in this critical zone the time step can be increased without altering the dynamics of the system. The elements at the centre of the axisymmetric model are the most important ones regarding the dynamics of the system. Therefore, these elements are weighted with a material density corresponding to the real material density ρ_{real}. The elements at the centre then also determine the critical time step Δt_{crit} through eqs. (4.19) and (4.20) where the minimal element length L_{min} of the mesh is replaced by a typical element length L_{typ} of one of the elements in this central zone of the mesh. The mass density ρ_{elem} of all other elements of the mesh is then scaled in order to give the same critical time step as given by the typical element of the central zone of the mesh. Thus the density in each element ρ_{elem} scales in the following way

$$\begin{cases} \rho_{elem} = \left(\dfrac{L_{typ}}{L_{min}^{elem}} \right)^2 \rho_{real} & \text{for} \quad L_{min}^{elem} \le L_{typ} \\ \rho_{elem} = \rho_{real} & \text{for} \quad L_{min}^{elem} > L_{typ} \end{cases} \tag{4.22}$$

where ρ_{real} is the real material density and L_{min}^{elem} is the minimum length of the respective element. We see from eq. (4.22) that elements smaller than the typical element are weighted with a density higher than the real material density. With the above approach the time step Δt of the central difference algorithm increases approximately by a factor of 6. This means that the material density ρ_{elem} in the smallest elements is artificially increased by a factor of 36 with respect to the real material density ρ_{real}. If the density increase according to eq. (4.22) is applied the simulation is refered to as accelerated simulation. The increase in the critical time step obtained with an accelerated simulation is still not sufficient for the use of the explicit formulation in an inverse finite element algorithm. To additionally speed

up the simulation the density of all and not only of the smallest elements is increased with increasing material deformation. In the following this material density increase is called global material density increase. The global material density increase is always applied together with the variable material density increase as characterized by eq. (4.22). In the following a simulation with a global material density increase is called a globally accelerated simulation. In Fig. 4.4 the kinetic energy and the potential energy for a non-accelerated, an accelerated and a globally accelerated simulation of a typical aspiration experiment are compared. All quantities

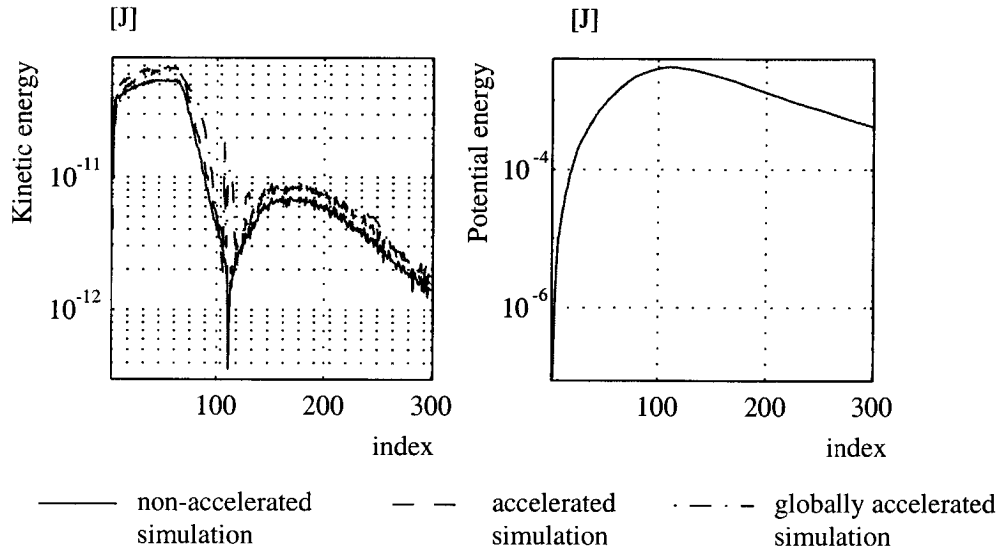

Fig. 4.4 Kinetic and potential energy of the Silgel material (see Chapter 6) in a typical aspiration test. The non-accelerated, the accelerated and the globally accelerated simulation are compared.

are plotted over their column index which is proportional to the running time in the simulation. An unsteady behaviour is observed in the plots of the kinetic energy in the non-accelerated, the accelerated and the globally accelerated simulation. These observed peaks are due to the sensitivity of the kinetic energy to mesh oscillations which are difficult to suppress in this case of very soft but nearly incompressible materials. The kinetic energy in both the accelerated and the globally accelerated simulation nevertheless remains much smaller than the potential energy in the material throughout both simulations. The curves for the potential energy in Fig. 4.4 are identical for all three simulations, i.e. the non-accelerated, the accelerated and the globally accelerated simulation.

The objectivity function (see Chapter 5) in the parameter identification consists of the squared differences between experimental and simulated profile displacements. This makes the axial nodal displacements on the surface of the aspirated material become the quantities with the highest accuracy requirements in the simulation of the experiment. In Fig. 4.5 the axial coordinates of the central node of the aspirated material surface and of a node on the surface close to the aspiration tube are plotted. The curves of the accelerated and the globally accelerated simulation are seen to be identical with the curve of the non-accelerated simulation. The maximum relative error in the calculated nodal axial coordinates between the globally accelerated and the non-accelerated simulation is 0.8%.

The reduced Veronda-Westmann material law (see eq. (3.20)) is more sensitive to an acceleration of the simulation since the material stiffness is very small at small deformations. This means that the kinetic energy of an

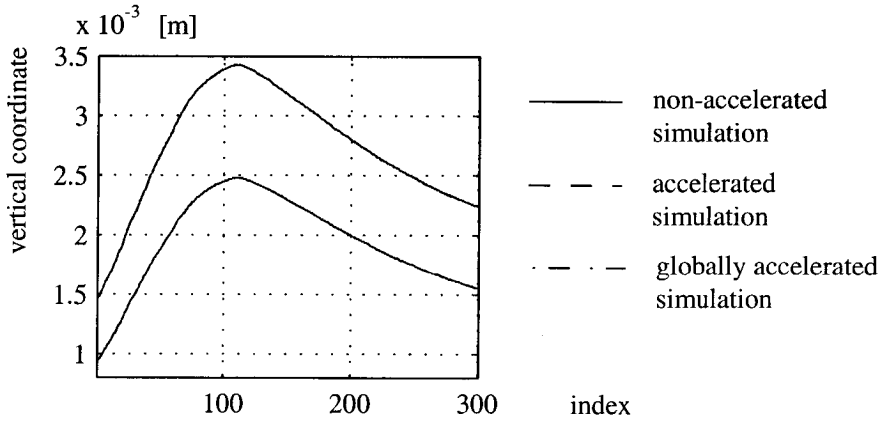

Fig. 4.5 Axial coordinate of the central node (top lines) and of a node close to the base (bottom lines) of the aspiration tube in the non-accelerated, the accelerated and the globally accelerated simulation of a typical aspiration experiment. The material model used is a neo-Hookean formulation.

aspirated material characterized by a reduced Veronda-Westmann material model is less likely to be small as compared to the potential energy at small deformations. For the reduced Veronda-Westmann material law from eq. (3.20) the maximum error in the axial displacements between the globally accelerated and the accelerated simulation is 0.4% (for $\gamma = 6$ [-]). The accelerated simulation proved for the neo-Hookean material model to compute the axial displacement results with a relative error of $4.5\ 10^{-4}$% as compared to the non-accelerated simulation. Due to this very high accu-

racy it seems admissible to use the accelerated simulation as a reference in order to establish the merit of the globally accelerated simulation.

The course of the global material density increase factor used in a typical simulation of an aspiration experiment is plotted in Fig. 4.6. At the beginning of the simulation due to the small potential energy in the material the density is increased only in the smallest elements to obtain a reasonable time step. With increasing deformation the global material density increase factor reaches values up to a maximum of 70 with respect to the real material density of the central elements in the mesh. The material density is then kept constant until the maximum axial surface displacement is reached. At this point the aspiration pressure in the tube is lowered in order to release the material. The aspirated material starts to return to its undeformed configuration. Though the acceleration of the material at this

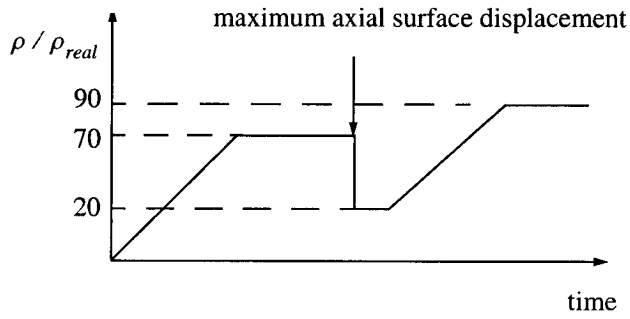

Fig. 4.6 Typical course of the global material density increase factor during the simulation of an aspiration experiment

point is small the global material density increase factor is decreased in order to capture the dynamics of this release process. When the material velocity has become small enough the global density increase factor is again slowly increased up to a maximum value of 90 for the rest of the simulation. With the above presented acceleration scheme the computational time is reduced to approximately 20 minutes for the simulation of an aspiration experiment lasting 20 seconds.

4.6 Friction

Friction plays an important role in many mechanical simulations where contact of bodies occurs. The classical model used to describe friction is *Coulomb's law*. Coulomb's law accounts for sticking and gliding (see Fig. 4.7), where the friction coefficient for gliding is smaller than the one

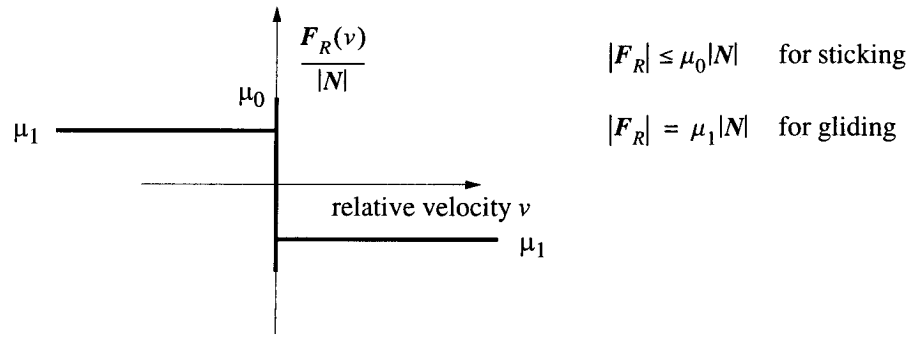

Fig. 4.7 Coulomb's law of friction

for sticking. Coulomb's law is not suited for finite element simulations since its non-linearity may lead to high artificial element stresses and thus to bad convergence behaviour due to oscillating normal contact forces. In an implicit integration scheme, as e.g. in the Newton-Raphson iteration, the tangential stiffness matrix with respect to the nodal degrees of freedom is formed. As Fig. 4.7 shows, Coulomb's law is not differentiable. Differentiability can be regained by approximating Coulomb's law from Fig. 4.7 with differentiable functions. Frictional contact leads to non-symmetric coefficient matrices if a consistent linearization procedure is applied. This prevents the use of efficient solvers for positive definite systems.

In our contact formulation a friction model corresponding to Fig. 4.8 is used. A node coming into contact with a rigid surface is subject to a force F_R pulling it back to the point of initial contact.

This force F_R scales linearly with increasing distance Δu_{rel} from the point of initial contact and is therefore comparable to a linear spring element. The spring stiffness does not only depend on the elongation Δu_{rel}

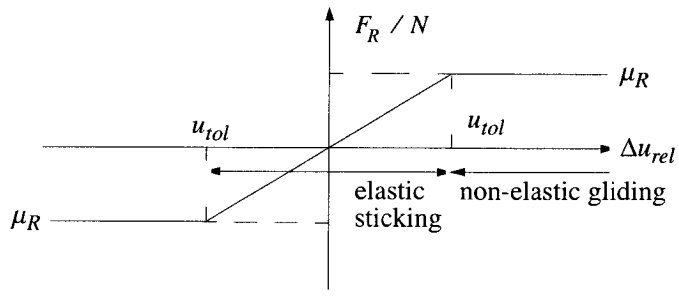

Fig. 4.8 Model for friction

but also on the normal contact force N and on the friction coefficient μ_R

$$F_R = -\frac{|\Delta u_{rel}|}{u_{tol}} \frac{\Delta u_{rel}}{|\Delta u_{rel}|} \mu_R N = -\frac{\Delta u_{rel}}{u_{tol}} \mu_R N \quad \text{for} \quad \Delta u_{rel} \le u_{tol} . \tag{4.23}$$

A node moving outside the region characterized by the factor u_{tol} experiences a force F_R not depending on the value of Δu_{rel} but only on its direction

$$F_R = -\frac{\Delta u_{rel}}{|\Delta u_{rel}|} \mu_R N \quad \text{for} \quad \Delta u_{rel} > u_{tol} . \tag{4.24}$$

A node changing the direction of relative movement and currently experiencing non-elastic gliding first returns into elastic sticking at the new nodal position and then possibly starts gliding again. This friction model is based on relative nodal displacements and not on relative velocities. In the simulations the nodal displacements proved to behave much more continuous than the nodal velocities. The incorporation of friction in the finite element model in general tends to destabilize the simulation, especially if large friction coefficients μ_R are considered. With large friction coefficients *stick-slip* effects can be observed at the contact nodes. As a consequence of these stick-slip effects strongly oscillating contact forces are observed. As an example in Fig. 4.9 the simulated deformed profiles for

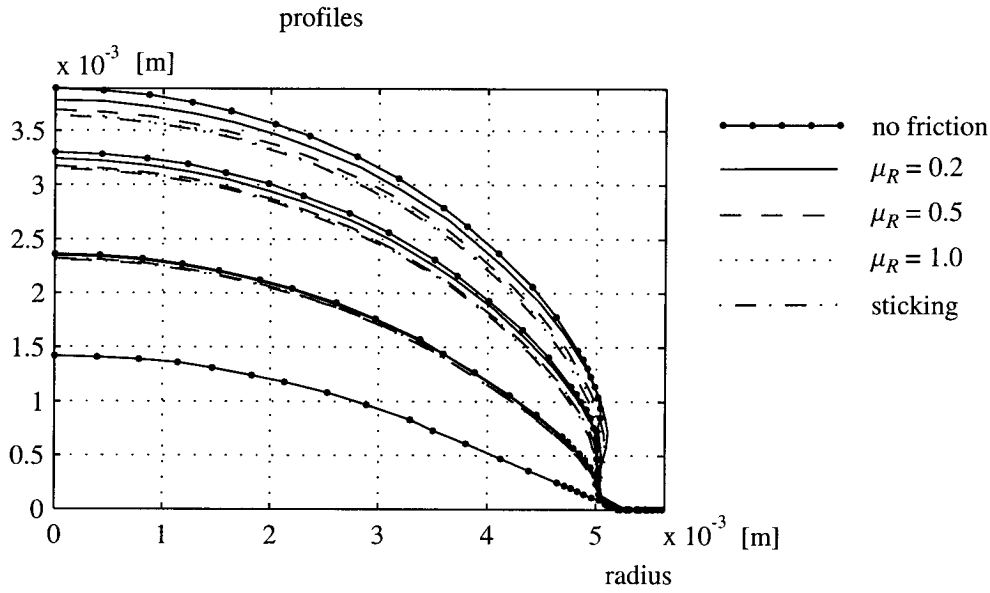

Fig. 4.9 Simulated deformed profiles of Silgel612 for different friction coefficients (corresponding to four aspiration pressure values)

the synthetic material Silgel612 for different friction coefficients μ_R are shown. This synthetic material was used in the experimental verification of the inverse material parameter estimation in Chapter 6. The different multiple profiles in Fig. 4.9 correspond to different aspiration pressure values, whereas the different line types designate the different frictional conditions applied in the simulation. The maximum applied aspiration pressure in Fig. 4.9 is 120 [mbar].

It might seem possible to obtain information about the frictional contact conditions from the shape of the deformed aspirated surface. But, as Fig. 4.9 shows, no relevant change in the shape of the deformed aspirated surface can be observed for different frictional conditions. The largest change in the surface profile shape due to different friction conditions occurs in the region next to the edge of the aspiration tube. Apart from the changing axial displacement of the aspirated profile hardly any change in shape of the central part of the profile is noticed due to the different frictional contact conditions. Considering the fact that the contour extraction algorithm for the profile determination does not yield reliable profile data in the surface region close to the edge of the aspiration tube (due to the special illumination conditions in the aspiration tube) an estimation of the friction coefficient μ_R is not possible in the inverse parameter estimation with the actual experimental configuration. In the inverse parameter estimation the changing axial displacement of the aspirated surface due to different frictional contact conditions results in an estimated material stiffness different from its real value if the contact conditions are not modelled properly. Therefore it turns out to be very important to have well defined contact conditions at the contact surface of the aspirated material with the aspiration tube.

4.7 Explicit versus implicit formulation

For quasi-static problems the implicit finite element formulation is in general numerically more efficient than the explicit finite element formulation.

The simulated aspiration experiments showed large material deformation around the corner of the base of the aspiration tube with strong element distortions. With the also tested implicit finite element formulation no converging results were obtained for this situation. Another advantage of the explicit formulation compared with the implicit code is also the simplicity in the treatment of contact conditions. In implicit finite element codes the

treatment of contact represents a challenging task, especially if also friction has to be considered. Friction is implemented very naturally in explicit codes and the small time steps additionally ensure that the evolution of the friction forces in the simulated process is accounted for very accurately. Material laws are easily implemented in explicit codes whereas in implicit codes the tangential material stiffness is required, which represents a far more difficult task. If viscoelastic materials with a spectrum of different relaxation times are modelled the smallest of the relaxation times determines the maximum time step for the implicit finite element code. In the explicit formulation, especially when nearly incompressible materials are modelled, the time step Δt is usually much smaller than the smallest relaxation time in the material model. In the material models used in this thesis the smallest relaxation time is approximately $\tau \approx 0.1$ [s]. In view of this small value a time step of $\Delta t \approx 0.01$ [s] is needed in the implicit formulation in order to accurately integrate the history dependence of the stresses. This small time step in the implicit formulation does not admit large time (or load) increments. The relatively large admissible time steps or load increments, one of the greatest advantages of the implicit over the explicit formulation, can thus not be taken advantage of.

The numerical advantages of the implicit formulation over the explicit formulation are cancelled out to a great extent by the disadvantages mentioned above and especially by the inability to simulate the large deformations observed in the aspiration experiments. Therefore the explicit formulation was chosen for the simulation of the aspiration experiment.

Chapter 5

Inverse Finite Element Algorithm

The *Inverse Finite Element Method* is a numerical approach in which an optimization algorithm is coupled with a finite element method in order to find optimal values for a set of target parameters which enter the finite element simulation. A user defined objective function serves to measure the optimality of the parameters. The finite element method is used to simulate the physical process which depends on the target parameters. The target parameters can be various physical quantities like e.g. the dimensions of a mechanical component in topology optimization or material parameters in inverse material parameter estimation related to experimental testing. In the second case an optimal fit of the simulated data to the experimental data is searched. In classical laboratory setups, like e.g. uniaxial tension experiments, an evaluation of the experimental data is usually possible with simple methods. In the case of the tissue aspiration experiment, the target parameters cannot be determined by solving simple relations between the experimental data and the target parameters. Therefore, the inverse finite element method was chosen to evaluate the tissue aspiration experiments.

Any assumptions included in the finite element model and in the whole simulation of the experiment determine the quality of the inverse solution. The simulation can only represent physical processes accounted for in the mathematical model. Also the experiment has to be performed in a way to reveal information relevant for the estimation of the target parameters in the inverse solution. It is preferable to keep the number of target parameters in the inverse solution as small as possible. Models with a large

number of target parameters tend to produce parameter values that are not reasonable from a physical point of view. The larger the number of target parameters the smaller is usually the influence of any single parameter on the physical response of the studied system and thus also on the objective function. *A priori* knowledge of reasonable parameter values in connection with *regularization techniques* can help to avoid such problems. If regularization is applied to an inverse problem the actual deviation of the parameters from known good values for some or all of the parameters is included in the objective function. Also parameter interdependencies should be avoided in the model as far as possible.

The optimization strategy for the parameter estimation can be a *global* or a *local* method. The global method finds a set of parameter values that corresponds to a global minimum of the objective function, whereas the local method performs locally optimal steps and may lead to only locally optimal parameter values. Optimization theory terms a method as *globally convergent* when the method guarantees a reduction of the objective function in each optimization step. A globally convergent method, however, does not guarantee that the global minimum of the respective function is found.

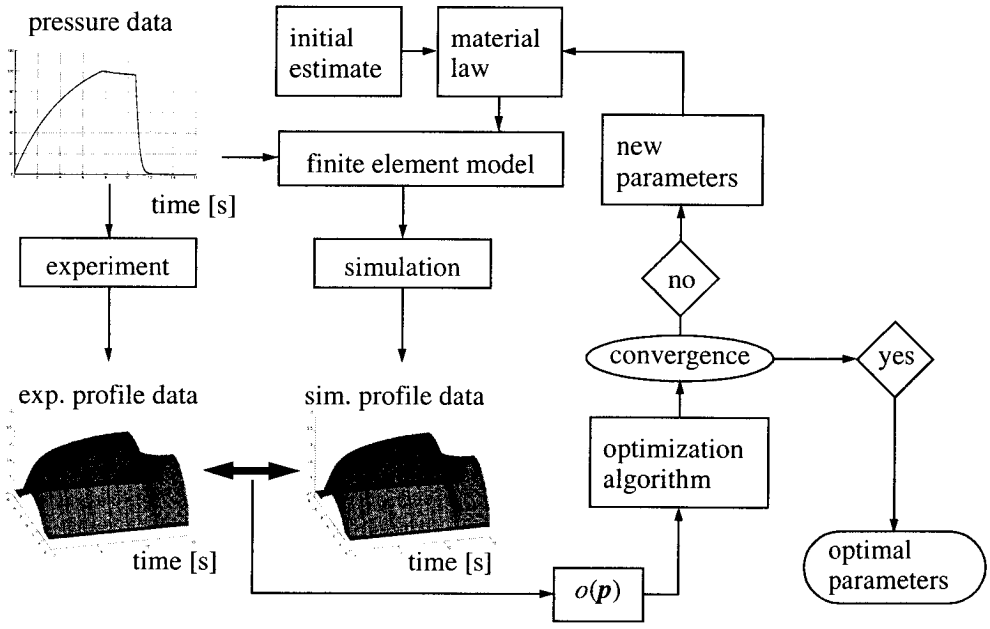

Fig. 5.1 Flow chart for parameter estimation algorithm

For our problem a *Levenberg-Marquardt algorithm* was chosen as opti-

mization strategy. The Levenberg-Marquardt algorithm has already shown to work well in finite strain applications of inverse material parameter estimation (Moulton 1995, Kyriacou 1996), it does however not guarantee that the global minimum of the objective function is found. Methods, like simulated annealing e.g., which are able to find global minima, are in our case computationally too expensive, because they require frequent sampling of the objective function. In our case the evaluation of the objective function requires a complete finite element simulation and thus represents the computationally most expensive part of the optimization.

The flow chart in Fig. 5.1 shows how the objective function is determined by comparing experimental and simulated data. The aspiration pressure applied in the experiment is used in the finite element simulation as boundary condition on the surface of the tissue. Then, the calculated and the experimentally determined tissue surface displacements are compared. This comparison determines the value of the objective function $o(\boldsymbol{p})$ for the actual set of the target parameters $\boldsymbol{p}$ at the respective iteration step. The target parameter vector $\boldsymbol{p}$ is adapted until an optimal match between the experimental and the simulated profile data is obtained. The elements p_i of the parameter vector $\boldsymbol{p}$ are normalized. The objective function $o(\boldsymbol{p})$ is equal to the sum of the squared elements of the residual vector $\boldsymbol{r}$

$$o(\boldsymbol{p}) = \frac{1}{2}\sum_{i=1}^{m} r_i(\boldsymbol{p})^2 = \frac{1}{2}\boldsymbol{r}(\boldsymbol{p})^T\boldsymbol{r}(\boldsymbol{p}), \tag{5.1}$$

where $m = n \cdot k$ (n is the number of radial profile sampling points and k is the number of profiles). In our case the residual vector is defined to be

$$r_i(\boldsymbol{p}) = [z_{sim}(rad_j, t_l, \boldsymbol{p}) - z_{exp}(rad_j, t_l)]\big|_{i=(l-1)\,n+j}, \tag{5.2}$$

where $z_{sim}(rad_j, t_l, \boldsymbol{p})$ is simulated data and $z_{exp}(rad_j, t_l)$ is measured data from one aspiration experiment. The experimental data is obtained by sampling the profile of the aspirated tissue at the radial positions with radii $rad = rad_1 \ldots rad_n$ at the discrete times $t = t_1 \ldots t_k$ whereas the simulated data is obtained by sampling the finite element data at the same radii and at the same times as in the experiment.

In our work the IMSL routine "imsl_d_nonlin_least_squares", which represents a Levenberg-Marquardt algorithm, was used to perform the optimization. In the following a short outline of the theory leading to the employed Levenberg-Marquardt algorithm is given.

5.1 Restricted step methods and trust region approach

The later presented Levenberg-Marquardt algorithm belongs to the restricted step methods (Fletcher, 1987). It is based on a quadratic function $\tilde{o}(\boldsymbol{p})$ which represents an approximation of the underlying objective function $o(\boldsymbol{p})$. The objective function in general is a non-linear function of the target parameters which are summarized in the vector $\boldsymbol{p}$. The Levenberg-Marquardt algorithm finds the optimal parameter vector $\boldsymbol{p}$ iteratively, therefore the iteration counter (k) is introduced. In the (k)-th iteration step a correction $\Delta\boldsymbol{p}^{(k)}$ to the actual parameter vector $\boldsymbol{p}^{(k)}$ is calculated. The quadratic model $\tilde{o}(\boldsymbol{p}^{(k)})$ of the objective function $o(\boldsymbol{p})$ is obtained from a *truncated Taylor series expansion* of the objective function $o(\boldsymbol{p}^{(k)})$

$$o(\boldsymbol{p}^{(k)} + \Delta\boldsymbol{p}^{(k)}) \approx \tilde{o}(\boldsymbol{p}^{(k)} + \Delta\boldsymbol{p}^{(k)}),$$

where

$$\tilde{o}(\boldsymbol{p}^{(k)} + \Delta\boldsymbol{p}^{(k)}) = o(\boldsymbol{p}^{(k)}) + \Delta\boldsymbol{p}^{(k)T}\nabla o(\boldsymbol{p}^{(k)}) + \frac{1}{2}\Delta\boldsymbol{p}^{(k)T}[\nabla^2 o(\boldsymbol{p}^{(k)})]\Delta\boldsymbol{p}^{(k)}. \tag{5.3}$$

This approach requires zero, first and second order derivatives of $o(\boldsymbol{p}^{(k)})$ to be available at the point $\boldsymbol{p}^{(k)}$. The quadratic model $\tilde{o}(\boldsymbol{p}^{(k)} + \Delta\boldsymbol{p}^{(k)})$ has a unique minimizer only if $\nabla^2 o(\boldsymbol{p}^{(k)})$ is positive definite. In all other circumstances no unique minimizer exists. Another way of regarding this fact is that the region around $\boldsymbol{p}^{(k)}$ in which the Taylor series is adequate, does not include a minimizing point of $\tilde{o}(\boldsymbol{p}^{(k)} + \Delta\boldsymbol{p}^{(k)})$. A more realistic approach therefore is to assume that some neighbourhood Ω of $\boldsymbol{p}^{(k)}$ is defined in which $\tilde{o}(\boldsymbol{p}^{(k)} + \Delta\boldsymbol{p}^{(k)})$ agrees with $o(\boldsymbol{p}^{(k)} + \Delta\boldsymbol{p}^{(k)})$ in some sense. Then it is appropriate to choose $\Delta\boldsymbol{p}^{(k)}$ in a way to minimize $\tilde{o}(\boldsymbol{p}^{(k)} + \Delta\boldsymbol{p}^{(k)})$ in the neighbourhood Ω of $\boldsymbol{p}^{(k)}$. This approach is often also referred to as the *trust region* approach.

The optimization problem is then formulated for the quadratic model $\tilde{o}(\boldsymbol{p}^{(k)} + \Delta\boldsymbol{p}^{(k)})$ and not for the objective function $o(\boldsymbol{p}^{(k)} + \Delta\boldsymbol{p}^{(k)})$ itself

$$\text{minimize } \tilde{o}(\boldsymbol{p}^{(k)} + \Delta\boldsymbol{p}^{(k)}) \text{ subject to } \|\Delta\boldsymbol{p}^{(k)}\| \leq h^{(k)}. \tag{5.4}$$

Here arises the problem of how to choose the radius $h^{(k)}$ of the neighbourhood Ω. To prevent undue restriction of the step $\Delta\boldsymbol{p}^{(k)}$, $h^{(k)}$ should be as

large as possible. On the other hand $h^{(k)}$ is subject to a certain measure of agreement existing between $o(\boldsymbol{p}^{(k)}+\Delta\boldsymbol{p}^{(k)})$ and $\tilde{o}(\boldsymbol{p}^{(k)}+\Delta\boldsymbol{p}^{(k)})$. This can be quantified by defining the actual reduction in $o(\boldsymbol{p}^{(k)}+\Delta\boldsymbol{p}^{(k)})$

$$\Delta o^{(k)} = o(\boldsymbol{p}^{(k)}) - o(\boldsymbol{p}^{(k)}+\Delta\boldsymbol{p}^{(k)})$$

and the corresponding reduction as predicted by $\tilde{o}(\boldsymbol{p}^{(k)}+\Delta\boldsymbol{p}^{(k)})$

$$\Delta\tilde{o}^{(k)} = \tilde{o}(\boldsymbol{p}^{(k)}) - \tilde{o}(\boldsymbol{p}^{(k)}+\Delta\boldsymbol{p}^{(k)}) = o(\boldsymbol{p}^{(k)}) - \tilde{o}(\boldsymbol{p}^{(k)}+\Delta\boldsymbol{p}^{(k)}).$$

Then the ratio

$$r^{(k)} = \frac{\Delta o^{(k)}}{\Delta\tilde{o}^{(k)}}$$

measures the quality to which $\tilde{o}(\boldsymbol{p}^{(k)}+\Delta\boldsymbol{p}^{(k)})$ approximates $o(\boldsymbol{p}^{(k)}+\Delta\boldsymbol{p}^{(k)})$ in the k-th iteration step. The closer $r^{(k)}$ is to unity, the better is the approximation. $h^{(k)}$ is changed adaptively from iteration step to iteration step in order to keep a good degree of agreement as measured by $r^{(k)}$.

5.1.1 Levenberg-Marquardt algorithm

The Levenberg-Marquardt algorithm, as already mentioned, belongs to the restricted step methods. The reasons for restricting the optimization step were given in section 5.1.

The optimization problem to solve is formulated in eq. (5.4), where now the norm $\|\ \|$ is defined to be the L_2 norm. Thus the optimization problem can be reformulated as

$$\text{minimize } \tilde{o}(\boldsymbol{p}^{(k)}+\Delta\boldsymbol{p}^{(k)}) \text{ subject to } \Delta\boldsymbol{p}^{(k)T}\Delta\boldsymbol{p}^{(k)} \le h^{(k)2}. \qquad (5.5)$$

With the *Lagrange multiplier technique* the condition $\Delta\boldsymbol{p}^{(k)T}\Delta\boldsymbol{p}^{(k)} \le h^{(k)2}$ can be added to the function $\tilde{o}(\boldsymbol{p}^{(k)}+\Delta\boldsymbol{p}^{(k)})$ to yield the augmented *Lagrange function L*

$$L = \tilde{o}(\boldsymbol{p}^{(k)}+\Delta\boldsymbol{p}^{(k)}) + \lambda^{(k)}\frac{1}{2}(\Delta\boldsymbol{p}^{(k)T}\Delta\boldsymbol{p}^{(k)} - h^{(k)2}), \qquad (5.6)$$

where the *Lagrange multiplier* $\lambda^{(k)}$ has been introduced (the factor $1/2$ was introduced for convenience). The optimality condition for the parame-

ter correction $\Delta \boldsymbol{p}^{(k)}$ requires that the variation of the Lagrange function L with respect to $\Delta \boldsymbol{p}^{(k)}$ and with respect to the Lagrange multiplier $\lambda^{(k)}$ be equal to zero (remember that $\boldsymbol{p}^{(k)}$ is kept constant, since it denotes the actual parameter vector, whereas $\Delta \boldsymbol{p}^{(k)}$ denotes the correction to $\boldsymbol{p}^{(k)}$)

$$\delta L = \nabla o(\boldsymbol{p}^{(k)})^T \delta \Delta \boldsymbol{p}^{(k)} + \delta \Delta \boldsymbol{p}^{(k)T} (\nabla^2 o(\boldsymbol{p}^{(k)}) + \lambda^{(k)} \boldsymbol{I}) \Delta \boldsymbol{p}^{(k)}$$

$$+ \frac{1}{2} \delta \lambda^{(k)} (\Delta \boldsymbol{p}^{(k)T} \Delta \boldsymbol{p}^{(k)} - h^{(k)2}) = 0. \tag{5.7}$$

Since the variations $\delta \Delta \boldsymbol{p}^{(k)}$ and $\delta \lambda^{(k)}$ are independent from each other eq. (5.7) yields two conditions for the optimality of the parameter correction vector $\Delta \boldsymbol{p}^{(k)}$

$$\Delta \boldsymbol{p}^{(k)} = -(\nabla^2 o(\boldsymbol{p}^{(k)}) + \lambda^{(k)} \boldsymbol{I})^{-1} \nabla o(\boldsymbol{p}^{(k)}) \tag{5.8}$$

$$\Delta \boldsymbol{p}^{(k)T} \Delta \boldsymbol{p}^{(k)} = h^{(k)2}. \tag{5.9}$$

If $\|\Delta \boldsymbol{p}^{(k)}\| = \|(\nabla^2 o(\boldsymbol{p}^{(k)}))^{-1} \nabla o(\boldsymbol{p}^{(k)})\| < h^{(k)}$ then $\Delta \boldsymbol{p}^{(k)}$ represents an unconstrained minimizer and the optimization problem from eq. (5.5) can be solved with $\lambda^{(k)} = 0$. In this case $\|\Delta \boldsymbol{p}^{(k)}\|$ represents an unconstrained Newton step whereas in all other cases eqs. (5.8) and (5.9) have to be solved simultaneously. One of the major problems with eq. (5.8) and eq. (5.9) is to find the value for $\lambda^{(k)}$ such that $\Delta \boldsymbol{p}^{(k)T} \Delta \boldsymbol{p}^{(k)} = h^{(k)2}$. Dennis (Dennis, 1983) shows that there exists a unique solution for $\lambda^{(k)}$ and also gives implementation details for the solution of eqs. (5.8) and (5.9).

The iteration is continued by setting $\boldsymbol{p}^{(k+1)} = \boldsymbol{p}^{(k)} + \Delta \boldsymbol{p}^{(k)}$ until one of the convergence criteria for the objective function $o(\boldsymbol{p})$ is met. Usually different absolute and relative convergence criteria are used at the same time and the iteration is stopped as soon as one of the criteria is fulfilled.

5.1.2 Application to sums of squares

If the objective function consist of a sum of squares special methods exist which use this structure advantageously. The gradient $\nabla o(\boldsymbol{p}^{(k)})$ and the *Hessian matrix* $\nabla^2 o(\boldsymbol{p}^{(k)})$ needed for the solution of eqs. (5.8) and (5.9) are obtained from eq. (5.1)

$$\nabla o(\boldsymbol{p}^{(k)}) = \boldsymbol{A}(\boldsymbol{p}^{(k)}) \boldsymbol{r}(\boldsymbol{p}^{(k)})$$

$$\nabla^2 o(\boldsymbol{p}^{(k)}) = \boldsymbol{A}(\boldsymbol{p}^{(k)})\boldsymbol{A}(\boldsymbol{p}^{(k)})^T + r_i(\boldsymbol{p}^{(k)})\nabla^2 r_i(\boldsymbol{p}^{(k)}), \tag{5.10}$$

where i runs through $i = 1...m$ and

$$\boldsymbol{A}(\boldsymbol{p}^{(k)}) = \left[\nabla r_1(\boldsymbol{p}^{(k)}), \nabla r_2(\boldsymbol{p}^{(k)}) \ \ldots \ , \nabla r_m(\boldsymbol{p}^{(k)})\right] \tag{5.11}$$

is the $q \times m$ *Jacobian matrix.* q denotes the number of target parameters and m represents the number of residual functions $r(\ )$ introduced in eq. (5.1). In eq. (5.10) the Hessian matrices $\nabla^2 r_i(\boldsymbol{p}^{(k)})$ of the functions $r_i(\boldsymbol{p}^{(k)})$ are needed. Since $\boldsymbol{r}(\boldsymbol{p}^{(k)})$ is being minimized in a least squares sense, it is often the case that the components $r_i(\boldsymbol{p}^{(k)})$ are small. This suggests that a good approximation to $\nabla^2 o(\boldsymbol{p}^{(k)})$ might be (Fletcher, 1987)

$$\nabla^2 o(\boldsymbol{p}^{(k)}) \approx \boldsymbol{A}(\boldsymbol{p}^{(k)})\boldsymbol{A}(\boldsymbol{p}^{(k)})^T. \tag{5.12}$$

The gradient of all functions $r_i(\boldsymbol{p}^{(k)})$ can be approximated by

$$\nabla_j(r_i(\boldsymbol{p}^{(k)})) = (r_i(\boldsymbol{p}^{(k)} + \epsilon \boldsymbol{e}_j) - r_i(\boldsymbol{p}^{(k)})) / \epsilon, \tag{5.13}$$

where $\boldsymbol{e}_j$ is a unit vector corresponding to the direction of the j-th target parameter and ϵ is a small perturbation parameter. Eq. (5.13) shows that to evaluate the objective function $o(\boldsymbol{p}^{(k)})$ and the gradient $\nabla(r_i(\boldsymbol{p}^{(k)}))$ at one point the functions $r_i(\boldsymbol{p}^{(k)})$ have to be evaluated $q+1$ times.

The evaluation of the functions $r_i(\boldsymbol{p}^{(k)})$ requires one finite element simulation of the aspiration experiment. The finite element simulation is the computationally most expensive part of the inverse solution. The evaluation of the objective function $o(\boldsymbol{p}^{(k)})$ and the gradient evaluation from eq. (5.13) can be split up in $q+1$ separate tasks, which can be calculated on $q+1$ processors. This parallel computing was carried out on a PC cluster consisting of 12 PCs, each of it being a two processor PC (with two Alpha 21264 processors working at 666 MHz). This cluster (see Fig. 5.2) was set up by A. Rhomberg (Rhomberg, 2000). The IMSL routines are run on a SUN Ultra 10 (master) which communicates with the PC cluster. After each optimization step the finite element calculations are sent out to the different processors. The results of the $q+1$ finite element simulations are sent back to the master which performs an iteration step and then sends out the new finite element simulations. With this PC cluster the computa-

tion time for one parameter estimation run was reduced by a factor of 30-50 as compared to the single processor machine (SUN Ultra 10) used previously. Another advantage of the parallel computation is, that as long as each of the $q+1$ finite element simulations can run on its own single processor, an increase in the number q of target parameters does not increase

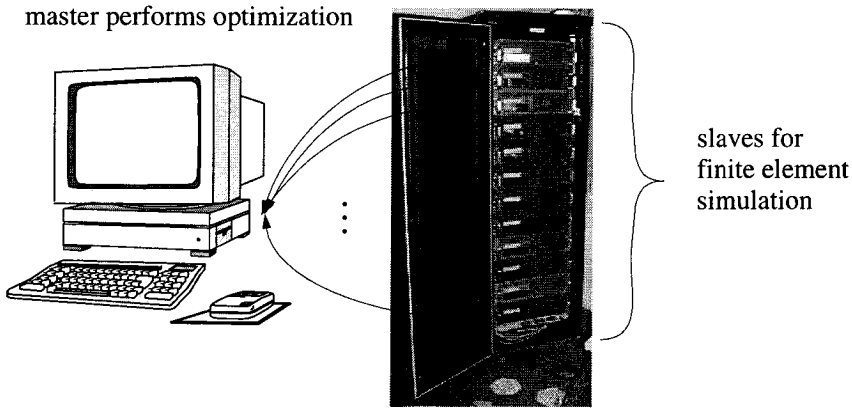

Fig. 5.2 Parallel computation for parameter estimation

the computer time involved for the parameter estimation (apart from the fact that an increase in the number of target parameters often tends to destabilize the estimation of the optimal target parameters).

5.2 Estimation of material parameters

The above presented optimization algorithm is used for the estimation of the material parameters for different material laws, including the time dependent viscoelastic material properties. The general form of the material laws used in this work is

$$S(x,t+\Delta t) = S^e(C(x,t+\Delta t)) + \int_0^{t+\Delta t} \sum_{i=0}^{N_d} \left(c_i e^{-(t+\Delta t-s)/\tau_i} \frac{\partial}{\partial s} S'(C(x,s)) \right) ds \,. \quad (5.14)$$

The first part $S^e(C(x,t+\Delta t))$ on the right hand side of the eq. (5.14) represents the fully relaxed material answer that is obtained at time scales that are very large as compared to the largest relaxation time τ_{N_d} in the model if the material deformation is kept constant. The second term on the right hand side of eq. (5.14) represents the history depending part of the stresses that decays with time as soon as the deformation of the material is kept

constant. When a material corresponding to the material model in eq. (5.14) is deformed the deformation activates a specific set of relaxation times τ_i. The specific activated relaxation times in the material model are related to the frequency content of the applied deformation. The highest observed stretch rate in the material undergoing a certain deformation determines the value τ_0 of the lowest discernible relaxation time in the material model (see Fig. 5.3). When the material deformation is kept con-

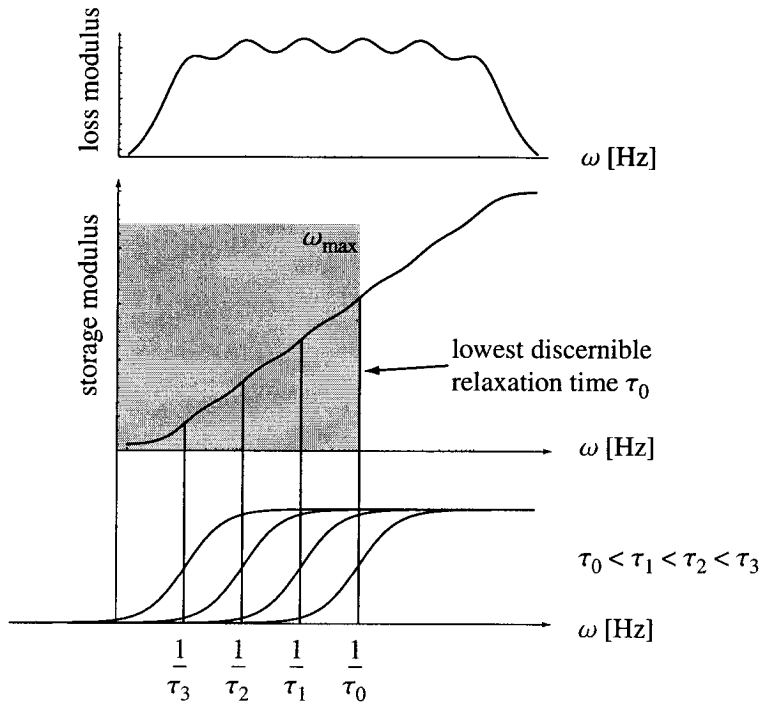

Fig. 5.3 Storage and loss modulus for a linear viscoelastic model corresponding to a series of reduced exponential relaxation functions

stant from some point on material relaxation is observed. This material relaxation continues until the fully relaxed material answer, corresponding to the elastic answer $S^e(C(x, t+\Delta t))$, is obtained. The time after which the fully relaxed material answer is obtained is related to the largest relaxation time τ_{N_d} in the material model. In contrast to linear viscoelasticity the nonlinear material behaviour does not allow to strictly relate the relaxation times to the decay time of the history depending part in eq. (5.14). The largest relaxation times in the material model are activated by a specific deformation only if the time scale at which material relaxation is caused is at least of the same order of magnitude as the largest relaxation time in the model.

To illustrate the behaviour of the optimization algorithm in connection with the material model from eq. (5.14) we first study a simple example. A uniaxial tension test as illustrated in Fig. 5.4 allows to gain some very valuable insight in the behaviour of the inverse parameter estimation algorithm. The stretch λ_i at the i-th step of the test is defined as the ratio $\lambda_i = l_i / l$ of the deformed length l_i to the undeformed length l of the tension sample. The reaction force corresponding to step i is f_i. Usually experimental data is used as reference input to the parameter estimation algorithm. In this study the experimental data acquisition process is replaced by a numerical data generation process. Reference data is generated with a known material law and preset values for the material parameters. The same material law is then used in the estimation process. The squared differences between the external forces from the reference data and the actual external forces are used as objective function. In the optimization the value of this objective function is minimized. Since in this example the reference data was generated numerically, and therefore the exact material model is known (which is a situation probably never encountered in a real experiment), strict convergence criteria in the estima-

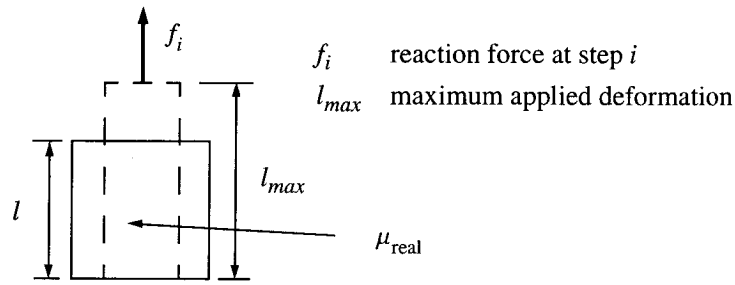

Fig. 5.4 Uniaxial tension test

tion process would in any case result in the correct parameter values which were originally used to generate the reference data. By using rather coarse convergence criteria in the parameter estimation the algorithm will stop at parameter points producing no further significant reduction of the objective function. In a real experimental situation this points often correspond to local minima. In probably all cases of inverse parameter estimation local minima are encountered. The material models used in the parameter estimation are only an approximation to the real materials and thus together with the reference data often produce objective functions that have multiple local minima, especially in cases where the experiments for the reference data acquisition are not performed in a way to avoid or at

least minimize such effects. It is the scope of this section to study these influences and to give guidelines for the conduction of the experiments which should lead to a robust parameter estimation.

The viscoelastic properties of the studied materials are modelled by the spectral approximation formulated in section 3.5. It has proven to be a good approach in the later presented parameter estimations (see Chapter 6.2) to keep the single relaxation times τ_0 to τ_3 constant and to not include them in the estimation. Only the weighting factors c_i of their respective relaxation functions are estimated together with the rest of the material parameters. As shown in the following sections the estimated values for the fully relaxed material answer and for the largest relaxation time in the material are strongly related in an inverse parameter fitting procedure. To obtain good estimates for the fully relaxed material answer a correct value of the largest relaxation time in the material model is indispensable. In the examples presented in Chapter 6 a good material characterization was obtained by choosing evenly spaced relaxation times (in logarithmic sense) in the material models, after having estimated the largest relaxation time. The continuous relaxation spectrum of the materials was approximated by sampling it at discrete locations within the spectrum. Apart from the largest relaxation time in the material model the exact location of the other spectrum sampling points is not of crucial importance for the quality of the approximation of the continuous material relaxation spectrum. The exact location of the spectrum sampling points, given by the assumed spectrum of relaxation times, is only important when materials with strong discontinuities in their relaxation spectrum are modelled.

The material laws studied here are the neo-Hookean material (eq. (3.19)) and the reduced Veronda-Westmann material law (eq. (3.20)).

5.2.1 Material parameter estimation for a viscoelastic neo-Hookean material

To describe the viscoelastic neo-Hookean material the formulation from eq. (3.19) and eq. (3.52) is used

$$\tilde{W} = \mu(I_1 - 3),$$

$$S(x, t+\Delta t) = = S^e(C(x, t+\Delta t)) + \int_0^{t+\Delta t} \left(\sum_{i=0}^{N_d} c_i e^{-(t+\Delta t-s)/\tau_i} \right) \frac{\partial}{\partial s} S'(C(x, s)) ds,$$

where the relaxation constants are chosen to be

$$\tau_0 = 0.1 \text{ [s]}, \tau_1 = 1 \text{ [s]}, \tau_2 = 10 \text{ [s]}, \tau_3 = 100 \text{ [s]} .$$

For this material model the following 5 material parameters need to be estimated in the inverse parameter estimation process

$$\mu \text{ [N/m}^2\text{]}, c_0 \text{ [-]}, c_1 \text{ [-]}, c_2 \text{ [-]}, c_3 \text{ [-]} .$$

The reference data generated with the following material parameters

$$\mu = 1700 \text{ [N/m}^2\text{]}, c_0 = 1.0 \text{ [-]}, c_1 = 1.5 \text{ [-]}, c_2 = 0.5 \text{ [-]}, c_3 = 0.2 \text{ [-]}$$

is shown on the right hand side of Fig. 5.5. The course of the prescribed stretch λ from Fig. 5.5 (left hand side) is similar to the situation encountered in our aspiration experiments. The data in Fig. 5.5 represents the only one "experiment" used in the inverse material parameter estimation. Although in the aspiration experiments the external force (given through the aspiration pressure) and not the applied stretch is prescribed the conclusions regarding the behaviour of the inverse algorithm are valid for both situations.

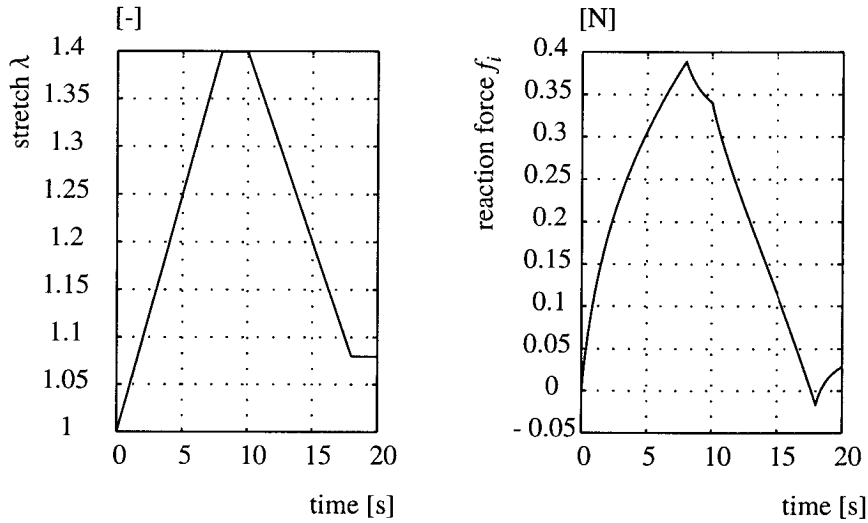

Fig. 5.5 Prescribed stretch and resulting reaction force in tension experiment

In a first example the sensibility of the inverse parameter estimation problem to the parameter values used as initial estimate is studied. Inverse parameter estimations are performed with different initial estimate values.

As input to the parameter estimation the generated reference data is employed. The iterative optimization of the target parameters is stopped when the objective function $o(\boldsymbol{p}^{(k)})$ changes less than 5% with respect to the last iteration step. This coarse convergence criterion is only used for the following theoretical study and is not applied to the evaluation of the real experiments in Chapter 6. In Tab. 5.1 the results from the parameter estimations for different initial estimates are summarized. If during the optimization one of the target parameters assumed a negative value the corresponding line in the tables containing the results is marked with an asterisk in the first column. As Tab. 5.1 shows the estimated values of the target parameters depend on the initial estimates. Additionally, it is seen that wrongly estimated constants c_i result also in a wrongly estimated elastic constant μ. It turns out that the experiment does not reveal enough

id. number	μ [N/m²]	c_0 [-]	c_1 [-]	c_2 [-]	c_3 [-]	μ [N/m²]	c_0 [-]	c_1 [-]	c_2 [-]	c_3 [-]
	initial estimate					reference values				
						1700	1.0	1.5	0.5	0.2
						estimated values				
1*	1000	0.50	0.50	0.50	0.50	1764	0.87	1.40	0.51	0.16
2*	1300	0.50	0.50	0.50	0.50	1922	0.77	1.32	0.47	0.08
3*	1500	0.50	0.50	0.50	0.50	1909	0.82	1.30	0.48	0.08
4	2200	0.50	0.50	0.50	0.10	1865	0.74	1.38	0.47	0.11

Tab. 5.1 Initial estimates and values obtained from an experiment lasting 20 seconds

information about the relaxation behaviour of the material. The duration of the experiment is not long enough as compared to the largest relaxation time. Information about the parameter μ, which characterizes the fully relaxed material answer, is only contained in experiments which enforce material relaxation at time scales similar to the largest relaxation time in the material.

Though the estimated parameters do not represent the correct material parameters they may nonetheless be used to calculate approximately correct force-displacement curves. The predicted force-displacement curves show to reflect the correct material behaviour for conditions similar to the ones of the experiment used to obtain the reference data. The duration of the experiment that is being predicted should not exceed the duration of

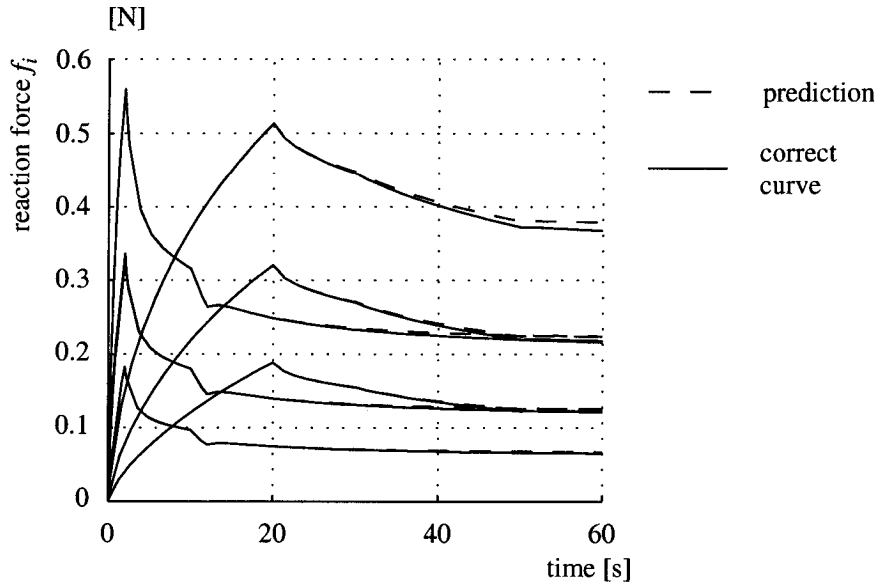

Fig. 5.6 Force-elongation curves calculated with parameter set 2 from Tab. 5.1 and with the correct parameter values (plotted over time)*

the experiment which was used to obtain the reference data. The maximum stretches should also not exceed the ones in the reference experiment, especially in cases with strongly non-linear material behaviour, and the stretch rates should be similar to the ones in the reference experiment. Fig. 5.6 shows that the predicted force-elongation curves (plotted over time for clarity) match the force-elongation curves generated with the real material parameters very well, even though set 2* of the estimated parameter values from Tab. 5.1 was used to generate the force-elongation curves. Parameter set 2* shows the largest deviation from the reference values in Tab. 5.1. The other estimated parameter sets from Tab. 5.1 result in even better agreement. They are not shown in Fig. 5.6 because they are hardly distinguishable from the one force-elongation curve plotted. It should be noted that the material behaviour can be predicted within the limits set by the reference data correctly for time scales and stretch rates different from the ones in the single experiment used to estimate the parameters. In order to enhance the match of the estimated material parameters with the known reference parameters the duration of the reference experiment is increased. The new duration of the experiment is equal to the largest relaxation time in the material $\tau_3 = 100$ [s] (which in this case is well known). The initial part of the prescribed displacement is the same as shown in Fig. 5.5. The time span at the end of the experiment where the material is subject to

relaxation with a constant stretch is prolonged. In all the following examples the same initial estimates in the same order as in Tab. 5.1 are used. Therefore they are not listed any more in the tables. The results of the esti-

id. number	μ [N/m^2]	c_0 [-]	c_1 [-]	c_2 [-]	c_3 [-]
	reference values				
	1700	1.0	1.5	0.5	0.2
	estimated values				
1*	1706	0.89	1.50	0.50	0.20
2*	1700	0.80	1.51	0.50	0.20
3*	1700	0.84	1.52	0.50	0.20
4	1706	0.78	1.52	0.50	0.20

Tab. 5.2 Parameter values obtained from an experiment lasting 100 seconds

mations for the prolonged experiment are listed in Tab. 5.2. Apart from the parameter c_0, the convergence of all parameters to their correct values is seen to be very good. The parameter c_0 shows to have only a limited influence on this experiment. The stretch rate in the experiment is too small as to reveal the material properties corresponding to this small relaxation time. Therefore, the parameter c_0 could also be neglected in the estimation. Results corresponding to this situation are given in Tab. 5.3. The esti-

id. number	μ [N/m^2]	c_0 [-]	c_1 [-]	c_2 [-]	c_3 [-]
	reference values				
	1700	1.0	1.5	0.5	0.2
	estimated values				
1*	1705	/	1.60	0.50	0.20
2*	1702	/	1.62	0.50	0.20
3*	1697	/	1.62	0.49	0.20
4	1705	/	1.61	0.50	0.20

Tab. 5.3 Parameter values obtained from an experiment lasting 100 seconds

mated values for the parameter c_1 now differ stronger from their correct values than by taking into account also the parameter c_0. This proves that,

although the estimated values of the parameter c_0 are not very reliable, it is of advantage to include this lowest relaxation time in the parameter estimation. The estimated values for the weighting factor c_1 are closer to the correct value if c_0 is included in the parameter estimation. Tab. 5.2 shows that an experiment used to assess both the elastic and the viscoelastic material properties should be of a duration at least equal to the largest relaxation time in the material model. Additionally, it proved not to be sufficient to subject the studied material to an arbitrary experiment with time duration longer than the largest relaxation time in the material. The relaxed material answer is estimated correctly only when material relaxation (at constant deformation) or creep (at constant loading) at time scales equal to or longer than the largest relaxation time in the material is enforced in the experiment.

In most cases, especially when testing biological materials, the largest relaxation time of the studied material is not known. If the influence of the material relaxation occurring at long relaxation times is small the material properties relevant for our short time experiment can nonetheless be estimated accurately. In order to prove this an additionally study is performed in which the reference material has a relaxation time larger than the largest one accounted for in the material model. The parameters used to generate the reference data are

a) $\tau_0 = 0.1$ [s], $\tau_1 = 1$ [s], $\tau_2 = 10$ [s], $\tau_3 = 100$ [s], $\tau_4 = 1000$ [s],

b) $\tau_0 = 0.1$ [s], $\tau_1 = 1$ [s], $\tau_2 = 10$ [s], $\tau_3 = 100$ [s], $\tau_4 = 10000$ [s],

and

$$\mu = 1700\ [\mathrm{N/m^2}],\ c_0 = 1.0\ [-],\ c_1 = 1.5\ [-],\ c_2 = 0.5\ [-],\ c_3 = 0.2\ [-],\ c_4 = 0.02\ [-].$$

The optimal values obtained for the 5 parameters for our material model are given in Tab. 5.4 and Tab. 5.5. The reference data was generated with the parameter set a) from above for Tab. 5.4 and with set b) for Tab. 5.5. A reasonable estimation of the material parameters is seen to be possible even though not all material relaxation times were included in the material model. However, the material model used in the estimation has at least to account for the relevant relaxation times. The error of the estimated material parameters is of course larger when the large relaxation times of the material contribute substantially to the viscoelastic behaviour, i.e. if the factors c_i with $i > 3$ in the above formulation are of the same magnitude as

the other constants c_i.

id. number	μ [N/m^2]	c_0 [-]	c_1 [-]	c_2 [-]	c_3 [-]
	reference values				
	1700	1.0	1.5	0.5	0.2
	estimated values				
1*	1749	0.86	1.46	0.49	0.19
2*	1749	0.78	1.47	0.49	0.19
3*	1757	0.77	1.46	0.49	0.19
4	1743	0.97	1.46	0.49	0.20

Tab. 5.4 Parameter values obtained from an experiment lasting 100 seconds for data set a)

id. number	μ [N/m^2]	c_0 [-]	c_1 [-]	c_2 [-]	c_3 [-]
	reference values				
	1700	1.0	1.5	0.5	0.2
	estimated values				
1*	1757	0.86	1.45	0.49	0.19
2*	1755	0.77	1.45	0.50	0.18
3*	1766	0.76	1.44	0.49	0.18
4	1750	0.97	1.46	0.49	0.19

Tab. 5.5 Parameter values obtained from an experiment lasting 100 seconds for data set b)

5.2.2 Material parameter estimation for a viscoelastic reduced Veronda-Westmann material

The same study as for the neo-Hookean material is now done for the reduced Veronda-Westmann material law from eq. (3.20)

$$\tilde{W} = \frac{\mu}{\gamma}(e^{\gamma(I_1 - 3)} - 1).$$

The reference material parameters are chosen in a way that the peak force in the simulated tensile test is approximately equal to the one observed in

the reference data for the neo-Hookean material. In Fig. 5.7 the prescribed stretch and the resulting reference force are plotted over time. The conclusions drawn for the reduced Veronda-Westmann material law are analogous to the ones for the neo-Hookean material. Additionally, the influence of the non-linearity of the material on the parameter estimation is studied. The two data sets used to generate the reference data are

a) $\mu = 1300\ [\mathrm{N/m^2}], \gamma = 0.5\ [-], c_0 = 1.0\ [-], c_1 = 1.5\ [-], c_2 = 0.5\ [-], c_3 = 0.2\ [-]$,

b) $\mu = 150\ [\mathrm{N/m^2}], \gamma = 5.0\ [-], c_0 = 1.0\ [-], c_1 = 1.5\ [-], c_2 = 0.5\ [-], c_3 = 0.2\ [-]$,

where for both parameter sets the following spectrum of relaxation times is used

$\tau_0 = 0.1\ [\mathrm{s}], \tau_1 = 1\ [\mathrm{s}], \tau_2 = 10\ [\mathrm{s}], \tau_3 = 100\ [\mathrm{s}]$.

In Tab. 5.7 the results for estimations with a simulated experiment dura-

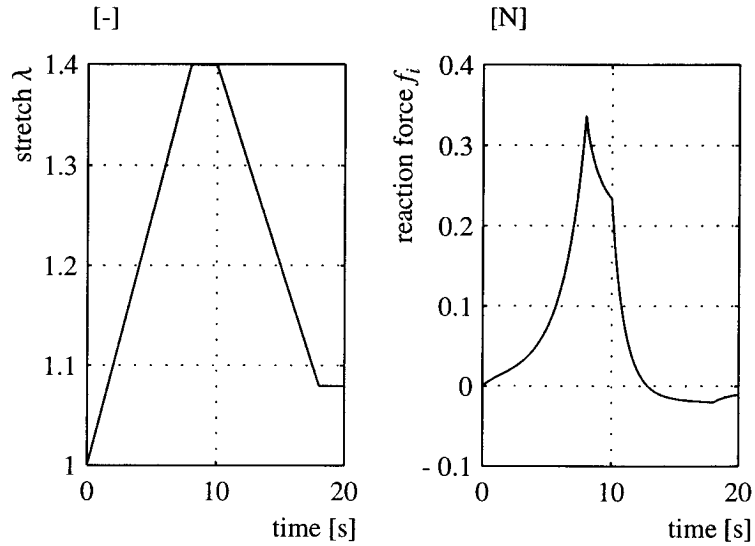

Fig. 5.7 Prescribed stretch and resulting reaction force in tension experiment

tion of 20 seconds are summarized. We see from Tab. 5.6 that again a robust estimation of the material parameters is not possible if the duration of the experiment is not at least equal to the largest relaxation time in the material. The same observation is made for a material with a stronger non-linearity (see Tab. 5.7). By performing an experiment whose duration time compares to the largest relaxation time in the material a much more robust estimation of the reference material parameters is possible. The estimated

id. number	μ [N/m²]	γ [-]	c_0 [-]	c_1 [-]	c_2 [-]	c3 [-]	μ [N/m²]	γ [-]	c_0 [-]	c_1 [-]	c_2 [-]	c3 [-]
	initial estimate						reference values					
							1300	0.5	1.0	1.5	0.5	0.2
							estimated values					
1*	600	1.00	0.50	0.50	0.50	0.50	1343	0.49	0.63	1.44	0.52	0.16
2*	600	0.10	0.50	0.50	0.50	0.50	1575	0.49	0.62	1.24	0.45	0.02
3*	1800	1.00	0.50	0.50	0.50	0.50	1557	0.50	0.62	1.27	0.45	0.03
4*	1800	0.10	0.50	0.50	0.50	0.50	1070	0.13	0.54	0.90	1.24	0.26

Tab. 5.6 Initial estimates and parameter values obtained from an experiment lasting 20 seconds for data set a)

id. number	μ [N/m²]	γ [-]	c_0 [-]	c_1 [-]	c_2 [-]	c_3 [-]	μ [N/m²]	γ [-]	c_0 [-]	c_1 [-]	c_2 [-]	c_3 [-]
	initial estimate						reference values					
							150	5.0	1.0	1.5	0.5	0.2
							estimated values					
1*	600	6.0	0.5	0.5	0.5	0.5	188	5.34	0.49	0.88	0.41	-0.09
2*	600	3.0	0.5	0.5	0.5	0.5	200	4.96	0.59	1.09	0.48	-0.08
3*	50	6.0	0.5	0.5	0.5	0.5	146	5.00	0.70	1.59	0.51	0.23
4*	50	3.0	0.5	0.5	0.5	0.5	146	5.00	0.70	1.58	0.51	0.22

Tab. 5.7 Initial estimates and parameter values obtained from an experiment lasting 20 seconds for data set b)

id. number	μ [N/m²]	γ [-]	c_0 [-]	c_1 [-]	c_2 [-]	c_3 [-]
	reference values					
	1300	0.5	1.0	1.5	0.5	0.2
	estimated values					
1*	1311	0.50	0.62	1.51	0.50	0.19
2*	1293	0.40	0.61	1.55	0.55	0.22
3*	1297	0.50	0.63	1.55	0.50	0.20
4	1295	0.49	0.61	1.55	0.51	0.20

Tab. 5.8 Parameter values obtained from an experiment lasting 100 seconds for data set a)

id. number	μ [N/m^2]	γ [-]	c_0 [-]	c_1 [-]	c_2 [-]	c_3 [-]
	reference values					
	150	5.0	1.0	1.5	0.5	0.2
	estimated values					
1*	155	4.98	0.59	1.50	0.50	0.17
2*	151	4.99	0.72	1.53	0.50	0.20
3*	149	4.99	0.67	1.56	0.50	0.21
4	151	5.02	0.67	1.49	0.50	0.19

Tab. 5.9 Parameter values obtained from an experiment lasting 100 seconds for data set b)

values obtained in estimations using reference experiments with longer duration are summarized in Tab. 5.8 and Tab. 5.9. Also here it is seen that the optimal values of the parameter c_0 are not reliable. But, omitting the parameter c_0 in the parameter estimation has a worse effect on the optimal values of the other parameters than taking it into account.

5.2.3 Summary

From the preceding study follows that the weighting factors corresponding to the spectrum of relaxation times of a material can be determined with one single experiment. This single experiment, however, needs to reveal information at least about the largest and the smallest discernible relaxation time accounted for in the material model. If these two limiting relaxation times are far apart from each other in the spectrum of relaxation times one should also be concerned with revealing material information about the relaxation times in between these two limiting relaxation times in the experiment. The following observations are guidelines for the inverse parameter estimation and for the conductance of experiments in connection with the inverse parameter estimation for a quasi-linear viscoelastic material law.

- The largest relevant relaxation time in the material can only be estimated robustly if the corresponding experiment has a duration similar to the value of this largest relaxation time and also reveals material information regarding these time scales.
- If relaxation times larger than the duration of the experiment are included in the material model non-unique parameter sets depending

on the initial estimates may result in the inverse fit. The different resulting estimated parameters can nonetheless be used to correctly predict the material behaviour within the time, stretch and stretch rate limits set by the reference experiment.

- Better estimated values of the smallest discernible relaxation time (here, discernible is always meant as discernible in the performed experiment) are obtained by including a single relaxation time, one order of magnitude smaller, in the spectrum approximation. Though the estimated value of the weighting factor of this smaller relaxation time is not reliable it minimizes the error in the estimation of the weighting factor of the larger neighbouring relaxation time.
- The sampling frequency of the experimental data has to be adapted to the smallest relaxation time which is estimated to influence the experiment. A minimum sampling frequency of $f \approx 1 / \tau_0$ [s^{-1}] is required in order to allow a detection of these fastest decaying stresses in the material.

5.3 Sensitivity to geometrical model errors

In an *in-vivo* aspiration experiment we usually have only little information about the structure of the aspirated tissue and the geometry of any underlying tissue layers. However, in the inverse parameter estimation algorithm we need an exact model of the situation as a basis for the finite element simulation. Thus it becomes important to know the sensitivity of the estimated material parameters to errors in the assumed geometry of the finite element model. In order to quantify these parameter errors reference data is generated with well known material parameters and a well defined finite element model. In a second step the material parameters are estimated with the inverse algorithm using a finite element model with quantified geometrical errors. A model consisting of two layers is used to study the influence of the assumed thickness of the upper layer on the estimated material parameter values. The extreme case of an underlying tissue with no material stiffness is considered. Since, apart from situations in which soft tissue covers boney or cartilagenous material, the underlying tissue usually can be assumed to have a stiffness similar to the one of the upper layer, this special situation represents an extreme case. In common situations with an underlying soft tissue layer of similar stiffness a smaller influence of the assumed top layer thickness on the estimated parameters of the top layer is observed. When the tissue is assumed to stick to the

aspiration tube, the assumed thickness of the topmost tissue layer has a smaller influence on the estimated material parameters as compared to the case in which the tissue is gliding along the basis of the aspiration tube. Since in our aspiration experiments the tissue surface is wiped dry the tissue can be assumed to stick to the aspiration tube (compare the friction measurements in Chapter 6.3). As in the previous sections the neo-Hookean and the reduced Veronda-Westmann material behaviour are studied. The material parameters used to generate the reference data are in the case of the neo-Hookean material model

$$\mu = 1800\ [\mathrm{N/m^2}],\ c_0 = 2.0\ [-],\ c_1 = 2.0\ [-],\ c_2 = 1.0\ [-],\ c_3 = 0.3\ [-]\,,$$

and in the case of the reduced Veronda-Westmann material

$$\mu = 150\ [\mathrm{N/m^2}],\ \gamma = 5.0\ [-],\ c_0 = 2.0\ [-],\ c_1 = 2.0\ [-],\ c_2 = 1.0\ [-],\ c_3 = 0.3\ [-]\,.$$

The different relaxation times τ_i were chosen equal in both cases

$$\tau_0 = 0.1\ [\mathrm{s}],\ \tau_1 = 1\ [\mathrm{s}],\ \tau_2 = 10\ [\mathrm{s}],\ \tau_3 = 100\ [\mathrm{s}]\,.$$

The largest relaxation time $\tau_3 = 100\ [\mathrm{s}]$ of the material determines also the required duration of the reference experiment in order to avoid multiple parameter sets in the inverse solution. Consequently, the duration of the reference experiment is chosen to be $100\ [\mathrm{s}]$. The aspiration pressure history is taken from a typical aspiration experiment. For both material laws the assumed top layer thickness h in the different models scales as follows as compared to the thickness h_0 of the model used to generate the reference data

$$h = 1.56h_0,\ h = 1.24h_0,\ h = 0.80h_0,\ h = 0.64h_0\,,$$

where $h_0 \approx 9\ [\mathrm{mm}]$ is the thickness of the reference model. With a reference model with larger reference thickness h_0 the influence on the estimated material parameters diminishes in the inverse algorithm if the same relative geometrical model errors as above are assumed. The larger the top layer thickness the closer is the problem to an infinite half-space problem. In the infinite half-space problem the thickness of the assumed layer is equal to infinity and does therefore not influence the solution of the problem. The results for the neo-Hookean material are summarized in Tab. 5.10. The largest resulting relative error in the estimated parameters is 22%. The material stiffness, represented by the parameter μ, results to be

	μ [N/m^2]	c_0 [-]	c_1 [-]	c_2 [-]	c_3 [-]
	reference values				
	1800	2.0	2.0	1.0	0.3
h / h_0 [%]	estimated values				
156	1727	2.22	1.91	1.0	0.27
125	1775	2.27	1.91	1.0	0.26
80	1976	2.52	1.84	0.99	0.25
64	2188	2.25	1.82	0.99	0.24

Tab. 5.10 Estimated parameters in the presence of model errors for the neo-Hookean material law

the most sensitive quantity in the material model regarding errors in the thickness h of the finite element model. Tab. 5.10 shows that in the case of an uncertain top layer thickness h it is preferable to assume large values for the thickness h. The errors in the estimated material parameters are smaller if too large a top layer thickness is assumed instead of too small a top layer thickness.

The same study is now performed with the reduced Veronda-Westmann material. The results are summarized in Tab. 5.11. The largest relative error is 18% and corresponds to the wrongly estimated parameter μ in the

	μ [N/m^2]	γ [-]	c_0 [-]	c_1 [-]	c_2 [-]	c_3 [-]
	reference values					
	150	5.0	2.0	2.0	1.0	0.3
h / h_0 [%]	estimated values					
156	139	5.16	2.20	2.11	0.94	0.31
125	143	5.09	2.10	2.10	0.97	0.31
80	161	4.86	2.01	1.86	1.05	0.29
64	176	4.77	1.98	1.91	1.04	0.26

Tab. 5.11 Estimated parameters in the presence of model errors for the reduced Veronda-Westmann material law

case of the smallest assumed model thickness h. Though the relative errors in the estimated coefficient γ are relatively small, with a maximum

relative error of 4.6%, their influence becomes increasingly important when material stretches larger than in the reference experiment are considered.

Chapter 6

Results

In the first section of this chapter we discuss the problems that arise when both material parameters of a Mooney-Rivlin material law have to be estimated in an inverse process. It is shown that reference experiments with moderate stretches ($\lambda \leq 1.3$) do not allow the desired robust estimation of both material parameters μ and α. For stretches between $\lambda \approx 0.7$ and $\lambda \approx 1.5$ the neo-Hookean model is proposed instead of the Mooney-Rivlin formulation.

Then, the results of an experimental validation of the tissue aspiration method are presented. The validation tests were performed on a synthetic material and not on soft biological tissues in order to avoid any influence of tissue altering, tissue ageing or tissue conditioning on the tests. Results of the inverse parameter estimation from aspiration experiments and of the control experiments are presented for the synthetic material.

In a second part of this chapter we present measurements and experiments performed *ex-vivo* on soft biological tissues. The presented results were mostly obtained from experiments on pig kidneys. The intra-operative *in-vivo* and *ex-vivo* application of the tissue aspiration method on human uteri and the results from these experiments are presented in the last part of this chapter.

6.1 Validation of the inverse parameter estimation

As already mentioned above the experimental validation of the inverse finite element parameter estimation using data gained from aspiration

experiments was carried out on a synthetic material and not on biological soft tissues. Wacker Silgel 612 turned out to have a stiffness similar to the one of soft biological tissues encountered in the previously performed aspiration tests. Silgel 612 is a pourable, two component silicone rubber, that cures to a very soft gel-like vulcanizate. The mixing ratio of the two components of the silgel allows to adjust the hardness of the silicone rubber. To ensure that the two different samples used in the aspiration experiment and the control tension tests have the same mechanical properties they were cast using the same mixture. The two samples were dried for about three weeks. The samples were dyed with red ELASTOSIL paste to augment the visibility with the video camera in the aspiration experiment. In Fig. 6.1 the two silgel samples used in the validation experiments are

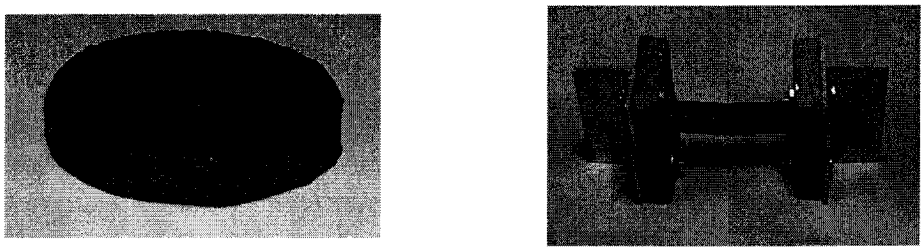

Sample used for aspiration test

Sample used for tension test

Fig. 6.1 Silgel samples

shown. The sample on the left hand side has a little spherical bush at the centre of the top surface. This bush was cast to ensure visibility of the top surface with the optics of the aspiration tube also in the undeformed stress-free configuration. As shown in Fig. 6.2 the finite thickness of the base of

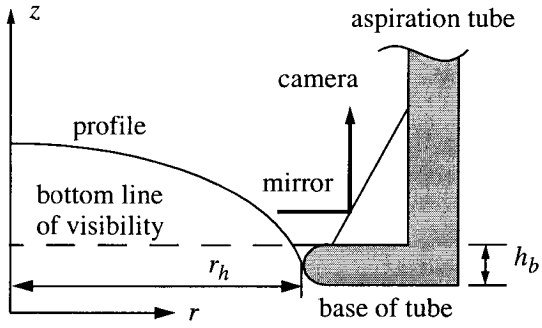

r_h radius of base hole of aspiration tube

h_b thickness of base of aspiration tube

Fig. 6.2 Profile viewing with camera

the aspiration tube causes some loss of information regarding the contour of the material surface. The finite element mesh for the parameter estimation procedure is based on the profile information of the undeformed sample surface. The profile information is transformed into a format that can be imported into the commercial preprocessor MENTAT. In MENTAT the mesh generation is done and a job-file is created which is then used in our own code for the finite element simulation of the aspiration experiment.

6.1.1 Parameter estimation for the Mooney-Rivlin material law

Preliminary tension tests performed on the silgel tension sample suggested that the material behaviour of the silgel might be modelled with a Mooney-Rivlin material model. The Mooney-Rivlin material law is often used to model rubber material for moderate stretches and also in biomechanics to model cartilaginous tissues, brain tissue etc. The determinability of the Mooney-Rivlin material parameters is studied in this section. The Mooney-Rivlin material law was already presented in Chapter 3. For the theoretical studies of this section the totally incompressible formulation of the Mooney-Rivlin material law with the following strain energy function is used

$$W = \mu_{real}(I_1 - 3) + \alpha_{real}(I_2 - 3)\,. \tag{6.1}$$

The condition $I_3 = 1$ is required to hold for the specified deformation.

In a purely analytical process the properties of the inverse parameter estimation are studied in connection with the Mooney-Rivlin material law. A uniaxial tension test is employed in this study as a simple possibility to

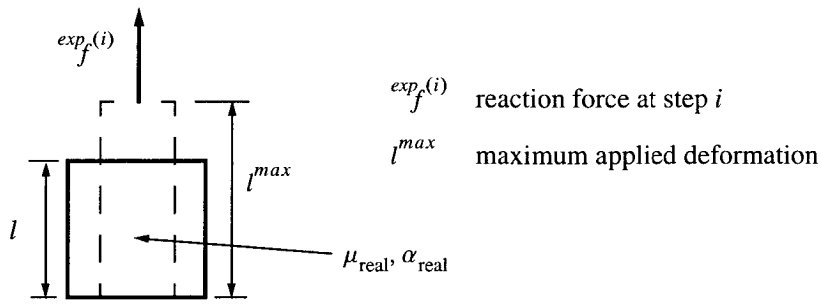

Fig. 6.3 Uniaxial tension test

estimate the material parameters μ_{real} and α_{real} of the Mooney-Rivlin material law. A material sample with a square unit cross-section of initial length l is stretched to a length l^{max} in n steps. The lateral surfaces of the

sample are free of any surface tension. The incompressibility condition of the material relates the longitudinal stretch $\lambda_1^{(i)} = l^{(i)} / l$ at step i with the lateral contraction

$$\lambda_2^{(i)} = \lambda_3^{(i)} = 1 / \sqrt{\lambda_1^{(i)}}. \tag{6.2}$$

The stretch $\lambda_1^{(i)}$ has been assumed to lie in the direction of the first coordinate axis. The reaction force ${}^{exp}f^{(i)}$ corresponding to the stretch $\lambda_1^{(i)} = l^{(i)} / l$ is measured at every load step $i = 1...n$. The reaction force at step i can be calculated from eq. (6.1)

$${}^{exp}f^{(i)} = 2\left(\lambda_1^{(i)} - \frac{1}{(\lambda_1^{(i)})^2}\right)\left(\mu_{real} + \frac{\alpha_{real}}{\lambda_1^{(i)}}\right). \tag{6.3}$$

In an ideal parameter estimation process the correct material model with the unknown material parameters μ and α is used in the inverse parameter estimation algorithm. The reaction force calculated with the unknown material parameters μ and α results to

$$f^{(i)} = 2\left(\lambda_1^{(i)} - \frac{1}{(\lambda_1^{(i)})^2}\right)\left(\mu + \frac{\alpha}{\lambda_1^{(i)}}\right). \tag{6.4}$$

In the parameter estimation process the sum over all load steps n of the squared differences $({}^{exp}f^{(i)} - f^{(i)})^2$ between the "experimentally" determined reaction forces ${}^{exp}f^{(i)}$ and the reaction forces $f^{(i)}$ is minimized

$$\begin{aligned} o(\mu, \alpha) &= \sum_{i=1}^{n} ({}^{exp}f^{(i)} - f^{(i)})^2 \\ &= \sum_{i=1}^{n}\left(k^{(i)}\bar{\mu}^2 + \frac{k^{(i)}}{(\lambda_1^{(i)})^2}\bar{\alpha}^2 + \frac{2k^{(i)}}{\lambda_1^{(i)}}\bar{\mu}\bar{\alpha}\right), \end{aligned} \tag{6.5}$$

where $k^{(i)} = 4(\lambda_1^{(i)} - 1 / (\lambda_1^{(i)})^2)$, $\bar{\mu} = \mu_{real} - \mu$, and $\bar{\alpha} = \alpha_{real} - \alpha$. Eq. (6.5) can be written as a quadratic form

$$o(\mu, \alpha) = \begin{bmatrix} \bar{\mu} & \bar{\alpha} \end{bmatrix} \begin{bmatrix} A_{11} & A_{12} \\ A_{12} & A_{22} \end{bmatrix} \begin{bmatrix} \bar{\mu} \\ \bar{\alpha} \end{bmatrix} = \begin{bmatrix} \bar{\mu} & \bar{\alpha} \end{bmatrix} \boldsymbol{A} \begin{bmatrix} \bar{\mu} \\ \bar{\alpha} \end{bmatrix} \tag{6.6}$$

with

$$A_{11} = \sum_{i=1}^{n} k^{(i)}, \quad A_{12} = \sum_{i=1}^{n} k^{(i)} / \lambda_1^{(i)}, \quad A_{22} = \sum_{i=1}^{n} k^{(i)} / (\lambda_1^{(i)})^2.$$

In eq. (6.6) $o(\mu, \alpha)$ describes a hyperboloid over the μ-α plane. The minimum of this objective function assumes the value zero (when the estimated parameters are equal to the real material parameters $\mu_{real} = \mu$, $\alpha_{real} = \alpha$). If the material is stretched to l^{max} ($\lambda_1^{max} = l^{max} / l$) within one single load step all parameter values fulfilling the condition

$$\mu_{real} - \mu + \frac{1}{\lambda_1^{max}} (\alpha_{real} - \alpha) = 0 \tag{6.7}$$

result in a value of the objective function equal to zero $o(\mu, \alpha) = 0$ and no

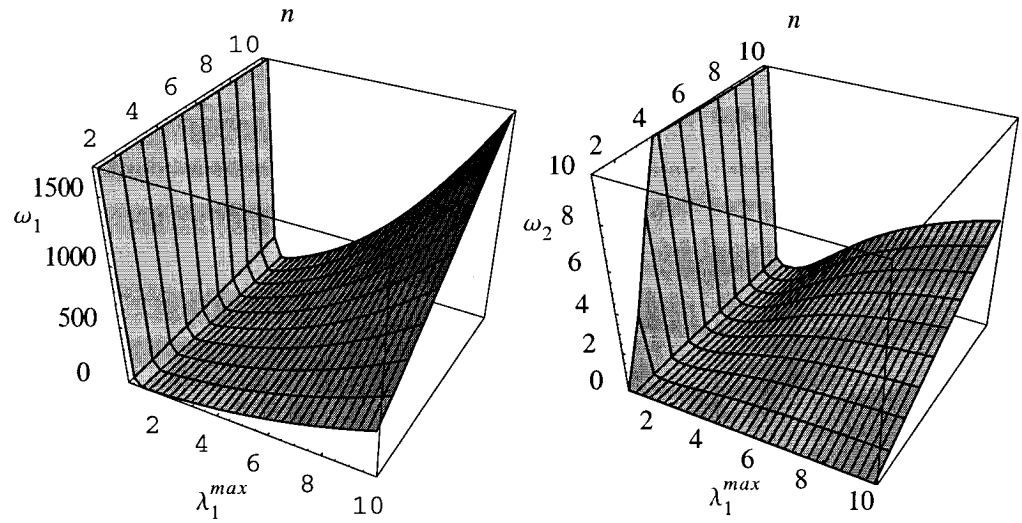

Fig. 6.4 Eigenvalues ω_1 and ω_2 of $\boldsymbol{A}$ for different numbers of load steps n and different applied maximum stretches λ_1^{max}.

unique solution to the minimization problem exists. Two material parameters can obviously not be fitted with only one single experimental data

point.

The eigenvalues ω_1, ω_2 of the matrix A in eq. (6.6) are inversely propor-

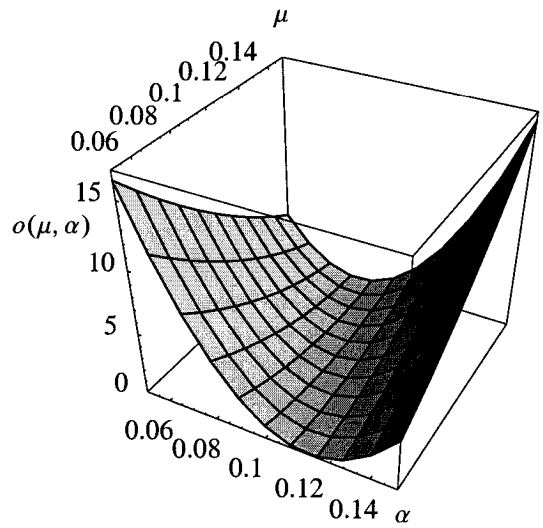

Fig. 6.5 Residual surface for $\mu_{real} = 0.1$ $\alpha_{real} = 0.1$ *and* $\lambda_1^{max} = 0.3$ *(compression) and* $n = 10$

tional to the principle radii of curvature of the surface of the objective function at the optimal solution $\bar{\mu} = \bar{\alpha} = 0$ and thus contain valuable information about the convergence properties of the optimization problem at

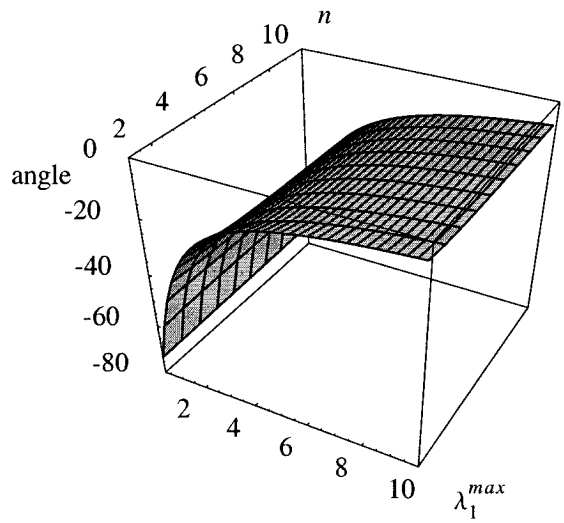

Fig. 6.6 Angle between the principle direction corresponding to the major radius of curvature and the α *axis in the* μ, α *plane*

this point. As shown in Fig. 6.4 the two principle radii of curvature of the

surface $o(\mu, \alpha)$ assume strongly differing values. Due to this the surface $o(\mu, \alpha)$ in general has a small and a large radius of curvature at $\bar{\mu} = \bar{\alpha} = 0$ as depicted in Fig. 6.5. This means that all solutions lying on the principle direction of curvature corresponding to the larger radius of curvature result in very small values of the objective function $o(\mu, \alpha)$. In an experimental study any measurement errors will result in a shift of the minimum of the objective function along this direction. The only way to avoid this quasi-singularity of the solution is to combine two experiments where the two directions corresponding to the larger radius of surface curvature include a relative angle of $90°$. Fig. 6.6 shows the variation of the direction corresponding to the major radius of curvature depending on the maximum applied stretch in the experiment. Adding the objective functions of an experiment with compressive deformation and an experiment with tensile deformation results in a superposed objective function with the desired shape (see Fig. 6.7). The large deformations required to obtain this optimal

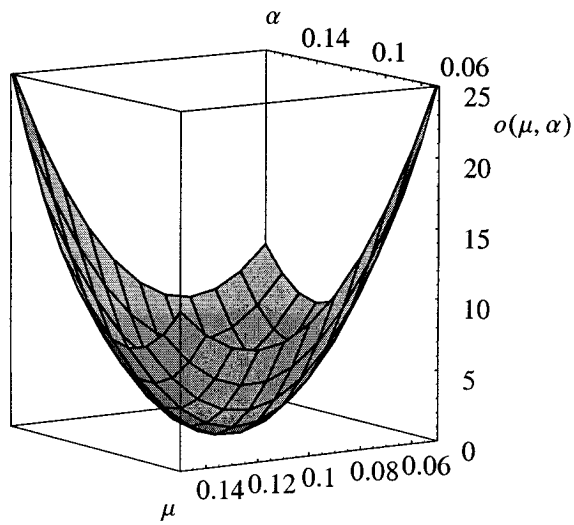

Fig. 6.7 Residual surface for combined compression-tension experiment ($\mu_{real} = \alpha_{real} = 0.1$, $\lambda_1^{max} = 0.3$ *in the compression test,* $\lambda_1^{max} = 20$ *in the tension test)*

shape of the surface representing the objective function in the case of uniaxial experiments do not allow the use of this estimation technique for the Mooney-Rivlin material in *in-vivo* applications. The above example shows that with a uniaxial deformation a robust estimation of both material parameters of the Mooney-Rivlin material is not possible.

Also Rivlin and Saunders (Rivlin, 1951) showed that the terms $I_1 - 3$ and $I_2 - 3$ in the Mooney-Rivlin material formulation depending on the first

and second invariant I_1, I_2 are equal up to the third order $O(e^3)$, i.e.

$$I_1 - 3 = -4(e_2e_3 + e_3e_1 + e_1e_2) + O(e^3),$$

$$I_2 - 3 = -4(e_2e_3 + e_3e_1 + e_1e_2) + O(e^3), \tag{6.8}$$

where $\lambda_1 = 1 + e_1, \lambda_2 = 1 + e_2, \lambda_3 = 1 + e_3$ was set for the principal stretches λ_i. The incompressibility condition is used for the above derivation. This fact again shows that for moderate stretches the neo-Hookean material formulation may well be used instead of the Mooney-Rivlin formulation. Another possibility of identifying the parameters of a Mooney-Rivlin material model is given by biaxial testing. In biaxial testing we might deform the material in a way to keep either the first or the second term in eq. (6.1) equal to zero or at a constant value. This requires the ability to exactly control the principal stretches during the experiment which is again not possible in *in-vivo* situations.

However, in modelling biological soft tissues the Mooney-Rivlin material does not play an important role. If soft tissues behaving like a Mooney-Rivlin material are encountered, the neo-Hookean formulation may be used instead to approximate the tissue behaviour for moderate stretches. For larger stretches the Mooney-Rivlin formulation might be adequate only in very special situations since its force-elongation behaviour is not at all typical for most soft tissues. As shown later the neo-Hookean material law, which is a reduced form of the Mooney-Rivlin material law, is a good description for the silgel material used in our experiments.

6.2 Material parameter estimation for the Silgel sample

A number of aspiration and tensile experiments on Silgel 612 were performed during a period of a few months. In the performed experiments aging effects of the silgel material were observed. The silgel material is subject to a constant drying process and therefore the different results presented in Fig. 6.12 and Fig. 6.13 cannot be strictly compared. The corresponding measurements were performed within two months time. In order to eliminate the effects of material aging the tensile experiments were always performed the same day as the aspiration experiments. The aspiration silgel sample and the silgel sample for the tension test were cast from the same mixture in order to ensure that both samples undergo the same

aging process. The thickness of the aspiration sample was chosen equal to the lateral dimension of the tensile sample in order to guarantee similar diffusion and thus aging conditions for both samples.

Preliminary simulations and tension tests showed that a neo-Hookean model is adequate to describe the material behaviour of the studied silgel. In Fig. 6.8 an experimental force-displacement and a simulated force-displacement curve for a tension test are compared qualitatively. The left hand side of Fig. 6.8 shows the experimentally determined force-displacement curve and the right hand side displays the simulation of the test with the material parameter μ suitably chosen in a way to fit the experiment. The right hand side of Fig. 6.8 is not the result of an inverse parameter estimation. The experimental data was obtained with the tension test sample shown in Fig. 6.1. The length of the tension test sample is 50 [mm]. Fig. 6.8 shows that the neo-Hookean model is well suited to describe the material behaviour of the silgel. The maximum displacement in Fig. 6.8

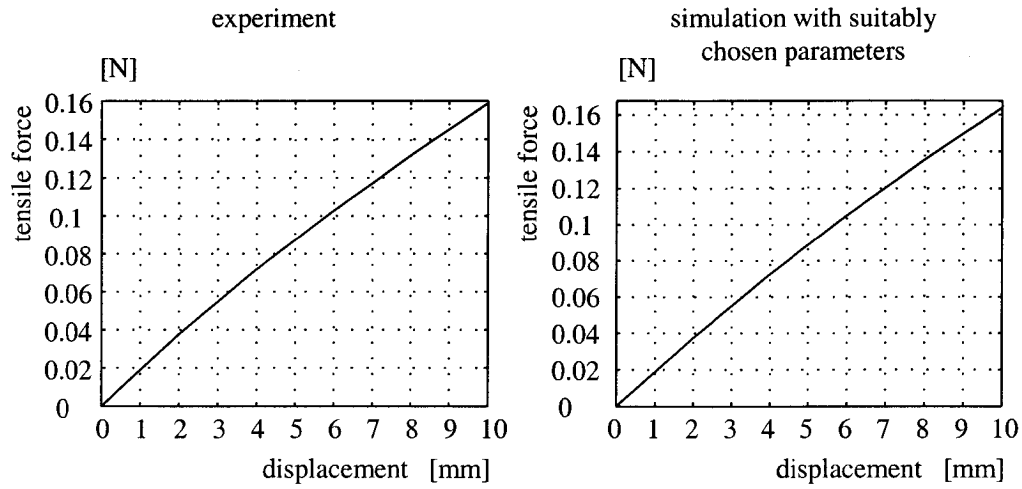

Fig. 6.8 Experimentally determined and simulated force-displacement curve for silgel and neo-Hookean material law

corresponds to a maximum stretch ratio of the sample of $\lambda = 1.2$. In Fig. 6.8 the fully relaxed material answer is shown, i.e. that all transient parts of the material response have decayed.

For clarity we recall the strain energy function for the neo-Hookean material description

$$\overline{W} = \mu(J_1 - 3) + \frac{1}{2}\kappa(J_3 - 1)^2 .$$

The bulk modulus κ is set to $\kappa = 10^7$ [N/m^2] for all following simulations. The neo-Hookean material law is combined with eq. (3.52) to reflect the viscoelastic material properties. To approximate the relaxation spectrum of the material four reduced relaxation functions $c_i e^{-(t-s)/\tau_i}$ are used. In a first step the relaxation times τ_i and their weighting factors c_i are estimated from an aspiration experiment through an inverse fit. As shown in section 5.2 there exists a strong relation between the estimated values of the largest relaxation time, c_3 in this case, and the material constant μ in the neo-Hookean material model in an inverse parameter estimation. A robust estimation of the constants μ and c_3 is only possible if the experiments are performed according to the guidelines from section 5.2.3. The value of μ was determined in a tension experiment and resulted to be $\mu = 1810$ [N/m^2]. With this information it was possible to determine the value of the largest material relaxation time τ_3 in an inverse parameter fit. The other three relevant material model relaxation times were distributed evenly spaced depending on the value of τ_3

$$\tau_i = 10^{i-3} \cdot \tau_3 \qquad i = 0 \ldots 2 .$$

For the largest relaxation time τ_3 a value of $\tau_3 = 36$ [s] was found. The obtained material relaxation times were then again used in an inverse parameter estimation but were kept constant during the iterations. Only the corresponding weighting factors c_i and the constant μ were fitted to the experimental data. Since the largest relaxation time in the material model $\tau_3 = 36$ [s] is smaller than the duration of the aspiration experiment (which is 100 seconds) the estimated material parameter sets converged in the vicinity of one single set (see section 5.2 for further explanations). Although the conditions to obtain a single and not multiple estimated parameter sets set up in section 5.2 are fulfilled one cannot blindly use any values as initial estimates in the inverse parameter estimation. The range of reasonable initial parameter estimates is limited also by the finite element simulation. Very small elastic parameters e.g. result in large deformations and thus often cause an abortion of the simulation due to a diverging solution.

Since the employed material model is only an approximation of the real material encountered the robustness of the inverse parameter estimation is expected to be inferior to the theoretically determined one from section 5.2. In Tab. 6.1 the results of three different material parameter estimations for a single silgel aspiration experiment are summarized. The

id. nr.	initial estimate					estimated values				
	μ [N/m^2]	c_0 [-]	c_1 [-]	c_2 [-]	c_3 [-]	μ [N/m^2]	c_0 [-]	c_1 [-]	c_2 [-]	c_3 [-]
1	1600	1.0	1.0	1.0	1.0	1783	1.00	3.60	0.41	0.42
2	1300	0.7	0.7	0.7	0.7	1784	0.57	3.15	0.47	0.42
3	2000	0.4	0.4	0.4	0.4	1782	1.30	3.54	0.41	0.42

Tab. 6.1 Initial estimates and resulting parameters

weighting factor c_0 is not relevant for the material properties regarding the aspiration experiment. The value of the corresponding relaxation time is very small τ_0 = 0.036 [s] and thus hardly discernible in the rather slow aspiration experiment. To obtain better values for the weighting factor c_1 the constant c_0 was, according to the guidelines in section 5.2.3, included in the parameter estimation.

In Fig. 6.9 the experimental tip displacement of the aspirated silgel and the respective simulated tip displacement are compared. The simulation

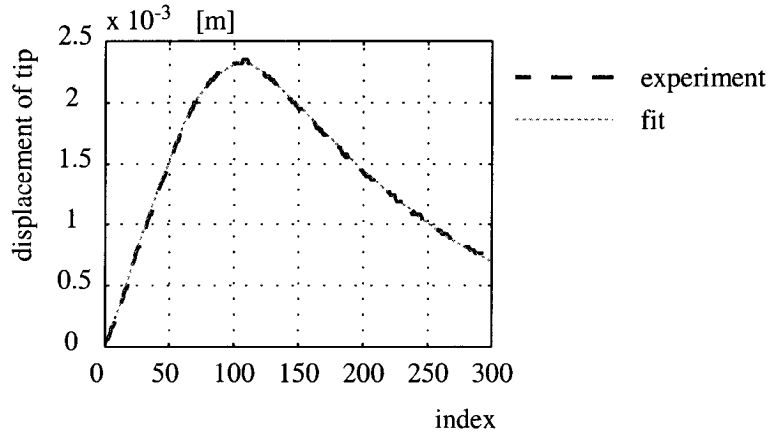

Fig. 6.9 Comparison of experiment and fit

was carried out with the estimated parameter set 1 from Tab. 6.1.

The same parameter set 1 from Tab. 6.1 is now used to predict the force-elongation curves one would measure in tensile experiments. The predictions of these force-elongation curves are then compared to real tensile experiments performed on the tensile sample from Fig. 6.1. The predicted force-elongation curves are expected to be valid for material extension ratios within the range of extension ratios encountered in the respective aspiration experiment. Also the stretches in the simulated experiments should be similar to the ones from the aspiration experiment. However,

since the neo-Hookean material is a "rather linearly" behaving material extrapolations of the material behaviour to extension ratios larger than the ones encountered in the aspiration experiment might be possible. To determine the admissible range of stretch ratios for the simulations the extension ratio distribution in the material during the aspiration experiment is computed. Fig. 6.10 shows the simulated distribution of the principle extension ratio in the aspiration experiment for the silgel material. The principle extension ratios are defined by

$$\hat{\lambda}_i = eig_i(\boldsymbol{U}) - 1\,, \tag{6.9}$$

where $eig_i(U)$ represents the i-th eigenvalue of the right stretch tensor $\boldsymbol{U}$. In Fig. 6.10 only the extension ratio maximizing $|eig_i(U) - 1|$ is depicted. The plotted values of $eig_i(U) - 1$ are evaluated at the centre of the element and are assumed to be constant within each element.

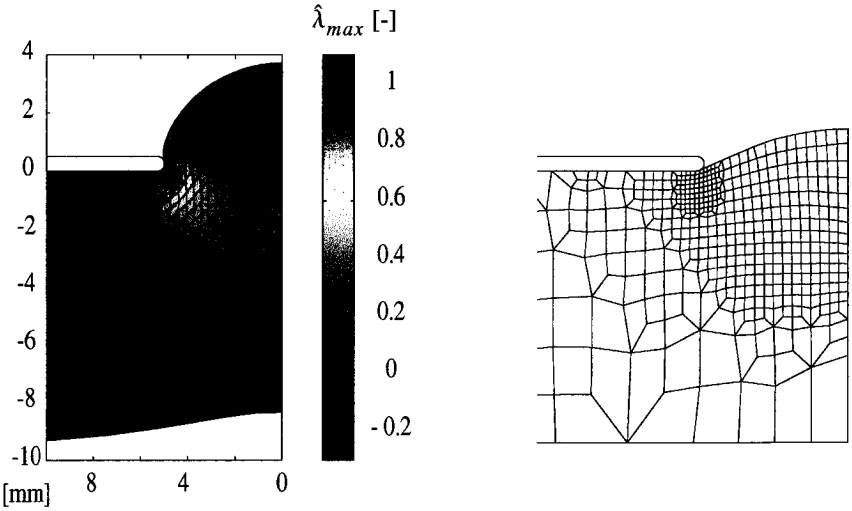

Fig. 6.10 Simulated distribution of the major principle extension ratio in the aspirated silgel at maximum tip displacement and undistorted finite element mesh

As Fig. 6.10 shows there exists quite a large area at the centre of the aspirated silgel sample with nearly constant stretch of $\lambda = \hat{\lambda}_i + 1 \approx 1.4$. Stretches larger than $\lambda \approx 1.4$ can be observed in the vicinity of the sharp corner of the base of the aspiration tube. The material parameters obtained from the aspiration experiment are expected to represent an adequate material description for stretches up to $\lambda \approx 1.4$. The maximum stretch of the material of $\lambda \approx 1.4$ is observed approximately after the first 7 seconds of the

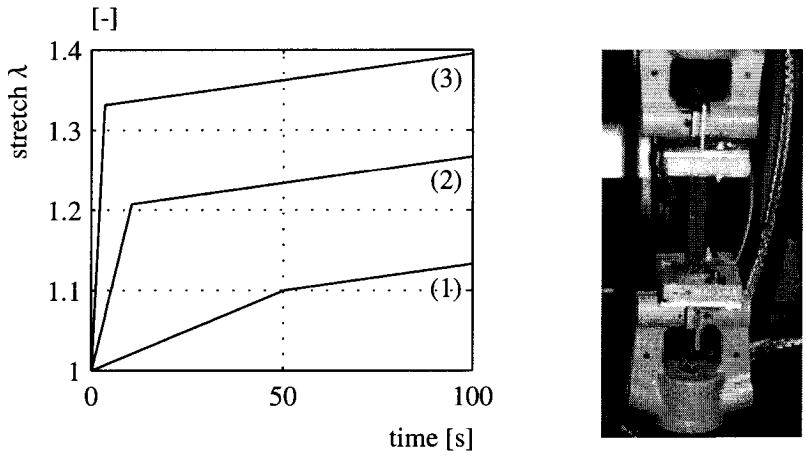

Fig. 6.11 Prescribed stretch-time curves and clamped sample

aspiration experiment. If constant straining of the material is assumed an estimate for the stretch rate in the aspiration experiment of $\dot{\lambda}$ = 0.06 [1/s] is obtained for the first part of the experiment; in the second part of the aspi-

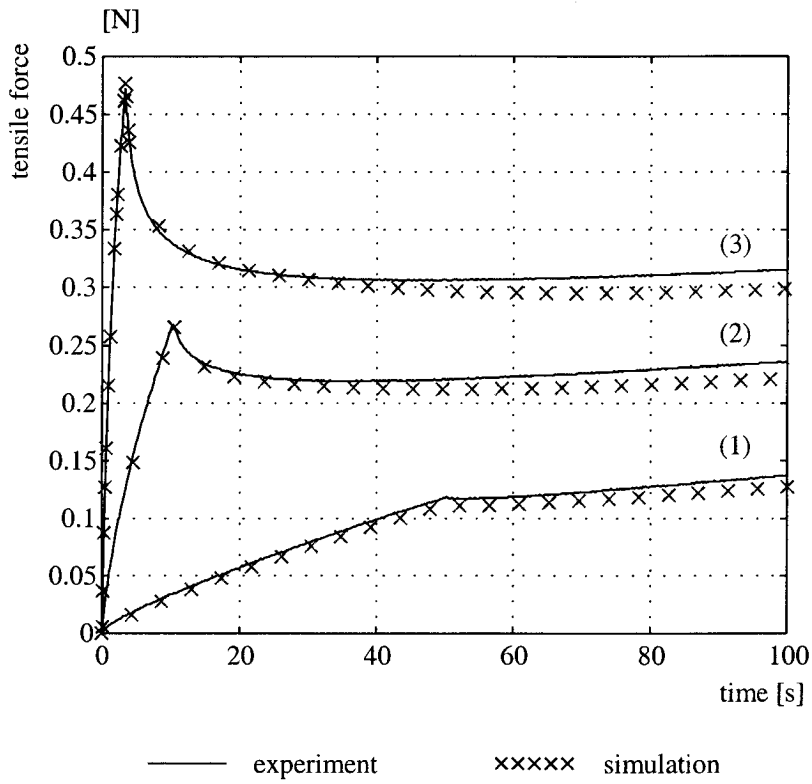

Fig. 6.12 Comparison of predicted force-time curves and experimentally determined data

ration experiment the aspirated material is released and much smaller stretch rates are observed. In Fig. 6.11 the prescribed stretch-time curves of the performed tensile experiments are shown. The stretch rates in the tensile experiments for the initial steep part of the stretch-time curve from Fig. 6.11 are $\dot{\lambda} = 0.002$ [1/s] for curve (1), $\dot{\lambda} = 0.02$ [1/s] for curve (2), $\dot{\lambda} = 0.1$ [1/s] for curve (3). After the change in crosshead speed of the tension machine the stretch rate is equal in all three tension experiments and assumes a value of $\dot{\lambda} = 7 \cdot 10^{-4}$ [1/s].

Fig. 6.12 shows that a very good prediction of the experimental data is possible with the material parameters obtained from the aspiration experiment. The observed differences between experiment and computation for the three tensile tests are summarized in Tab. 6.2. The small deviation between the measured and the computed force-displacement curves shows that a very good prediction of the experimental data is possible with the parameters obtained from the aspiration test. If the duration of the simu-

test nr.	$\lvert {}^{exp}f(i) - {}^{comp}f(i) \rvert$
(1)	0.010 [N]
(2)	0.015 [N]
(3)	0.017 [N]

Tab. 6.2 Absolute error in the force-displacement prediction

lated tensile experiment is extended to 300 seconds an approximately constant difference between the predicted and the measured force-time curves of 0.02 [N] can be observed.

In an *in-vivo* situation the value of the fully relaxed material answer (in this case characterized by the parameter μ) is not known. An estimation of the largest relaxation time, as performed for the silgel material, is thus not possible. Additionally, only aspiration experiments of short duration can be performed in an *in-vivo* situation. To demonstrate the possibility to nonetheless obtain a good material characterization parameter estimations with only estimated material relaxation times were performed. The aspiration experiments evaluated in the following have a duration of 20 seconds. These aspiration experiments were performed on an aged sample. The smallest relaxation time τ_0 is chosen to be $\tau_0 = 0.1$ [s]. The largest relaxation time τ_3 is set to $\tau_3 = 100$ [s]. The two remaining time constants are chosen evenly spaced in logarithmic sense: $\tau_1 = 1$ [s], $\tau_2 = 10$ [s]. Again, the

id. nr.	initial estimate					estimated values				
	μ [N/m^2]	c_0 [-]	c_1 [-]	c_2 [-]	c_3 [-]	μ [N/m^2]	c_0 [-]	c_1 [-]	c_2 [-]	c_3 [-]
1	1500	0.5	0.5	0.5	0.5	1814	1.05	1.62	0.34	0.19
2	2000	0.4	0.4	0.4	0.4	1881	4.61	1.07	0.39	0.12
3	2200	0.2	0.2	0.2	0.2	/	/	/	/	/
4	1300	0.7	0.7	0.7	0.7	1673	2.22	1.61	0.36	0.30

Tab. 6.3 Initial estimates and estimated parameters from an aspiration experiment with a duration of 20 seconds

relaxation times are kept constant in the parameter estimation process. The estimated material parameters for different initial estimates are summarized in Tab. 6.3. On the left hand side of Tab. 6.3 the initial estimates of the parameters in the estimation are given, whereas the right hand side lists the parameter values estimated by the algorithm. Table cells marked with a slash indicate that one of the parameters assumed a negative value during the estimation in which case the algorithm was forced to stop. Tab. 6.3 shows that the estimated parameter values depend on their initial estimates. As already explained in section 5.2 their does not exist a unique

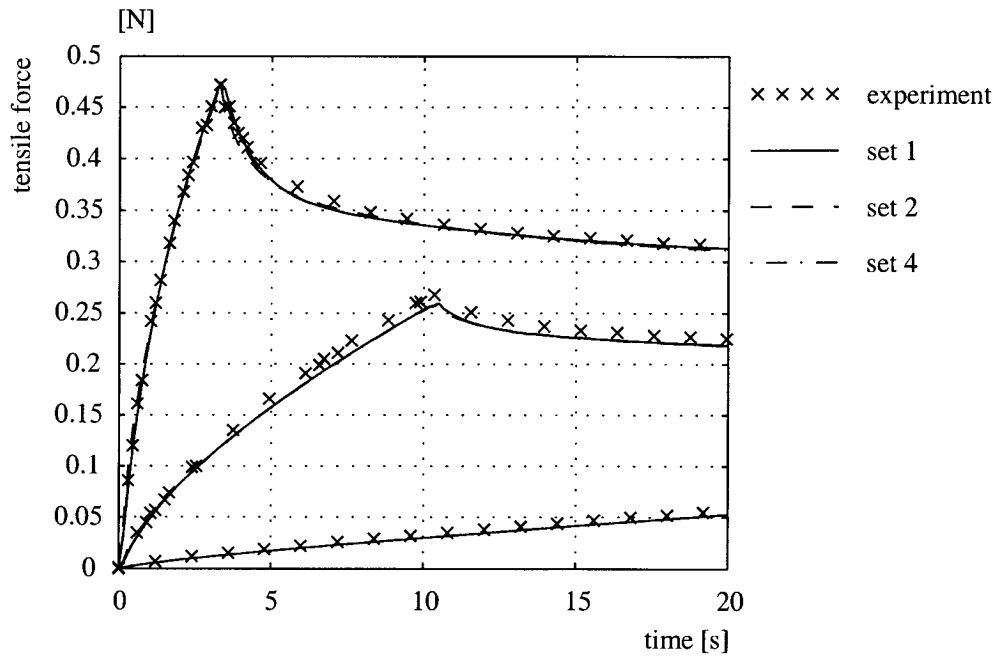

Fig. 6.13 Comparison of force-time curves, computed with the parameter sets from Tab. 6.3, with experimental tensile data

parameter fit to the experimental data if the largest relaxation time in the material model is larger than the duration of the reference experiment. However, all the above results represent a good short-term characterization of the material, in the sense that force-displacement data can very well be predicted with the estimated parameters within a limited time frame. As Fig. 6.13 shows, a good prediction of the material response is possible within a time scale equal to the duration of the aspiration experiment.

6.3 Measurements on soft biological tissues

In this section some measurements performed on soft biological tissues are presented. A number of measurements were performed on pig kidney tissue, especially on pig kidney cortex. The reason for using pig kidney in our experiments is the possibility to easily purchase pig kidney in every butcher shop and that there exists data in the literature (Farshad, 1999) which allows a comparison with our own results. A number of experiments were carried out in order to measure the friction coefficient of the renal capsule, which covers the kidney, in contact with aluminium (the aspiration tube is made of aluminium). As already mentioned earlier this friction coefficient plays an important role in the inverse material parameter estimation with the aspiration technique.

6.3.1 Friction measurements on pig kidney and liver

Though the measurement of the friction coefficient of the pig kidney capsule in contact with an aluminium surface posed many problems and the numerical values obtained for the friction coefficient might not be very reliable they give an idea of the friction conditions encountered in the aspiration experiment.

In Fig. 6.14 the experimental setup for the measurement of the friction coefficient is shown. A rotating aluminium test head was pressed against the tissue surface. A balance was used for the measurement of the contact force between the sample and the rotating test head. The test head with the form of an annulus is driven by a motor mounted on a beam. The beam's deflection, a quantity proportional to the applied torque, was measured with a differential laser interferometer. The deflection measurement is calibrated by appending small weights to the beam in a horizontal position. The measurements proved to be very sensitive to the distribution of the

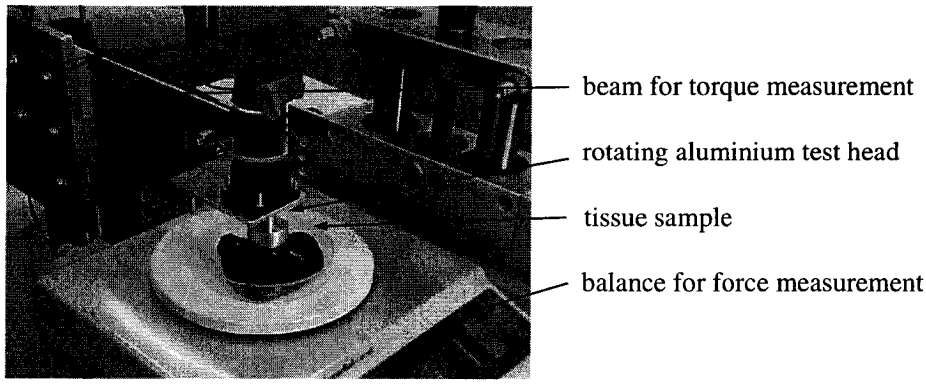

Fig. 6.14 Experimental setup for friction coefficient measurements

normal contact force at the annulus of the testing head. If the distribution of the contact force is not homogenous over the whole annulus reaction forces and torques in all coordinate directions have to be considered apart from the frictional torque. A simple relation between the measured beam deflection and the frictional torque does not exist any longer. Different experimental techniques were tested to minimize these effects but a complete avoidance of the above mentioned side effects was not possible.

Lubricant	[rpm] of the test head	Average friction coefficient [-]
Water	35	1.97
	80	1.70
	125	1.42
Ringer-solution	35	0.88
	80	0.82
	125	0.75
Glycerin	35	1.26
	80	0.77
	125	0.85

Tab. 6.4 Average friction coefficient for kidney capsule in contact with rotating aluminium test head

Three different lubricants were used to study the influence on the friction: water, Ringer-solution (a solution used for wound rinsing and infusions; also used as lubricant in tribologic studies with soft tissues) and glycerin.

With the dry kidney surface no measurements were possible, since the kidney surface too strongly stuck to the test head. The measurements were performed with three different rotational speeds of the test head. The corresponding velocities of the medium radius of the annulus are 0.027 [m/s], 0.063 [m/s], 0.098 [m/s] . These velocities are high as compared to the velocities of the tissue gliding on the base of the aspiration tube. In simulations of the aspiration experiment with no friction an average relative velocity of the tissue with respect to the aspiration tube of approximately 10^{-4} [m/s] was determined. Due to the strong adherence of the kidney surface to the test head measurements at lower rotational speeds were not possible. This fact also reflects the general observation made that the friction coefficient diminishes with increasing rotational speed of the test head. Tab. 6.4 lists the results of the friction measurements for pig kidney. The resulting friction coefficients are very high. Although the resulting values for the friction coefficients seem somewhat unrealistically high it is seen that large friction forces are acting in the contact zone of the tube and the tissue. For dry contact conditions tissue can therefore be assumed to stick to the aspiration tube. Very similar observations were made for liver tissue although the obtained friction coefficients are slightly smaller than the corresponding ones for the kidney.

6.3.2 Aspiration experiments on pig kidney

A series of aspiration experiments was performed on pig kidney. The pig kidneys were purchased at the butcher shop and then stored in the refrigerator for a maximum time of 5 hours. The pig kidney is covered by an outer

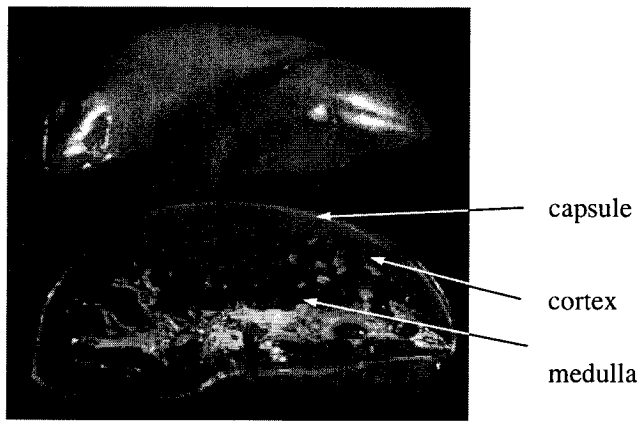

Fig. 6.15 Dissected pig kidney

membrane, called capsule (see Fig. 6.15). This capsule is very thin (estimated thickness 0.2 [mm]). Measurements published by Farshad (Farshad, 1999) indicate that the capsule is much stiffer than the underlying cortex. In our aspiration experiments the capsule was not separated from the underlying cortex and therefore an influence of the capsule on the measurements is expected. The performed aspiration experiments rather reflect the mechanical properties of the compound of capsule, cortex and medulla. The mechanical properties of the cortex were determined in preliminary tension tests. Three results of these tension tests are shown in Fig. 6.16. To cut geometrically well defined samples of cortex for the tension tests proved to be a difficult task. Since kidney cortex is a tissue with anisotropic material properties also the orientation of the sample within the organ plays an important role regarding the measured mechanical properties. The tensile data shown in Fig. 6.16 rather has the purpose to

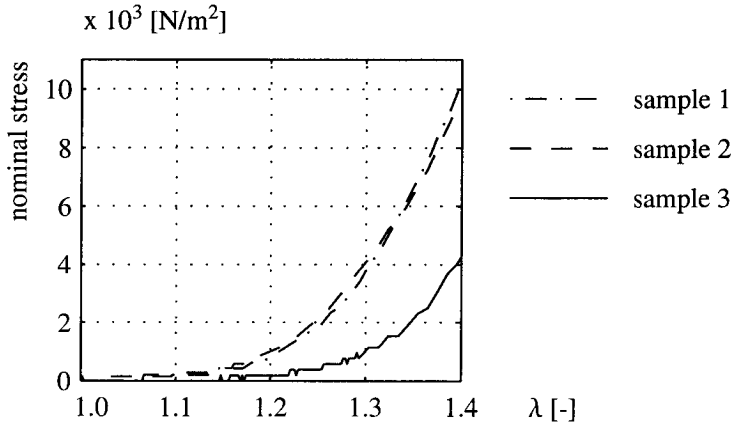

Fig. 6.16 Tensile tests for pig kidney cortex

choose the right material law for the inverse parameter estimation with the aspiration technique than to determine exact material parameters. The cortex samples from Fig. 6.16 were stretched until rupture occurred. Rupture of the cortex samples was observed at $\lambda \approx 1.6$. It is not clear from what stretch values on damaging of the cortex samples occurred, but it is assumed that it certainly started somewhat before the rupture of the samples took place.

For uniaxial tension and moderate stretches the reduced Veronda-Westmann material proves to adequately model the pig kidney cortex behaviour. For larger stretches the reduced Veronda-Westmann material law might not be adequate since pig kidney cortex shows an almost linear

stress-elongation behaviour after a strong rise in the stiffness as shown in Fig. 6.17. As also shown in Fig. 6.17 the polynomial strain energy function

$$\hat{W} = \sum_{i=1}^{N} \mu_i (J_1 - 3)^i \tag{6.10}$$

depending on the first reduced invariant J_1 is better suited to fit the cortex material behaviour. The number N of polynomial terms in eq. (6.10) was set to $N = 5$ to calculate the data in Fig. 6.17. The bulk modulus is set to

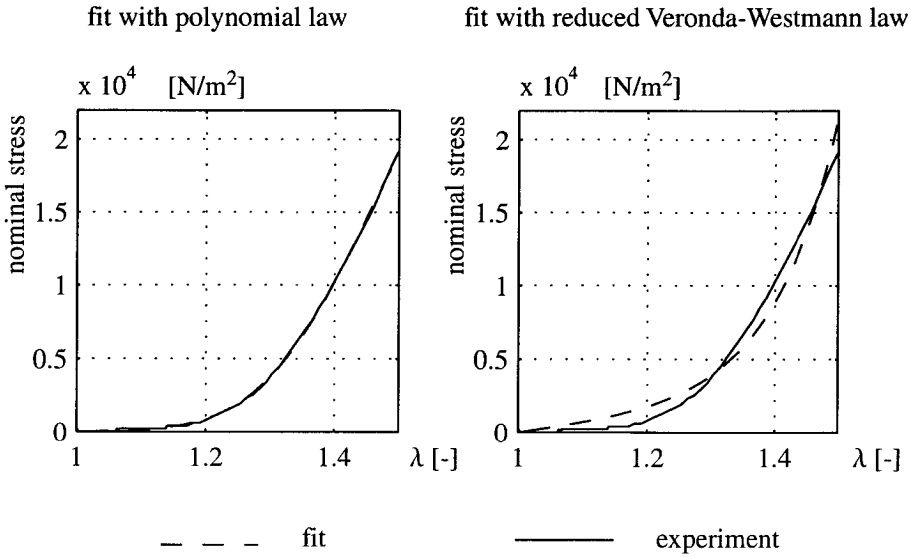

Fig. 6.17 Fit for tensile test with polynomial material law and reduced Veronda-Westmann material formulation

$\kappa = 10^7$ [N/m^2]. In the aspiration experiments the kidney cortex is covered by the capsule. In the undeformed configuration the capsule does hardly produce any material stiffening since the deformation of the tissue and the capsule occurs mainly orthogonal to the capsule. As the kidney surface is deformed in the aspiration experiment a tissue bulge is formed which is covered by the stiff capsule. The influence of the capsule increases with increasing deformation since more and more load can be transferred to the capsule. Since in the finite element model employed in the parameter estimation the capsule is not modelled separately this strong stiffness increase is erroneously attributed to the cortex.

For the material parameter estimation the values for the different relaxa-

tion times of the material are needed. Since no information about the relaxation times is available the following spectrum is assumed

$$\tau_0 = 0.05\ [s],\ \tau_1 = 0.5\ [s],\ \tau_2 = 5.0\ [s],\ \tau_3 = 50\ [s]\ .$$

It is probably not possible to determine a maximum relaxation time for the kidney cortex tissue since material creeping seems to go on for a very long time when the tissue is loaded. This fact is emphasized by the data published by Farshad (Farshad, 1999), who uses a four parameter fluid model to describe the viscoelastic properties of the cortex. The used spectrum of relaxation times contains the relaxation times relevant for the aimed at time frame in our simulations.

A number of aspiration experiments were performed on the same spot of a single pig kidney in order to show that the phenomenon of tissue conditioning can be measured with the aspiration technique. As already mentioned in section 3.1 the load-elongation curve of soft tissues shifts to the right and the hysteresis-loop narrows with increasing experiment repeti-

exper. nr.	μ [N/m^2]	γ [-]	c_0 [-]	c_1 [-]	c_2 [-]	c_3 [-]
(1)	228	5.93	2.68	0.38	1.40	0.45
(2)	113	8.23	9.11	1.48	0.45	0.08
(3)	134	7.50	7.76	0.62	0.56	0.10
(25)	154	6.21	2.30	0.22	0.59	0.25

Tab. 6.5 Parameters for the reduced Veronda-Westmann material obtained from the kidney aspiration experiments

tion number in a tissue conditioning process. After a certain number of repetitions a material state with a reproducible hysteresis loop is reached. The tissue is then said to be conditioned. 25 aspiration experiments were performed. The time interval between two aspiration experiments was about 30 minutes. Between the aspiration experiments that had only the purpose to condition the tissue, and which were not recorded, the time intervals were kept shorter. In Tab. 6.5 the results of the inverse parameter estimation for the reduced Veronda-Westmann material are summarized. In the parameter estimation a finite element model with a tissue layer thickness of 15 [mm] was employed. The model's surface opposite to the aspirated surface was seen to hardly move when the aspiration pressure was applied. An increasing layer thickness is therefore expected to have

only a marginal influence on the estimated material parameters. The estimated parameters were then used to calculate the material hysteresis in a tension experiment with subsequent forced reduction to the initial material length. The simulated crosshead speed in these tension experiments is ± 1 [mm/s]. With the sample length of 50 [mm] this results in a stretch rate of about $\dot{\lambda} = 0.02$ [1/s]. It is however difficult to compare the resulting stretch rate to the corresponding value in the aspiration experiment. Due the nonlinearity of the material continuously changing strain rates are observed in the aspiration experiment. An average value for the stretch rate in the aspiration experiment is $\dot{\lambda} = 0.05$ [1/s].

In Fig. 6.18 the hysteresis loops simulated with the parameters from

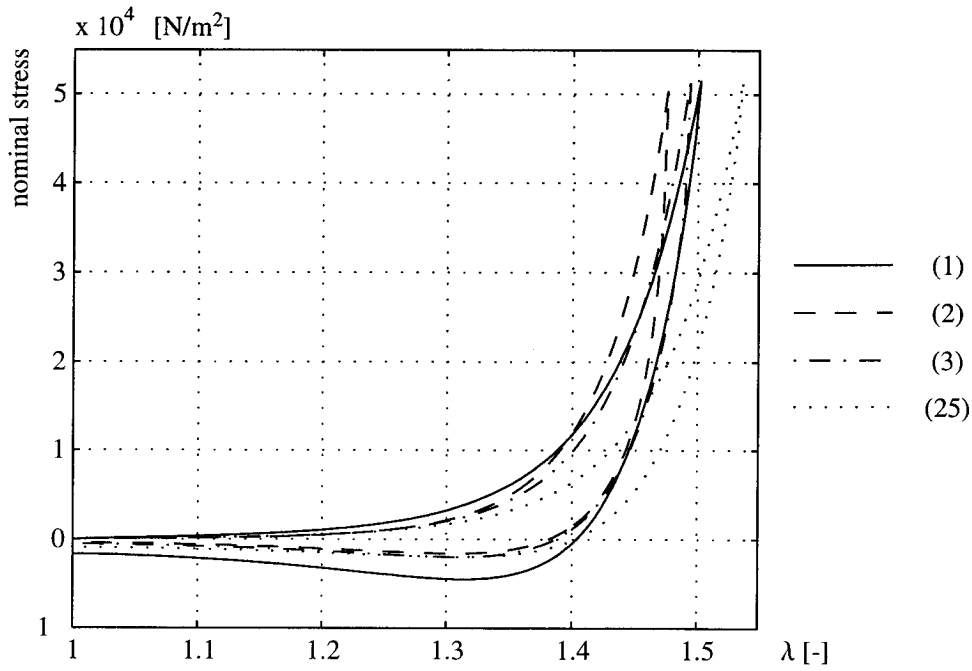

Fig. 6.18 Hysteresis loop of pig kidney cortex (covered with capsule) predicted with parameters from Tab. 6.5

Tab. 6.5 are shown. The shift to the right between experiment (1) and experiment (25) can clearly be seen as expected. However, experiment (2) and (3) do not to shift to the right as compared to experiment (1), although they are expected to do so. As shown in the following, the reduced Veronda-Westmann material is not suited for this fine tuning of the material behaviour. Also fits of aspiration data with the full Veronda-Westmann formulation from eq. (3.20) resulted only in negligible differences as com-

pared to the results obtained with the reduced Veronda-Westmann model. Therefore, an inverse parameter estimation with the material law proposed in eq. (6.10) was performed. The same relaxation spectrum as for the

exper. nr.	μ_1 [N/m^2]	μ_2 [N/m^2]	μ_3 [N/m^2]	μ_4 [N/m^2]	μ_5 [N/m^2]	c_0 [-]	c_1 [-]	c_2 [-]	c_3 [-]
(1)	274	446	631	921	8716	0.31	0.49	1.30	0.63
(2)	247	393	630	964	9696	0.22	0.04	0.89	0.31
(3)	212	456	633	800	10328	0.45	0.44	0.73	0.23
(25)	175	657	5	21	7580	0.79	0.22	0.55	0.33

Tab. 6.6 Parameters for the polynomial material law obtained from the kidney aspiration experiments

reduced Veronda-Westmann material was used. The results are listed in Tab. 6.6. These parameters are again used to compute hysteresis loops for tensile tests. Fig. 6.19 shows that now all calculated stress-elongation

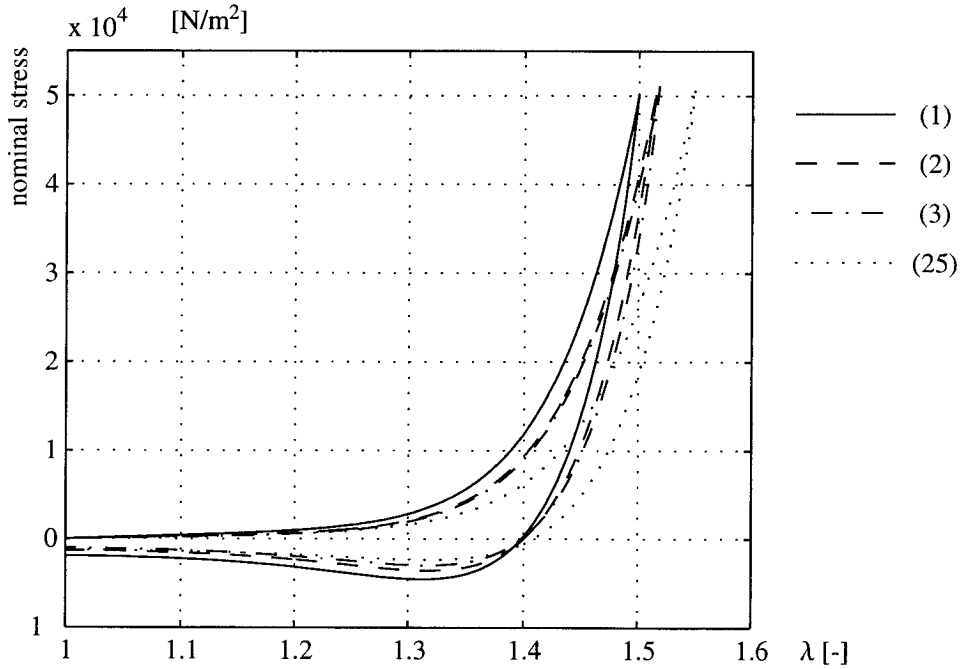

Fig. 6.19 Hysteresis loop of pig kidney cortex (covered with capsule) predicted with parameters from Tab. 6.6

curves shift to the right with increasing experiment number. The polyno-

mial material law thus proves to better reproduce the cortex material behaviour than the reduced Veronda-Westmann material formulation. However, a larger number of material parameters has to be fitted for the polynomial material law.

Comparison of Fig. 6.19 and Fig. 6.18 with Fig. 6.17, however, shows considerable differences between the predicted stress-elongation curves and the measured curves. This is attributed to:

- The data in Fig. 6.19 and Fig. 6.18 were obtained from a different pig kidney than the data in Fig. 6.17.
- In the tensile tests kidney samples without capsule were used (preliminary tests performed by F. Carter on pig liver indicate that the initial sample stiffness in indentation tests is reduced from approximately $2 \cdot 10^3 [N/m^2]$ to roughly $1 \cdot 10^3 [N/m^2]$ when the capsule is removed, see http://www-sop.inria.fr/epidaure/AISIM/CompteRendu/aisim3/thiriet_carter.html, June 2001)

Since the kidney cortex tissue is very soft, especially at small stretches, it

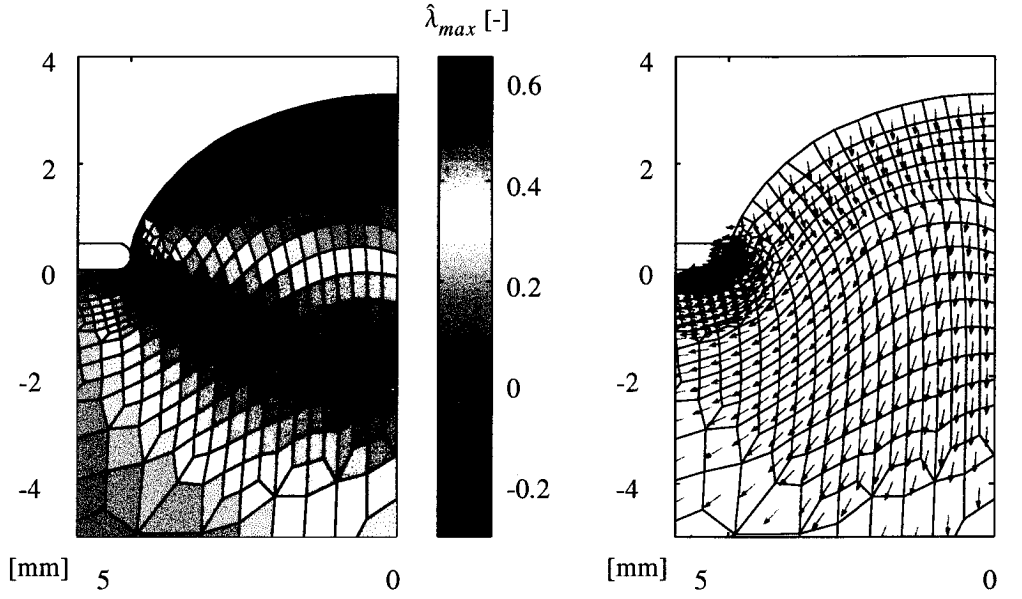

Fig. 6.20 Simulated major principle extension ratio and corresponding principle direction for the kidney aspiration experiment

proved also difficult to define the undeformed sample length in the tensile experiments. A shift of the initially very flat stress-elongation curve of the

cortex tissue can therefore not be excluded in the tensile experiments. The predicted stress-elongation hysteresis loops seem nonetheless reasonable, if one keeps in mind the differences in the experimental conditions and all the other effects, as e.g. the anisotropy of the cortex tissue, that were not included in the evaluation of the aspiration experiment.

Fig. 6.20 shows the distribution of the major principle extension ratio and the corresponding principle directions in the kidney aspiration experiment. The largest tissue deformation can be seen to occur around the sharp corner of the base of the aspiration tube. There exists also a large area of aspirated tissue with a nearly constant stretch of $\lambda_{max} = \hat{\lambda}_{max} + 1 \approx 1.5$. The stretch in this central tissue area corresponds to a tensile deformation. The deformation of the tissue in the aspiration experiment is generally characterized by tensile and only in small areas by compressive stretches. It is therefore questionable if parameters obtained from aspiration experiments can be used in simulations with mainly compressive material deformation. Depending on the direction of the tissue fibres in the aspiration experiment the soft tissue might behave very differently under compressive loading than in the aspiration experiment with mainly tensile loading.

6.4 Intra-operative in-vivo measurements

The tissue aspiration technique presented in the foregoing chapters was for the first time applied *in-vivo* on human tissue. In collaboration with the

Fig. 6.21 Intra-operative experiment on human uterus during a hysterectomy

Department of Gynaecology of the University Hospital in Zurich intra-operative measurements on human uteri were performed. From the continuum-mechanical point of view the uterus represents one of the most complex tissues one can imagine. The mechanical properties of the uterus are subject to changes during a woman's cycle. The uterus is a complex multi-layered structure with expected strongly anisotropic properties. Additionally, enormous changes in the size of the uterus occur during pregnancy. On the other hand it is of great advantage that the *hysterectomy* (removal of the uterus) is a quite frequently performed surgical intervention. Up to now measurements on 6 uteri were performed. 5 of them were excerpted after the measurements. One measurement showed too large a noise component and could therefore not be evaluated. These 6 series of measurements led to 5 data sets which were evaluated with the inverse finite element method. In some of the cases the excerpted uteri showed pathological changes. For more detailed information regarding the *in-vivo* measurements and the measurement protocol please refer to Vuskovic (Vuskovic, 2001). Due to the limited time available in the operating theatre the performed aspiration experiments were of short duration (approximately 20 seconds). Usually, three measurements at three different locations were performed before the uterus was removed, then three measurements in approximately the same positions after removal of the uterus and in one case also measurements after fixation of the uterus in formalin were carried out. The three locations were a ventral and a dorsal position and a position at the fundus of the uterus. Due to the short duration of the aspiration experiments the data obtained from these experiments is only valid for predictive simulations of the same short time range. The uterus proved to be relatively hard as compared to the previously measured pig kidney cortex. In the kidney cortex aspiration experiments extension ratios of $\hat{\lambda}_{max} \approx 0.5$ were observed whereas the extension ratios in the experiments on the uteri are approximately $\hat{\lambda}_{max} \approx 0.2$ (the maximum aspiration pressure applied in the experiments on the uteri was approximately 15% smaller than in the kidney aspiration experiments). In order to prevent any damage to the uterine tissue the maximum aspiration pressure in the experiments was not increased. Anyhow, in view of the hardness of the uterus the stretches caused by purely diagnostic interventions will not be very large and the data obtained here may well be used in a virtual reality laparoscopy simulator during purely diagnostic interventions.

In order to eliminate any influence of the natural trembling of the experimenting person on the measurements the aspiration pressure was not low-

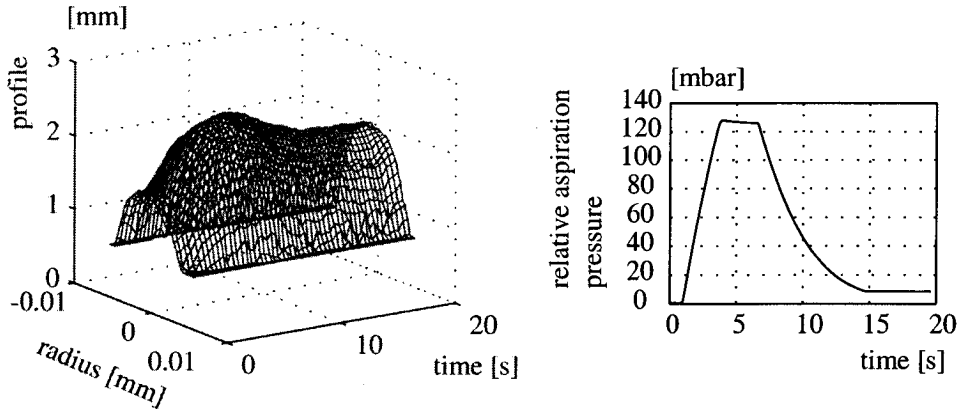

Fig. 6.22 Profile history of in-vivo measurement on uterus and corresponding aspiration pressure data

ered under a preset value after having applied the maximum aspiration pressure (see Fig. 6.22). The aspirated tissue thus remained in continuous contact with the aspiration tube throughout the whole aspiration experiment. The displacement measurement of the aspirated tissue is performed relative to the tube and should consequently not show any influence of the experimenter's trembling.

The uterus proved to be a strongly viscoelastic material. Marks caused by the aspiration experiments could be seen for a long time (approximately 20 minutes) on the uteri after the experiment had been performed. The marks vanished after a certain time period and no visible tissue damage remained. The following spectrum of relaxation times for our quasi-linear viscoelastic model was assumed

$$\tau_0 = 0.1\ [s],\ \tau_1 = 1.0\ [s],\ \tau_2 = 10.0\ [s]\ .$$

The observed strongly viscoelastic properties of the uterus would certainly require the inclusion of larger relaxation times in the material model. The robust estimation of their weighting factors c_i calls for experiments of long duration, which are currently not possible under *in-vivo* conditions. Some evaluations of the aspiration experiments including also the larger relaxation time $\tau_3 = 100.0\ [s]$ were done. With this extended spectrum of relaxation times in most evaluations negative estimates for some of the weighting factors c_i resulted. Negative weighting factors c_i are not reasonable from a physical point of view, because they lead to energy production and not to energy dissipation when the modelled material is subject to

deformation. For this reason no larger relaxation times are included in the material model in the evaluation of the experimental data.

Tensile experiments performed by Yamada (Yamada, 1970) on uteri of rabbits indicate a nearly linear stress-elongation behaviour of the uterus in tensile experiments up to extension ratios of 40%. The human uterus is assumed to mechanically behave similar and the following strain energy function is thus used to model the uterine tissue

$$\hat{W} = \mu_1(J_1 - 3) + \mu_2(J_1 - 3)^2 . \tag{6.11}$$

The first term on the right-hand side of eq. (6.11) is equal to a neo-Hookean material which has a flattening force-elongation behaviour in tension. The second term on the right-hand side of eq. (6.11) allows to compensate for this flattening behaviour. The bulk modulus in the hydrostatic work term (see eq. (3.30)) is set to $\kappa = 10^7 [\mathrm{N/m^2}]$.

In the following the uteri are numbered according to the order the measurements were carried out and will be referred to as e.g. uterus 1. Tab. 6.7

uterus nr.	diagnosis	remarks	fixed in formalin	*in-vivo* data available	*ex-vivo* data available
1	uterus myomatosus	too large contact force, no parameter estimation for *ex-vivo* data at fundus	yes	yes	yes
2	uterus healthy	none	no	yes	no
3	uterus healthy	none	no	yes	yes
4	uterus healthy	none	no	yes	yes
5	uterus myomatosus	very large uterus, asp. test performed also on myoma, no parameter estimation for *ex-vivo* data at ventral position	no	yes	yes

Tab. 6.7 Overview of measured uteri

gives an overview of the experiments performed on the different uteri. Of the uteri in Tab. 6.7 only uterus 2 remained in situ. Although some of the other uteri were healthy, they were extracted because of other diagnoses.

6.4.1 Uterus 1

Uterus 1 was strongly deformed by a myoma. The parameter values obtained from the aspiration experiments on uterus 1 are listed in Tab. 6.8. In this first evaluation a negative value for the weighting factor c_0 is admitted in the evaluation of the *ex-vivo* experiment in the ventral position. Although this is not reasonable from a physical point of view the

	location of performed aspiration experiment	μ_1 [N/m^2]	μ_2 [N/m^2]	c_0 [-]	c_1 [-]	c_2 [-]
in-vivo	ventral	5708	8686	3.0	2.6	5.3
	dorsal	646	72546	1.2	37.8	28.1
	fundus	3229	15828	0.2	0.6	9.2
ex-vivo	ventral	6104	13206	-0.9	2.6	2.0
	dorsal	4043	39566	9.9	0.0	1.1
	fundus	14448	2158	0.4	1.0	0.4
ex-vivo high asp. press.	ventral	3210	25280	9.7	0.6	1.6
	dorsal	5890	45080	5.7	0.5	0.9
	fundus	too noisy measurement				

Tab. 6.8 Parameters for the polynomial material law obtained from the in - vivo and ex-vivo aspiration experiments performed on uterus 1

influence of the weighting factor c_0 on the material behaviour in the studied range of stretch rates is small. In the following negative values for the weighting factors are not admitted. If nevertheless negative values result as estimates from the experimental data the last result from the iterative estimation with all positive weighting factors c_i is taken as optimal result. The value of the objective function $o(\ )$ of this preceding iteration step is required to be close to the optimal value of $o(\ )$ which was obtained with the not allowed negative value for one or more of the weighting factors c_i.

The measurement protocol for the aspiration experiments on uterus 1 states that the aspiration instrument was pressed firmly against the uterine tissue during all experiments. This has a misleading effect on the measurements. Initial stresses are probably induced in the tissue which artificially increase the measured stiffness of the tissue. Additionally, the deformation caused by the aspiration pressure tends less to recede to the undeformed

configuration when the aspiration pressure is diminished in the aspiration experiment. A high contact force can thus lead to unrealistically high estimates for the weighting factors c_i. The *in-vivo* measurement on uterus 1 in the dorsal location was performed by pressing the aspiration tube especially hard against the uterus. The unrealistically high values for the weighting factors c_i in Tab. 6.8 are supposed to be a consequence of this high contact force. For the *ex-vivo* measurement in the ventral location a negative weighting factor c_0 resulted. As already explained in Chapter 5.2

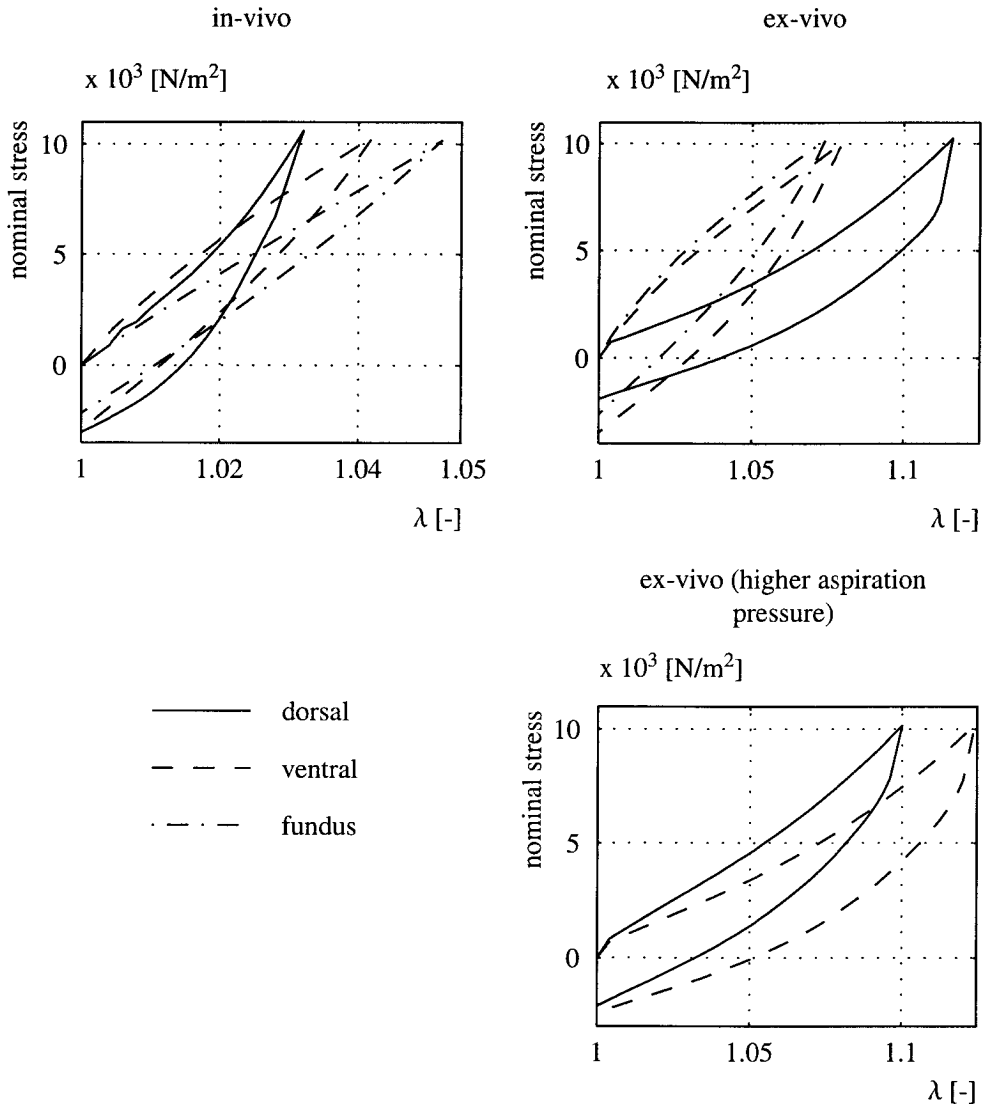

Fig. 6.23 Predicted stress-elongation curves with parameters obtained from in-vivo and ex-vivo aspiration experiments on uterus 1

the weighting factor c_0 has only a limited influence on the aspiration

experiment. The aspiration experiment is a rather slow process which is not strongly influenced by the relaxation time τ_0 = 0.1 [s]. The values estimated for the factor c_0 cannot be expected to be very reliable. The *ex-vivo* experiments on uterus 1 were performed with two different maximum aspiration pressures (110 [mbar] and 130 [mbar]). Due to the strong deformation of the uterus caused by the myoma the uterine tissue was very hard as compared to the expected hardness and also as compared to the hardness of the other uteri. The *ex-vivo* aspiration experiment with the higher aspiration pressure in the location close to the fundus of the uterus could not be evaluated because the measurement was too noisy. The reasons for this high noise component in the profile history are not known.

The parameters obtained from the evaluation of the aspiration experiments were used to predict stress-stretch curves for the uterine tissue in tensile tests. The stress-elongation hysteresis was simulated up to a maximum nominal stress of 10×10^3 [N/m^2]. After obtaining this maximum stress value in the simulated tensile tests the sample was forced to return to its initial configuration at the same stretch rate as the stretching occurred. This procedure ensures that the maximum stretches in the simulated tensile tests are approximately equal to the maximum stretches observed during the respective aspiration tests. Fig. 6.23 displays the stress-elongation curves for uterus 1. The match of the corresponding predicted stress-elongation curves between the two series of *ex-vivo* measurements is rather poor. The reasons for this poor match are not clear. The two series of *ex-*

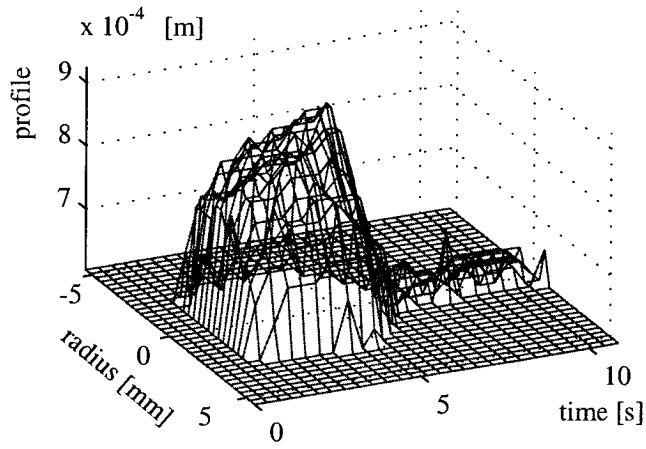

Fig. 6.24 Profile history of uterus 1 fixed in formalin

vivo measurements were expected to better match. However, it is not clear how well the same spot of tissue was re-located in the multiple experiments since no marks where placed on the tissue.

Uterus 1 was fixed in formalin after the extraction and then again subjected to a series of aspiration experiments. The prepared uterine tissue showed to be very hard and large aspiration pressures were needed to produce any deformation at all. An evaluation of these experiments was not possible due to the poor quality of the experimental data. As can be seen from Fig. 6.24 a strong reduction of the viscoelastic material properties is caused by the preparation of the uterus in formalin. The deformation caused by the aspiration experiment can be seen to recede as soon as the aspiration pressure is diminished. The mechanical properties of the *in-vivo* uterine tissue and the uterine tissue fixed in formalin are not at all comparable. As Fig. 6.24 shows no initial profile information for the undeformed tissue surface is available. The undeformed tissue surface is very flat and thus not visible due to the loss of information caused by the finite thickness of the base of the aspiration tube (see Fig. 6.2).

6.4.2 Uterus 2

Tab. 6.9 lists the parameters obtained from the *in-vivo* aspiration experiments on uterus 2. Since uterus 2 was healthy it remained *in-situ* and no *ex-vivo* measurements are available. The stress-elongation curves predicted with these parameters are shown in Fig. 6.25. As compared to uterus 1 uterus 2 is clearly much softer. The strongly viscoelastic properties of the uterine tissue manifest themselves in the broad hysteresis loop observed during loading and unloading in the simulated tensile tests.

	location of performed aspiration experiment	μ_1 [N/m^2]	μ_2 [N/m^2]	c_0 [-]	c_1 [-]	c_2 [-]
in-vivo	ventral	1637	1550	9.7	4.2	3.2
	dorsal	1437	153	1.2	2.3	7.6
	fundus	2993	9293	0.2	3.1	0.7

Tab. 6.9 Parameters for the polynomial material law obtained from the in-vivo aspiration experiments on uterus 2

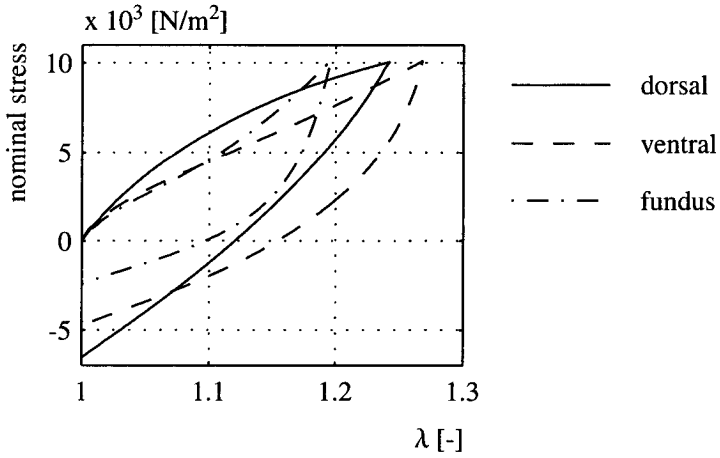

Fig. 6.25 Predicted stress-elongation curves with parameters obtained from in-vivo aspiration experiments on uterus 2

6.4.3 Uterus 3

Tab. 6.10 lists the parameters obtained from the measurements on

	location of performed aspiration experiment	μ_1 [N/m^2]	μ_2 [N/m^2]	c_0 [-]	c_1 [-]	c_2 [-]
in-vivo	ventral	1239	829	1.4	7.1	4.7
	dorsal	3044	1879	2.9	3.3	1.6
	fundus	3477	3580	0.5	5.0	1.8
ex-vivo	ventral	894	1306	1.7	3.4	1.9
	dorsal	708	3525	16.0	0.1	0.8
	fundus	754	2914	16.8	1.5	1.6

Tab. 6.10 Parameters for the polynomial material law obtained from the in - vivo and ex-vivo aspiration experiments performed on uterus 3

uterus 3. In Fig. 6.26 the predicted stress-elongation curves corresponding to the parameters in Tab. 6.10 are shown. Like in all performed experiments a pronounced decrease in the tissue stiffness is visible between the *in-vivo* and the *ex-vivo* measurements. The stiffness decrease is to one part due to a decrease in the estimated elastic material constants μ_i and to another part due to a decrease in the estimated weighting factors c_i. This decrease in the elastic stiffness is attributed at least to some part to the loss

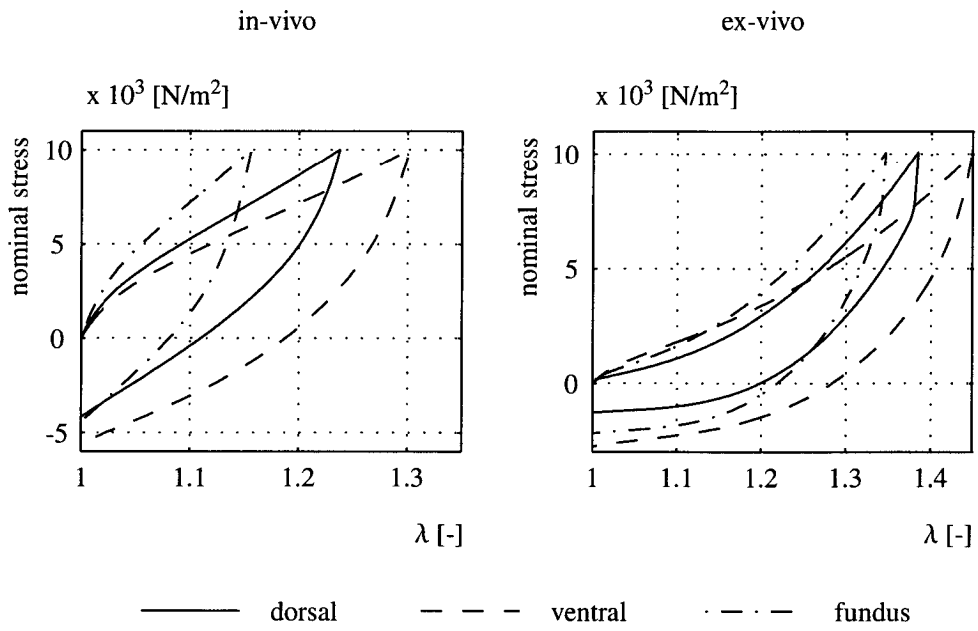

Fig. 6.26 Predicted stress-elongation curves with parameters obtained from in-vivo and ex-vivo aspiration experiments on uterus 3

of tonicity of the uterine tissue which mainly consists of muscles. The observed weakening of the tissue might to some extent also be due to the better accessibility of the tissue in the *ex-vivo* measurements. In the *ex-vivo* measurements more time is available to perform the aspiration experiments and the aspiration instrument can in general be handled with more care, which allows to diminish the initial stresses induced in the tissue by the contact with the aspiration tube. It is not clear to what extent this effect contributes to the observed diminished tissue stiffness. Here, a force sensor incorporated into the aspiration instrument could yield additional helpful information.

6.4.4 Uterus 4

Tab. 6.11 summarizes the parameters obtained from the experiments on uterus 4. The *ex-vivo* parameter evaluation for the dorsal position was restarted with an initial value for c_0 set to zero because a strongly negative value resulted as optimal fit in a first run. The last preceding estimated parameter set with all positive constants c_i showed a corresponding value of the objective function $o(\ )$ differing too much from the corresponding optimal value obtained with the negative value for c_0. An initial value of

	location of performed aspiration experiment	μ_1 [N/m^2]	μ_2 [N/m^2]	c_0 [-]	c_1 [-]	c_2 [-]
in-vivo	ventral	4171	3270	0.5	2.2	1.4
	dorsal	4571	27385	0.0	3.2	1.7
	fundus	2174	12785	6.0	1.8	1.6
ex-vivo	ventral	464	4859	24.5	0.4	0.7
	dorsal	445	2242	0.0	15.8	2.0
	fundus	764	7802	28.5	0.0	0.8

Tab. 6.11 Parameters for the polynomial material law obtained from the in - vivo and ex-vivo aspiration experiments performed on uterus 4

zero for a specific parameter forces this value to remain at this initial value since also the perturbed value of the parameter in the gradient evaluation is equal to zero. The parameter then has no influence on the value of the residual function $o(\ )$. The predicted stress-elongation curves corresponding to Tab. 6.11 are shown in Fig. 6.27. The wide hysteresis loop predicted

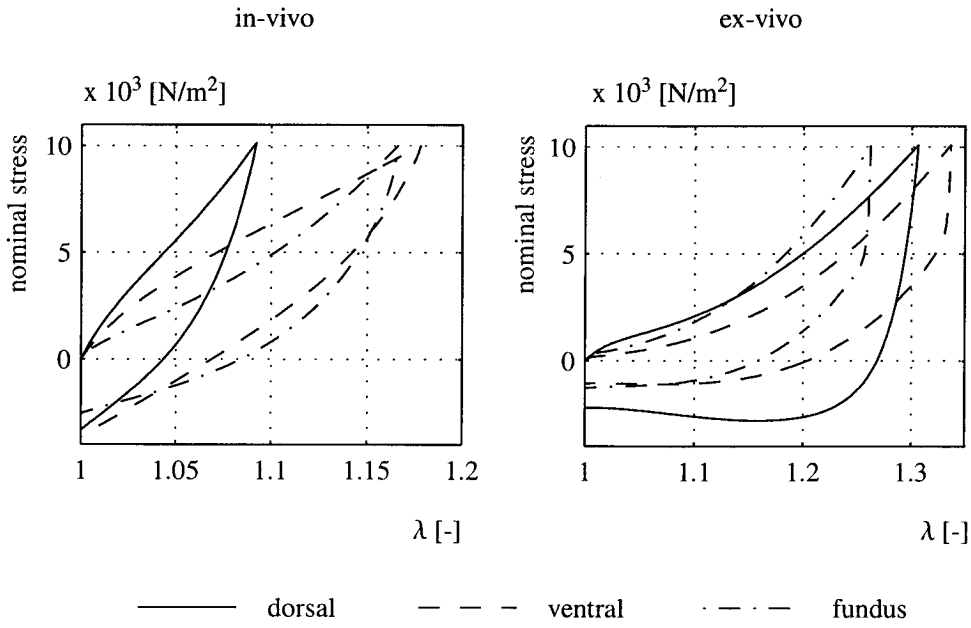

Fig. 6.27 Predicted stress-elongation curves with parameters obtained from in-vivo and ex-vivo aspiration experiments on uterus 4

for the dorsal position in the *ex-vivo* case is not due to the enforced value of zero for the weighting factor c_0 but is also observed in the original

measurement with a very slowly receding deformation of the aspirated tissue after its release.

In the *ex-vivo* measurements on uterus 4 the tissue at the fundus results to be the stiffest of all three measurements performed, whereas in the *in-vivo* measurements the dorsal location shows the stiffest material properties. In the measurement at the dorsal position possibly not the same location as during the *in-vivo* experiment was re-found in the *ex-vivo* measurement. Additionally, the dorsal position is the location which is the most difficult to access with the aspiration instrument in the *in-vivo* measurement of all specified locations on the uterus. The uterus in its natural position has to be bent upwards during the surgical intervention in order to lay open its dorsal side. This bending certainly induces initial stresses in the uterus which artificially increase the estimated material stiffness in the aspiration experiment. A quantification of this effect has not been carried out.

6.4.5 Uterus 5

Tab. 6.12 lists the parameters obtained from the measurements per-

	location of performed aspiration experiment	μ_1 [N/m^2]	μ_2 [N/m^2]	c_0 [-]	c_1 [-]	c_2 [-]
in-vivo	ventral	5642	2493	0.7	1.4	1.7
	dorsal	14513	1467	0.1	1.4	0.0
	fundus	9570	1450	0.3	1.3	0.5
	myoma	9085	3175	0.0	2.0	0.5
ex-vivo	ventral	poor measurement				
	dorsal	731	4459	0.0	2.7	0.0
	fundus	1297	9591	0.3	3.0	0.2
	myoma	2996	10452	5.1	2.9	0.8

Tab. 6.12 Parameters for the polynomial material law obtained from the in - vivo and ex-vivo aspiration experiments performed on uterus 5

formed on uterus 5. Uterus 5 was very large as compared to the other measured uteri. Its weight was about three times the weight of the other measured uteri. This huge size was due to a large myoma in uterus 5. It was difficult to distinguish healthy from unhealthy tissue on uterus 5. Additionally to the measurements at the usual three locations an extra

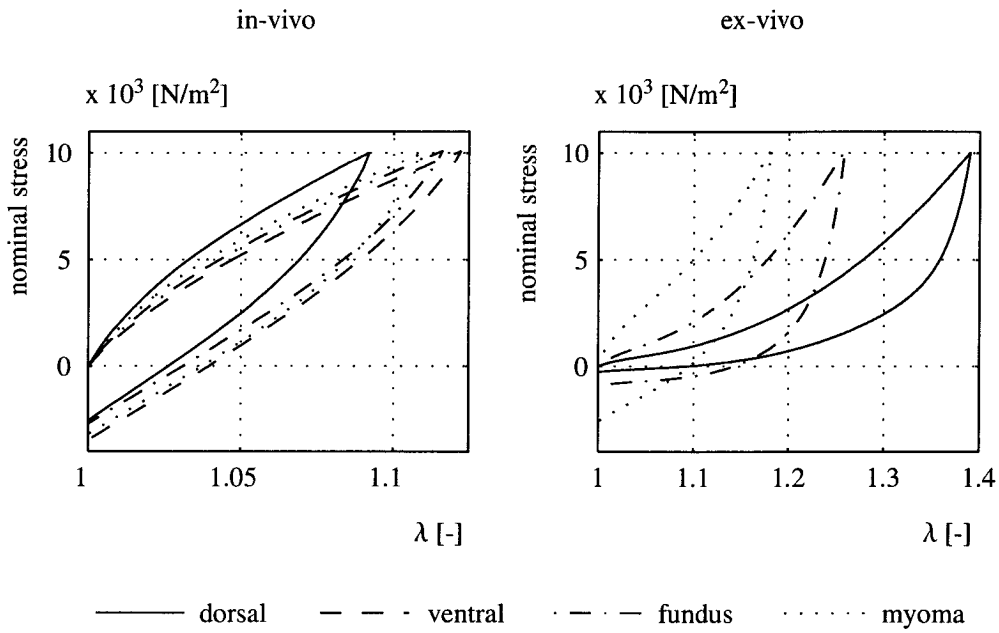

Fig. 6.28 Predicted stress-elongation curves with parameters obtained from in-vivo and ex-vivo aspiration experiments on uterus 5

aspiration experiment was performed on the myoma. As shown in Fig. 6.28 the *in-vivo* tissue properties in the different locations are all very similar. This confirms the statement in the measurement protocol that it was nearly impossible to distinguish healthy from unhealthy tissue. In contrast to the *in-vivo* tissue properties the three obtained stress-elongation curves from the *ex-vivo* measurements indicate a remarkable difference in the stiffness of the uterine tissue in the different locations. It is not clear where these differences result from. One may suspect that in all *in-vivo* measurements unhealthy tissue was measured whereas in the *ex-vivo* measurements probably both healthy and unhealthy tissue was measured.

6.4.6 Comparison of results

A comparison of the results from the different locations between *in-vivo* and *ex-vivo* measurements is generally difficult because it cannot be guaranteed that the same spot of tissue was measured before and after the removal of the uterus. A pronounced decrease in the stiffness of the uterine tissue with respect to the *in-vivo* measurements is observed in all the *ex-vivo* measurements. To what extent this effect must be attributed to the smaller contact force applied to the tissue with the aspiration tube in the

ex-vivo measurements is not clear. Certainly, both the tissue altering (loss of tonicity and stopped perfusion etc.) after the removal of the uterus and the better accessibility of the tissue for the experiments in *ex-vivo* measurements, resulting in smaller contact forces and smaller initial stresses in the tissue, contribute to this effect. The maximum stretch λ_{max}, at which the predicted nominal stress in the simulated tension test reaches the value of 10×10^3 [N/m^2] at a stretch rate of $\dot{\lambda} = 0.02$ [1/s], is used to characterize the stiffness of the uterine tissue. The *ex-vivo* uterine tissue has to be stretched to approximately twice the length as the *in-vivo* uterine tissue in order to show the same nominal stress values in tension (at a stretch rate of $\dot{\lambda} = 0.02$ [1/s]).Tab. 6.13 shows the following (here, uterus 1 is not taken into account because of the poor quality of these first measurements): in the *in-vivo* measurements the maximum stretch or elongation varies between $\lambda_{max} \approx 1.1$ and $\lambda_{max} \approx 1.3$ for all measured uteri. In the *ex-vivo* measurements the maximum stretch varies between $\lambda_{max} \approx 1.2$ and $\lambda_{max} \approx 1.45$ for all measured uteri. It can be seen that *in-vivo* the variation of the maximum stretch

	uterus nr.	$max(\lambda_{max})$	$min(\lambda_{max})$	location of $max(\lambda_{max})$	location of $min(\lambda_{max})$
in-vivo	2	1.25	1.2	ventral, dorsal	fundus
	3	1.3	1.15	ventral	fundus
	4	1.175	1.1	ventral, fundus	dorsal
	5	1.125	1.1	ventral, fundus, myoma	dorsal
ex-vivo	2	/	/	/	/
	3	1.45	1.35	ventral	fundus
	4	1.325	1.25	ventral	fundus
	5	1.4	1.2	dorsal	myoma

Tab. 6.13 Summary of the approximate values of λ_{max} of the results obtained from the measurements performed on the different uteri

$\Delta\lambda = max(\lambda_{max}) - min(\lambda_{max})$ between the softest and the stiffest part of tissue on the same uterus varies between $\Delta\lambda \approx 0.025$ and $\Delta\lambda \approx 0.15$ and *ex-vivo* between $\Delta\lambda \approx 0.075$ and $\Delta\lambda \approx 0.2$. The maximum difference $\Delta\lambda$ between all *in-vivo* measurements is $\Delta\lambda \approx 0.2$ and between all *ex-vivo* measurements $\Delta\lambda \approx 0.25$. Though the *in-vivo* tissue is definitely stiffer than the *ex-vivo* tissue, the variation of the tissue stiffness seems to remain constant between

in-vivo and *ex-vivo* measurements. The intersample stiffness variation seems to be slightly higher than the variation measured on the single uteri. In all *in-vivo* measured uteri the ventral position showed the largest value of λ_{max} in the stress-elongation curves, representing the softest part of the uterine tissue, whereas the smallest value was observed either in the dorsal position or in the position at the fundus. In the *ex-vivo* stress-elongation curves in two cases out of three the ventral position showed again the largest value of λ_{max}, whereas the smallest value was observed in two out of three cases at the position at the fundus.

Seite Leer /
Blank leaf

Chapter 7

Conclusions and Outlook

7.1 Conclusions

A tissue aspiration method is presented in this work which allows to determine the mechanical properties of soft biological tissues. The mechanical properties of the aspirated tissue are determined with an inverse finite element algorithm by comparing simulated and measured pressure-deformation data. The target parameters of this inverse fit are the material parameters of the employed material law. Of the many complex mechanical properties of soft biological tissues the following were incorporated into the mechanical model of the aspirated tissue: non-linearity, incompressibility and viscoelasticity. Initial stresses in the unloaded tissue are not modelled in this work. Tissues are assumed to be homogeneous and isotropic.

Soft biological tissues are modelled within the framework of hyperelasticity, where different strain energy functions were tested. The reduced Veronda-Westmann and also the full Veronda-Westmann formulation proved to adequately model the non-linear mechanical behaviour of soft pig kidney cortex tissue. However, the number of parameters in the Veronda-Westmann material model has proven too small in order to capture slight changes in the material properties as they occur when the soft tissue is conditioned. Compared to the Veronda-Westmann formulation the proposed polynomial material law is able to model a much wider range of material behaviour. This is primarily due to the larger number of material parameters contained in the polynomial material law. With the parallelized

algorithm for the solution of the inverse finite element parameter estimation, this larger number of parameters does fortunately not result in an increase of computation time. Regarding their overall capability to predict the force-displacement behaviour of the strongly non-linear pig kidney cortex tissue both material formulations are equivalent.

A quasi-linear viscoelastic formulation is employed to model the soft tissue viscoelasticity. Experiments with a soft silgel material showed the need to include more than just one single relaxation time in the material model. The same model with four different relaxation times is used to model viscoelasticity of soft tissues. Studies on the inverse determinability of the parameters of the viscoelasticity formulation showed the need to adjust the duration of the aspiration experiments to the largest relaxation time assumed in the material model. A good force-displacement characterization of the silgel material was possible also with only estimated values for the relaxation times in the material model. The estimated material parameters showed to depend on the initial estimates used in the identification if the experimental data was gained from an experiment whose duration is smaller than the largest relaxation time in the employed material model. When aspiration experiments of a duration longer than the largest material model relaxation time are performed more information about the relaxed material answer is obtained and the determined material parameters converge in the vicinity of one single optimal set of parameters. An improvement of the determined parameters in the sense that the predicted fully relaxed material response is closer to the experimentally fully relaxed material response is only possible if the correct maximum relaxation time in the material is known. If aspiration experiments of longer duration are used together with a material model with a wrongly estimated value for the largest material relaxation time, only the variability of the resulting estimated material parameters is reduced but no improvement of the estimated parameter values is obtained.

In our soft tissue model the assumption of a homogeneous material is included. This simplification does not reflect the situation encountered in most tissue aspiration experiments. In many cases the structure of the aspirated tissue might be represented by a layered continuum. Then the question arises to what extent the assumed top layer thickness influences the determined material parameters. A study regarding the robustness of the aspiration method against geometrical model errors showed that the influence of the top layer on the determined material parameters diminishes with increasing top layer thickness. Since these effects depend also on the

stiffness and other aspects like the non-linearity of the studied material, parameters reflecting "average" tissue properties were used to perform these numerical tests.

For the simulation of the aspiration experiment an explicit axisymmetric finite element code was developed. Only the explicit formulation allowed the simulation of the large deformations observed in the aspiration experiments including the resulting contact problem and the modelling of viscoelasticity. The resulting huge computational cost of the inverse finite element parameter estimation was overcome by computing the different finite element simulations needed for the gradient evaluation on different processors. The optimization, including the gradient approximation, was then calculated by gathering the results from the different simulations on one computer. Since the optimization part itself needed only negligible computational power as compared to the finite element simulation this parallelization represents a rather simple but very efficient way to overcome the computational challenge. A much more difficult and probably less efficient parallelization of the finite element code itself was thus avoided. By also artificially increasing the material density in the quasi-static simulations of the aspiration experiment an estimated overall speed-up factor of the computations of 500 was obtained.

The tissue aspiration technique was applied *in-vivo* on human uteri. The limited time available for the *in-vivo* experiments in the operating theatre has a negative influence on the quality of the measurements. Additionally, in order to assure a leakproof contact of the aspiration tube with the tissue the tube was, at least in some of the experiments, pressed firmly against the uterus. This contact pressure was not measured and it is not clear to what extent it biases the experiments. The resulting high values for the viscoelastic weighting factors in some evaluations could be an indicator for this large contact pressure in the experiments. The uteri proved to be relatively hard as compared e.g. to pig kidney cortex. However, a pronounced decrease of the tissue stiffness between the *in-vivo* and the *ex-vivo* measurements was observed.

7.2 Outlook

Since anisotropy of soft tissues was not included in our mechanical models a quantification of the error introduced by this assumption could occur by performing multiple aspiration experiments on the same spot of preconditioned tissue or on some synthetic anisotropic material. The different

obtained side-views of the aspirated material bulge should then reflect the anisotropy of the tissue when the instrument is rotated around its vertical axis from experiment to experiment. It should be studied if the effects obtained this way would suffice to quantify the tissue's anisotropy. Including anisotropy in the simulations would require a fully three-dimensional formulation of the problem and thus immensely increase the computational effort for the inverse solution of the problem as compared to the actually used axisymmetric formulation. To circumvent the computational problem it was suggested to use an implicit finite element code with prescribed displacement boundary conditions instead of surface loads. In order to simulate the large observed deformations one could apply the profile data as prescribed displacements to the finite element model. In a second step the nodes lying on the aspirated tissue surface would then be free to move tangentially along the profile after having applied the displacements. An equilibrium iteration would then give the positions of all nodes on and inside the profile. The objective function would consist of the squared differences between the nodal forces lying on the aspirated surface and the nodal forces according to the pressure information for this loadstep. Since the implicit finite element method is much more robust if the displacements are described instead of the external loads this approach would probably lead to converging solutions. By parallelizing the code the same way as was done for the explicit code a further reduction of the computation time needed for the inverse problem could possibly be obtained. It is however not clear how large this further reduction of computation time could be because the accurate modelling of viscoelasticity requires relatively small time steps also in the implicit finite element formulation. At present the computation time needed for the evaluation of one aspiration experiment with a duration of 20 seconds is approximately 4 hours.

Many organs and tissues have a layered structure. The influence of very thin but stiff covering membranes could be studied numerically by simulation and also experimentally by performing experiments on organs before and after removal of the covering membrane.

The aspiration method could be used to determine the mechanical properties of human brain. In neurosurgery the mechanical properties of brain are of major interest. Exact positions in the patient's brain, defined by computer tomography images, have to be re-located in the operating theatre. In the widely used rigid registration procedure the previously defined position in the brain is re-located in the operating theatre by excluding any deformation of the brain although the patient usually rests in a position dif-

ferent from the one in the computer tomograph. The knowledge of the mechanical properties of the human brain would allow to calculate the deformation of the brain with respect to the situation in the computer tomograph. An enhancement of the locating procedure could thus be achieved.

The presented aspiration method could also be used for the characterization of soft rubber materials. The mechanical properties of soft materials could be tested without any need of sample preparation.

Seite Leer /
Blank leaf

Appendix A

The derivatives of the three invariants of the right Cauchy-Green deformation tensor $\boldsymbol{C}$ *with respect to the Green-Lagrange strain tensor* $\boldsymbol{E}$ *are given in this section.*

Since the Green-Lagrange strain tensor $\boldsymbol{E}$ and the right Cauchy-Green deformations tensor $\boldsymbol{C}$ are closely related to each other the following relation holds

$$\frac{\partial}{\partial E_{ij}} = 2\frac{\partial}{\partial C_{ij}}. \tag{A.1}$$

The three invariants I_1, I_2, I_3 of the right Cauchy-Green deformation tensor $\boldsymbol{C}$ are defined by

$$I_1 = C_{ii}, \tag{A.2}$$

$$I_2 = \frac{1}{2}(I_1^2 - C_{ij}C_{ij}), \tag{A.3}$$

$$I_3 = det(\boldsymbol{C}). \tag{A.4}$$

Their derivatives with respect to the components E_{ij} of the Green-Lagrange strain tensor $\boldsymbol{E}$ are given by

$$\frac{\partial I_1}{\partial E_{ij}} = 2\delta_{ij}, \tag{A.5}$$

$$\frac{\partial I_2}{\partial E_{ij}} = 2(I_1\delta_{ij} - C_{ij}), \tag{A.6}$$

$$\frac{\partial I_3}{\partial E_{ij}} = 2I_3C_{ij}^{-1}, \tag{A.7}$$

The reduced invariants J_1, J_2, J_3 of the right Cauchy-Green deformation tensor $\boldsymbol{C}$ are defined by

$$J_1 = I_3^{-1/3} I_1 , \tag{A.8}$$

$$J_2 = I_3^{-2/3} I_2 , \tag{A.9}$$

$$J_3 = I_3^{1/2} = det(\boldsymbol{F}) . \tag{A.10}$$

Their derivatives with respect to the components E_{ij} of the Green-Lagrange strain tensor $\boldsymbol{E}$ are given by

$$\frac{\partial J_1}{\partial E_{ij}} = 2I_3^{-1/3}\left(\delta_{ij} - \frac{1}{3} I_1 C_{ij}^{-1}\right) , \tag{A.11}$$

$$\frac{\partial J_2}{\partial E_{ij}} = 2I_3^{-2/3}\left(I_1 \delta_{ij} - C_{ij} - \frac{2}{3} I_2 C_{ij}^{-1}\right) , \tag{A.12}$$

$$\frac{\partial J_3}{\partial E_{ij}} = J_3 C_{ij}^{-1} . \tag{A.13}$$

Another useful formula is

$$\frac{\partial C_{ij}^{-1}}{\partial E_{kl}} = -2 C_{ik}^{-1} C_{lj}^{-1} . \tag{A.14}$$

Appendix B

In this section the finite element matrices for an axisymmetric quadrilateral element (4-node element) for nearly incompressible material behaviour are given.

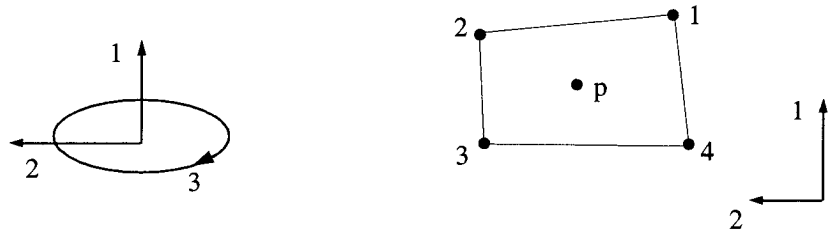

Fig. B.1 Coordinate system and four-node element with internal node numbering and pressure node at the centre of the element

Uppercase variables are again used for quantities belonging to the undeformed configuration whereas lowercase letters are used for quantities belonging to the deformed configuration. In Chapter 4 the element stiffness matrix was presented as

$$\begin{bmatrix} {}^{uu}\boldsymbol{K} & {}^{up}\boldsymbol{K} \\ {}^{up}\boldsymbol{K}^T & {}^{pp}\boldsymbol{K} \end{bmatrix} \begin{bmatrix} \hat{\boldsymbol{u}} \\ \hat{\boldsymbol{p}} \end{bmatrix} = \begin{bmatrix} {}^{ext}\boldsymbol{f} \\ \boldsymbol{0} \end{bmatrix} - \begin{bmatrix} {}^{u}\boldsymbol{f} \\ {}^{p}\boldsymbol{f} \end{bmatrix} . \tag{B.1}$$

The different matrices therein are

$${}^{uu}\boldsymbol{K} = \int_V \left(\boldsymbol{B}_L^T \, \Delta \widehat{\boldsymbol{S}} \, \boldsymbol{B}_L + \boldsymbol{B}_{NL}^T \, \widehat{\boldsymbol{S}} \, \boldsymbol{B}_{NL} \right) dV , \tag{B.2}$$

$${}^{up}\boldsymbol{K} = \int_V \left(-J_3 \boldsymbol{B}_L^T \begin{bmatrix} \bar{C}_{11}^{-1} & \bar{C}_{22}^{-1} & \bar{C}_{12}^{-1} & \bar{C}_{33}^{-1} \end{bmatrix}^T \right) dV , \tag{B.3}$$

$${}^{pp}\boldsymbol{K} = \int_V \left(\frac{1}{\kappa} \right) dV , \tag{B.4}$$

$${}^{u}\boldsymbol{f} = \int_V \left(\boldsymbol{B}_L^T \begin{bmatrix} \widehat{S}_{11} & \widehat{S}_{22} & \widehat{S}_{12} & \widehat{S}_{33} \end{bmatrix}^T \right) dV , \tag{B.5}$$

$$^{p}f = \int_{V}(-(J_3-1)-\tilde{p}/\kappa)dV\,, \tag{B.6}$$

$$\boldsymbol{B}_L = \boldsymbol{B}_{L0}+\boldsymbol{B}_{L1}\,, \tag{B.7}$$

$$\boldsymbol{B}_{L0} = \begin{bmatrix} h_{1,1} & 0 & h_{2,1} & 0 & h_{3,1} & 0 & h_{4,1} & 0 \\ 0 & h_{1,2} & 0 & h_{2,2} & 0 & h_{3,2} & 0 & h_{4,2} \\ h_{1,2} & h_{1,1} & h_{2,2} & h_{2,1} & h_{3,2} & h_{3,1} & h_{4,2} & h_{4,1} \\ 0 & \dfrac{h_1}{X_2} & 0 & \dfrac{h_2}{X_2} & 0 & \dfrac{h_3}{X_2} & 0 & \dfrac{h_4}{X_2} \end{bmatrix}, \tag{B.8}$$

$$\boldsymbol{B}_{L1} = \begin{bmatrix} l_{11}h_{1,1} & l_{21}h_{1,1} & l_{11}h_{2,1} & \dots\ l_{21}h_{4,1} \\ l_{12}h_{1,2} & l_{22}h_{1,2} & l_{12}h_{2,2} & \dots\ l_{22}h_{4,2} \\ (l_{11}h_{1,2}+l_{12}h_{1,1}) & (l_{11}h_{1,2}+l_{12}h_{1,1}) & (l_{11}h_{1,2}+l_{12}h_{1,1}) & \dots\ h_{4,1} \\ 0 & \dfrac{h_1}{X_2} & 0 & \dots\ \dfrac{h_4}{X_2} \end{bmatrix}, \tag{B.9}$$

$$\boldsymbol{B}_{NL} = \begin{bmatrix} l_{11}h_{1,1} & l_{21}h_{1,1} & \dots & l_{21}h_{4,1} \\ l_{12}h_{1,2} & l_{22}h_{1,2} & \dots & l_{22}h_{4,2} \\ (l_{11}h_{1,2}+l_{12}h_{1,1}) & (l_{21}h_{1,2}+l_{22}h_{1,1}) & \dots & (l_{21}h_{4,2}+l_{22}h_{4,1}) \\ 0 & l_{33}\dfrac{h_1}{X_2} & \dots & l_{33}\dfrac{h_4}{X_2} \end{bmatrix}, \tag{B.10}$$

$$l_{ij} = h_{M,j}u_i^M \qquad i,j = 1,2; \qquad l_{33} = h_M\frac{u_2^M}{X_2}\,. \tag{B.11}$$

With eq. (4.4) the stresses $\widehat{S}_{ij}$ are

$$\widehat{S}_{ij} = \frac{\partial\overline{W}}{\partial E_{ij}}+\frac{\partial Q}{\partial E_{ij}} = \frac{\partial\hat{W}}{\partial E_{ij}}-\tilde{p}J_3C_{ij}^{-1}\,. \tag{B.12}$$

The stress matrices defined in eq. (B.2) are given by

$$\widehat{S} = \begin{bmatrix} \widehat{S}_{11} & \widehat{S}_{12} & 0 & 0 & 0 \\ \widehat{S}_{21} & \widehat{S}_{22} & 0 & 0 & 0 \\ 0 & 0 & \widehat{S}_{11} & \widehat{S}_{12} & 0 \\ 0 & 0 & \widehat{S}_{21} & \widehat{S}_{22} & 0 \\ 0 & 0 & 0 & 0 & \widehat{S}_{33} \end{bmatrix}, \tag{B.13}$$

$$\Delta\widehat{S} = \begin{bmatrix} \frac{\partial \widehat{S}_{11}}{\partial E_{11}} & \frac{\partial \widehat{S}_{11}}{\partial E_{22}} & \frac{\partial \widehat{S}_{11}}{\partial E_{12}} & \frac{\partial \widehat{S}_{11}}{\partial E_{33}} \\ \frac{\partial \widehat{S}_{22}}{\partial E_{11}} & \frac{\partial \widehat{S}_{22}}{\partial E_{22}} & \frac{\partial \widehat{S}_{22}}{\partial E_{12}} & \frac{\partial \widehat{S}_{22}}{\partial E_{33}} \\ \frac{\partial \widehat{S}_{12}}{\partial E_{11}} & \frac{\partial \widehat{S}_{12}}{\partial E_{22}} & \frac{\partial \widehat{S}_{12}}{\partial E_{12}} & \frac{\partial \widehat{S}_{12}}{\partial E_{33}} \\ \frac{\partial \widehat{S}_{33}}{\partial E_{11}} & \frac{\partial \widehat{S}_{33}}{\partial E_{22}} & \frac{\partial \widehat{S}_{33}}{\partial E_{12}} & \frac{\partial \widehat{S}_{33}}{\partial E_{33}} \end{bmatrix}. \tag{B.14}$$

(the equations for different material laws for $\widehat{S}_{ij}$ and $\Delta\widehat{S}_{ijkl}$ can be found in Appendix C).

The right Cauchy-Green deformation $\boldsymbol{C}$ tensor is

$$\boldsymbol{C} = \begin{bmatrix} \left(\frac{\partial x_1}{\partial X_1}\right)^2 + \left(\frac{\partial x_2}{\partial X_1}\right)^2 & \frac{\partial x_1}{\partial X_1}\frac{\partial x_1}{\partial X_2} + \frac{\partial x_2}{\partial X_1}\frac{\partial x_2}{\partial X_2} & 0 \\ \frac{\partial x_1}{\partial X_1}\frac{\partial x_1}{\partial X_2} + \frac{\partial x_2}{\partial X_1}\frac{\partial x_2}{\partial X_2} & \left(\frac{\partial x_2}{\partial X_2}\right)^2 + \left(\frac{\partial x_1}{\partial X_2}\right)^2 & 0 \\ 0 & 0 & \frac{x_2}{X_2}\frac{x_2}{X_2} \end{bmatrix}. \tag{B.15}$$

In the presence of surface loads the vector of the external forces can be calculated from

$$f^1 = \begin{bmatrix} p_1 \\ p_2 \end{bmatrix} \frac{\pi}{3}(2x_2^1 + x_2^2)\sqrt{(x_2^1 - x_2^2)^2 + (x_1^1 - x_1^2)^2}\,, \quad \text{(force at node 1)}$$

$$f^2 = \begin{bmatrix} p_1 \\ p_2 \end{bmatrix} \frac{\pi}{3}(2x_2^2 + x_2^1)\sqrt{(x_2^1 - x_2^2)^2 + (x_1^1 - x_1^2)^2}\,, \quad \text{(force at node 2)} \qquad \text{(B.16)}$$

where the following coordinate system was used

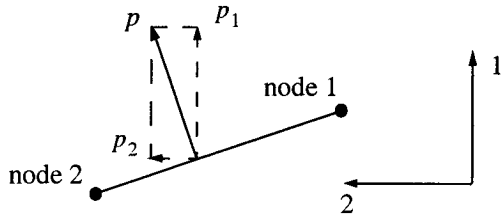

Fig. B.2 Surface load on element

The surface load was assumed to have the constant value p over the radius. The components f_i^j are added in the corresponding places to the vector ${}^{ext}f$ of the external forces.

Appendix C

The derivation of the second Piola-Kirchhoff stress tensor $\widehat{S}_{ij}$ and the tangential elastic modulus $\Delta\widehat{S}_{ijkl}$ for the Mooney-Rivlin and the Veronda-Westmann material are given in this section.

For the derivation of the second Piola-Kirchhoff stress tensor $\widehat{S}_{ij}$ and the first order fixed reference elastic moduli $\Delta\widehat{S}_{ijkl}$ we need to know the derivatives of the three invariants of the right Cauchy-Green deformation tensor with respect to C. They are listed in Appendix A. We have

$$\widehat{S}_{ij} = \frac{\partial\overline{W}}{\partial E_{ij}} + \frac{\partial Q}{\partial E_{ij}} = \frac{\partial\hat{W}}{\partial E_{ij}} - \tilde{p}J_3 C^{-1}_{ij} \,. \tag{C.1}$$

For the Mooney-Rivlin material the second Piola-Kirchhoff stresses and the first order fixed reference moduli are given by

$$\widehat{S}_{ij} = 2\mu I_3^{-1/3}\left(\delta_{ij} - \frac{1}{3}I_1 C^{-1}_{ij}\right)$$

$$+2\alpha I_3^{-2/3}\left(I_1\delta_{ij} - C_{ij} - \frac{2}{3}I_2 C^{-1}_{ij}\right) - \tilde{p}J_3 C^{-1}_{ij} \,, \tag{C.2}$$

$$\Delta\widehat{S}_{ijkl} = \frac{\partial\widehat{S}_{ij}}{\partial E_{kl}} = \frac{4}{9}(\mu J_1 + 4\alpha J_2)C^{-1}_{ij}C^{-1}_{kl} + \frac{4}{3}(\mu J_1 + 2\alpha J_2)C^{-1}_{ik}C^{-1}_{jl}$$

$$+\frac{8}{3}\alpha I_3^{-2/3}(C_{ij}C^{-1}_{kl} + C_{kl}C^{-1}_{ij}) - \frac{4}{3}I_3^{-1/3}(\mu + 2\alpha J_1)(\delta_{ij}C^{-1}_{kl} + \delta_{kl}C^{-1}_{ij})$$

$$+4\alpha I_3^{-2/3}(\delta_{ij}\delta_{kl} - \delta_{ik}\delta_{jl})$$

$$+\tilde{p}(2C^{-1}_{ik}C^{-1}_{lj} - C^{-1}_{kl}C^{-1}_{ij}) \tag{C.3}$$

whereas for the Veronda-Westmann material we have

$$\widehat{S}_{ij} = 2\mu e^{\gamma(J_1-3)} I_3^{-1/3}\left(\delta_{ij} - \frac{1}{3}I_1 C^{-1}_{ij}\right)$$

$$+2\alpha I_3^{-2/3}\left(I_1\delta_{ij} - C_{ij} - \frac{2}{3}I_2 C^{-1}_{ij}\right) - \tilde{p}J_3 C^{-1}_{ij} \,, \tag{C.4}$$

$$\Delta \widehat{S}_{ijkl} = \frac{\partial \widehat{S}_{ij}}{\partial E_{kl}} = 4\mu e^{\gamma(J_1-3)}\Big[\gamma I_3^{-2/3}\delta_{kl}\delta_{ij} - \frac{1}{3}I_3^{-1/3}(\gamma J_1+1)(\delta_{ij}C_{kl}^{-1}+\delta_{kl}C_{ij}^{-1})$$

$$+\frac{1}{9}J_1(\gamma J_1+1)C_{ij}^{-1}C_{kl}^{-1}+\frac{1}{3}J_1C_{ik}^{-1}C_{lj}^{-1}\Big]$$

$$-\frac{8}{3}\alpha I_3^{-1/3}J_1(C_{kl}^{-1}\delta_{ij}+C_{ij}^{-1}\delta_{kl})+\frac{8}{3}\alpha I_3^{-2/3}(C_{kl}^{-1}C_{ij}+C_{ij}^{-1}C_{kl})+\frac{16}{9}\alpha J_2C_{ij}^{-1}C_{kl}^{-1}$$

$$+4\alpha I_3^{-2/3}(\delta_{ij}\delta_{kl}-\delta_{ik}\delta_{jl})+\frac{8}{3}\alpha J_2C_{ik}^{-1}C_{lj}^{-1}$$

$$+\tilde{p}(2C_{ik}^{-1}C_{lj}^{-1}-C_{kl}^{-1}C_{ij}^{-1})\,. \qquad \text{(C.5)}$$

References

Aoki T., Ohashi T., Matsumoto T., Sato M., 1997, *The Pipette Aspiration Applied to the Local Stiffness Measurement of Soft Tissues*, Annals of Biomedical Engineering, Vol. 25, pp. 581-587.

Basdogan C., Ho C., Srinivasan M.A., Small S.D., Dawson S.L., 1998, *Force Interactions in Laparoscopic Simulations: Haptic Rendering of Soft Tissues*, Medicine Meets Virtual Reality, IOS Press, pp. 385-391.

Bathe K.J., 1996, *Finite Element Procedures*, Prentice Hall.

Bathe K.J., Chaudhary A., 1985, *A Solution Method for Planar and Axisymmetric Contact Problems*, International Journal for Numerical Methods in Engineering, Vol. 21, pp. 65-88.

Blatz P. J., 1969, *On the Mechanical Behaviour of Elastic Animal Tissue*, Trans. Society Rheology, Vol. 13:1, pp. 83-102.

Davies P.J., Carter F.J., Roxburgh D.G. & Cuschieri A., 1999, *Mathematical modelling for keyhole surgery simulations: spleen capsules as an elastic membrane*, Journal Theoretical Medicine, Vol. 1, pp. 247-262.

Dennis J.E. (JR.), Schnabel R.B., 1983, *Numerical Methods for Unconstrained Optimization and Nonlinear Equations*, Prentice Hall.

Decraemer W.F., Maes M.A., Vanhhuyse V.J., Vanpeperstraete P., 1980, *A Non-Linear Viscoelastic Constitutive Equation for Soft Biological Tissues based upon a Structural Model*, Journal of Biomechanics, Vol. 13, pp. 559-564.

Demiray H., 1972, *A Note on the Elasticity of Soft Biological Tissues*, Journal Biomechanics, Vol. 5, pp. 309-311.

Farshad M., Barbezat M., Flüeler P., Schmidlin F., Graber P., Niederer P., 1999, *Material Characterization of the Pig Kidney in Relation with the Biomechanical Analysis of Renal Trauma*, Journal of Biomechanics, Vol. 32, pp. 417-425.

Fletcher R., 1987, *Practical Methods of Optimization*, John Wiley & Sons, Sec. Ed.

Flory P., 1961, *Thermodynamic Relations for High Elastic Materials*, Trans. Faraday Soc., Vol. 57, pp. 829-838.

Fung Y.C., 1984, *What Principle Governs the Stress Distribution in Living Organs*, Biomechanics in China, Japan, and U.S.A. : Proceedings of An International Conference; Wuhan, Science Press, Beijing, China.

Fung Y.C., 1993, *Biomechanics: Mechanical Properties of Living Tissues*, Springer-Verlag, New York, Sec. Ed.

Guccione J.M., Okamoto R.J., 1994, *Epicardial Suction: A New Approach to Mechanical Testing of Myocardium*, Advances in Bioengineering ASME, BED-Vol. 28, pp. 9-10.

Hochmuth R.M., 1993, *Measuring the Mechanical Properties of Individual Human Blood Cells*, Journal of Biomechanical Engineering, Vol. 115, pp. 515-519.

Horowitz A., Lanir Y., Yin F.C.P., Perl M., Sheinman I., Strumpf R. K., 1988, *Structural Three-Dimensional Constitutive Law for the Passive Myocardium*, Journal Biomechanical Engineering, Vol. 110, pp. 200-207.

Johnson A.R., Quigley C.J., Freese C.E., 1995, *A Viscohyperelastic Finite Element Model for Rubber*, Computer Methods in Applied Mechanics and Engineering, Vol. 127, pp. 163-180.

Jones R.M., 1975, *Mechanics of Composite Materials*, McGRAW-HILL BOOK COMPANY.

Kimmel E., Kamm R.D., Shapiro A.H., 1987, *A Cellular Model of Lung Elasticity*, Journal Biomechanical Engineering, Vol. 109, pp. 126-131.

Kühnapfel U.G., Krumm H.G., Kuhn C., Hübner M., Neisius B., 1995, *Endosurgery simulations with KISMET: A Flexible Tool for Surgical Instrument Design, Operation Room Planning and VR Technology based Abdominal Surgery Training*, Proc. Virtual Reality World '95, Stuttgart, pp. 165-171.

Kyriacou S. K., Schwab C., Humphrey J. D., 1996, *Finite Element Analysis of Nonlinear Orthotropic Hyperelastic Membranes*, Computational Mechanics, Vol. 18, pp. 269-278.

Liu Z., Bilston L., 1998, *Rheological Properties of Bovine Liver Tissue*, Advances in Bioengineering, BED-Vol. 39, pp. 361-362.

Moulton M. J., Cresswell L. L., Actis R. L. Myers, K. W., Vannier M. W., Szabó B. A., 1995, *An Inverse Approach to Determining Myocardial Material Properties*, Journal of Biomechanics, Vol. 28, pp. 935-948.

Mow V.C., Kuei S.C., Lai W.M., Armstrong C.G., 1980, *Biphasic Creep and Stress Relaxation of Articular Cartilage in Compression: Theory and Experiments*, Journal of Biomechanical Engineering, Vol. 102, pp. 73-84.

Muthupillai R., Rossmann P.J., Lomas D.J., Greenleaf J.F., Riederer S.J., Ehman R.L., 1995, *Magnetic Resonance Elastography by Direct Visualization of Propagating Acoustic Strain Waves*, Science, Vol. 269, pp. 1854-1857.

Neubert H.K.P., 1963, *A Simple Model Representing Internal Damping in Solid Materials*, Aeronautical Quarterly, Vol. 14, pp. 187-210.

Ogden R.W., 1997, *Non-Linear Elastic Deformations*, Dover Publications Inc., Mineola, New York.

Ohashi T., Matsumoto T., Aoki T., Sato M., 1995, Local Elastic Moduli of Bovine and Porcine Aortic Walls Measured with Pipette Aspiration Technique, Advances in Bioengineering ASME, BED-Vol. 31, pp. 259-260.

Okamoto R.J., Guccione J.M., Moulton M.J., Pasque M.K., 1995, *Measurement of Left Ventricular Deformation During Epicardial Suction*, Advances in Bioengineering ASME, BED-Vol. 31, pp. 255-256.

Okamoto R.J., Moulton M.J., Peterson S.J., Li D., Pasque M.K., Guccione J.M., 2000, *Epicardial Suction: A New Approach to Mechanical Testing of the Passive Ventricular Wall*, Journal of Biomechanical Engineering, ASME, Vol. 122, pp. 479-487.

Puso M. A., Weiss J. A., 1998, *Finite Element Implementation of Anisotropic Quasi-Linear Viscoelasticity Using a Discrete Spectrum Approximation*, Journal of Biomechanical Engineering, Vol. 120, pp. 62-70.

Rhomberg A., 2000, *Real-Time Finite Elements: A Parallel Computer Application*, Diss. ETH Nr. 13928.

Rivlin R.S., Saunders D.W., 1951, *Large Elastic Deformations of Isotropic Materials-VII. Experiments on the Deformation of Rubber*, Philosophical Transactions of the Royal Society of London Series A, Vol. 243, pp. 251-288.

Rubin M.B., Bodner S.R., Binur N.S., 1998, *An Elastic-Viscoplastic Model For Excised Facial Tissues*, Journal of Biomechanical Engineering, Vol. 120, Nr. 5, pp. 686-689.

Sato M., Theret D.P., Wheeler L.T., Oshima N., Nerem R.M., 1990, *Application of the Micropipette Technique to the Measurement of Cultured Porcine Aortic Endothelial Cell Viscoelastic Properties*, Journal of Biomechanical Engineering, Vol. 112, pp. 263-268.

Simo J.C., Taylor R.I., Pister K.S., 1985, *Variational and Projection Methods for the Volume Constraint in Finite Deformation Elasto-Plasticity*, Computer Meth. Appl. Mech. Engng., Vol. 51, pp. 177-208.

Spector A.A., Brownell W.E., Popel A.S., 1996, *A Model for Cochlear Outer Hair Cell Deformations in Micropipette Aspiration Experiments: An Analytical Solution*, Annals of Biomedical Engineering, Vol. 24, pp. 241-249.

Sussman T., Bathe K.J., 1987, *A Finite Element Formulation for Nonlinear Incompressible Elastic and Inelastic Analysis*, Journal Computers & Structures, Vol. 26, pp. 357-409.

Theret D.P., Levesque M.J., Sato M., Nerem R.M., Wheeler L.T., 1988, *The Application of a Homogeneous Half-Space Model in the Analysis of Endothelial Cell Micropipette Measurements*, Journal of Biomechanical Engineering, Vol. 110, pp. 190-199.

Veronda D.R., Westmann R.A., 1970, *Mechanical Characterization of Skin-Finite Deformations*, Journal of Biomechanics, Vol. 3, pp. 111-124.

Vuskovic V., 2001, *Instrument for in-vivo Aspiration Experiments*, Diss. ETH. Nr. 14222.

Woo S. L-Y., Gomez M. A., Akeson W.H., 1981, *The Time and History-Dependent Viscoelastic Properties of the Canine Medial Collateral Ligament*, Journal of Biomechanical Engineering, Vol. 103, pp. 293-298.

Woo S. L-Y., Johnson G. A., Smith B.A., 1993, *Mathematical Modelling of Ligaments and Tendons*, Journal of Biomechanical Engineering, Vol. 115, pp. 468-473.

Yamada H., 1970, *Strength of Biological Materials*, The William & Wilkins Company, Baltimore.

Zienkiewicz O.C., Taylor R.L., 1994, *The Finite Element Method*, McGraw-Hill Book Company, Vol. 1, Basic Formulation and Linear Problems, Fourth Edition.

Seite Leer /
Blank leaf

Curriculum vitae

Martin Kauer

Born on 26 May, 1970 in Bozen/Bolzano, Italy.

1976 - 1981	Elementary school in Bozen/Bolzano, Italy.
1981 - 1984	Secondary school in Bozen/Bolzano, Italy.
1984 - 1989	Wissenschaftliches Lyzeum Raimund von Klebelsberg in Bozen/Bolzano, Italy.
1990 - 1995	Studies at the Department of Mechanical Engineering of the Swiss Federal Institute of Technology ETH, Zurich, Switzerland.
1996 - 2001	Doctoral student, research and teaching assistant at the Institute of Mechanical Systems of the ETH Zurich.